

RSC Advances



This is an *Accepted Manuscript*, which has been through the Royal Society of Chemistry peer review process and has been accepted for publication.

Accepted Manuscripts are published online shortly after acceptance, before technical editing, formatting and proof reading. Using this free service, authors can make their results available to the community, in citable form, before we publish the edited article. This *Accepted Manuscript* will be replaced by the edited, formatted and paginated article as soon as this is available.

You can find more information about *Accepted Manuscripts* in the [Information for Authors](#).

Please note that technical editing may introduce minor changes to the text and/or graphics, which may alter content. The journal's standard [Terms & Conditions](#) and the [Ethical guidelines](#) still apply. In no event shall the Royal Society of Chemistry be held responsible for any errors or omissions in this *Accepted Manuscript* or any consequences arising from the use of any information it contains.

Crumpled Graphene: Preparation and Applications

Waleed M. A. El Rouby

Materials Science and Nanotechnology Department, Faculty of Postgraduate Studies for Advanced Sciences, Beni-Suef University, Egypt.

Corresponding author: Tel.: (+2) 01225834333; Fax: (+2) 082 2244137; E-mails address: waleedmohamedali@yahoo.com or waleedmohamedali@psas.bsu.edu.eg
(*Waleed M. A. El Rouby*)

Abstract

A comprehensive overview and description of crumpled graphene explored in recent years for energy storage applications is presented. Although graphene is known as one of the best electronic materials, preparing of crumpled graphene has been less explored. This article selectively aims to present an overview of the advancement of research in crumpled graphene, in the area of preparation and applications especially in energy storage, such as supercapacitor and lithium ion batteries. When graphene was transformed to the crumpled form, the resulting one can give superior capacitance due to their unique properties like extremely high specific surface area, high conductivity and stability against graphitization (aggregation-resistant) compared to those of flat graphene sheets which tend to aggregation and thus lead to a dramatic decrease in the surface area, leading to a poor capacitance.

Table of contents

1.	Introduction	
2.	Preparation methods	
2.1.	<i>Aerosol spray drying method</i>	
2.1.1.	<i>Controlling the crumpling process</i>	
2.1.1.1.	<i>Effect of evaporation rate</i>	
2.1.1.2.	<i>Effect of heating</i>	
2.1.1.3.	<i>Effect of precursor concentration</i>	
2.1.1.4.	<i>Effect of pH</i>	
2.2.	<i>Hydrothermal method</i>	
2.3.	<i>Thermal reduction of graphene oxide method</i>	
2.4.	<i>Fast cooling method</i>	
2.5.	<i>Mechanical method</i>	
2.5.1.	<i>Fabrication of graphene paper</i>	
2.5.2.	<i>Crumpling and unfolding graphene paper</i>	
2.5.3.	<i>Crumpling control</i>	
3.	Applications	
3.1.	<i>Crumpled graphene for supercapacitor</i>	
3.2.	<i>Crumpled graphene in Lithium-ion batteries</i>	
4.	Conclusion	
	References	

1. Introduction

Two-dimensional (2D) graphene oxide (GO) nanosheets are attracting tremendous interest due to their exceptional properties emanating from unique morphology [1-3]. Theoretically, GO nanosheets have a high specific surface area of over 2500 m²/g [4], making them highly desirable for use as a 2D support for many applications. These nanosheets display high flexibility, enabling the possibility of encapsulation for drug delivery, photocatalysis, solar cells, and electrical energy storage systems [4-7]. One particular issue is the tendency to aggregate (restacking) due to strong intersheet adhesion (van der Waals attraction) [8]. Restacking of these nanosheets reduces their accessible surface area and hence negatively affects the properties and subsequent applications.

One possible solution is to turn the 2D nanosheets into three-dimensional (3D) crumpled balls. Unlike flat sheets, the crumpled GO balls have high free volume and excellent compressive properties, and can tightly pack without significantly reducing the accessible surface area [9]. At a crumpled equilibrium, approximately 58.6% of the accessible surface area, i.e., over 1500 m²/g is maintained [10], which is still much larger than those of conventional laminar or porous materials.

Crumpled sheet materials represent a new class of structures attracting a great interest because of their unique mechanical and physical properties. Such materials seem to be very promising for applications in the fields where extremely large specific surface area is required [11], which is in its turn governed by the topology of crumpled configuration [12]. These applications are ranged from virus capsids and polymerized membranes to folded engineering materials and geological formations [13].

Exploration of crumpled graphene structures is one of recent directions in modern materials science due to some promising results and perspectives revealed [11, 14]. One of the new findings is that crumpling eliminates layer stacking followed by transition to graphite and can be obtained on a commercial scale at a low price [13]. Together with combination of prominent properties of flat graphene [15, 16] it opens great opportunities for graphene-based bulk nanomaterials. A drastic increase of graphene specific capacitance caused by crumpling was shown in [17]. Crumpling of graphene can be performed in controllable [18] or uncontrollable [11, 15] manner.

The curvature imposed on a graphene sheet by external confinement or forces concentrates largely on the ridges [19, 20] and leads to considerable changes in various properties of the material. Graphene is very easy to bend and many researchers have discussed how to introduce ripples, folds or wrinkles in graphene sheets in a controllable fashion and how to use such corrugations [21-23]. Such one-or two-dimensional (2D) ripples can strongly affect the electronic properties of graphene by inducing effective magnetic fields and changing local potentials [23-25]. Moreover, crumpled graphene flakes, which can be characterized by various distribution of folds and ripples, are one of the main structural units for bulk nanomaterials and should be carefully studied.

2. Preparation methods

2.1. *Aerosol spray drying method*

In this method a suspension of GO prepared by dispersing the GO powder in DI water with the aid of ultrasonication. Then, the suspension was nebulized by an ultrasonic nebulizer to form aerosol particles, which carried by Ar, H₂, N₂ or any carrier gas at a flow rate of $\sim 0.5 \text{ L min}^{-1}$ through a horizontal tube furnace preheated at a desired temperature (600 - 700 °C). After that the GO sheets were quickly dried and crumpled during flight in the tube furnace (Fig. 1). Si wafer, ITO glass (1 x 1 in.), Cu foil (0.25 in. diameter disk), Ni foam, carbon cloth or any other support materials were used as substrates to collect the aerosol downstream [17, 26, 27].

Because the average size of the generated droplets from the ultrasonic nebulizer was around 1.7 μm , the solvents rapidly evaporated in the tube furnace, leading to the shrinkage of GO sheets and the subsequent compression of GO sheets into crumpled balls with a submicrometer size. Because of the high temperature, GO sheets were also partially reduced, as indicated by the color change from brown to black [17, 26, 27].

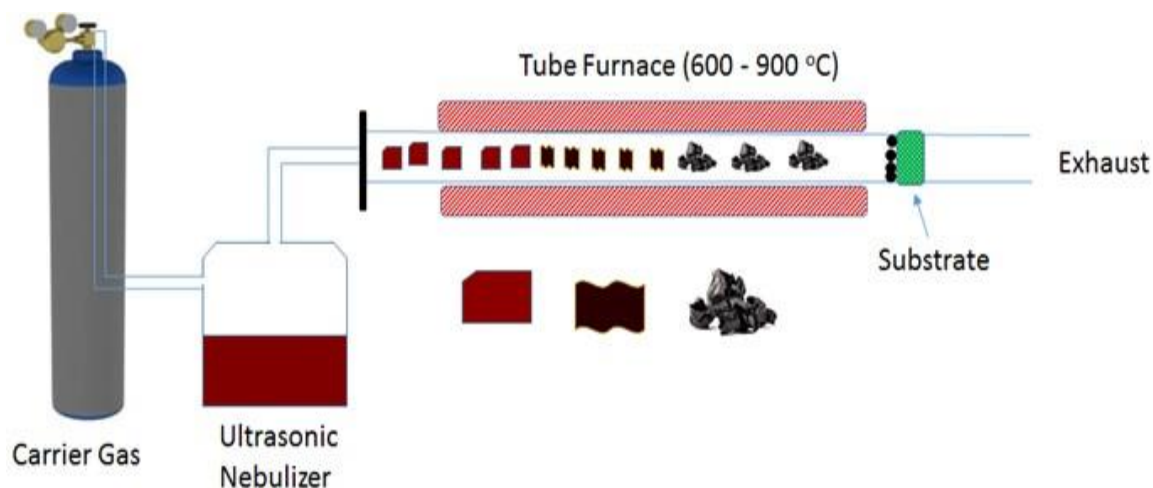


Fig. 1: Shows the experimental setup for producing crumpled graphene (CG).

SEM images (Fig. 2a and b) indicate that each of the crumpled graphene (CG) balls is formed by a single piece of GO sheet, and in general, a larger GO sheet led to a CG ball with a larger diameter. Experimental results indicated that, the size of the CG balls was mainly dependent on the size of the initial GO sheets as well as the number of layers of the GO or GO thickness [26-29].

TEM observation of the interior structure of CG balls (Fig. 2c and d) shows a typical CG ball structure, which is a three dimensional structure with a folded graphene sheet as in Fig. 2c. The formation of CG balls is motivated by the capillary force associated with rapid solvent loss; the physical deformation naturally creates folds on the graphene surface. The TEM image clearly shows the folded structure, evidenced from the interlaced carbon lattices from the HRTEM image (Fig. 2d).

By the same method metal oxide/crumpled graphene composite can be prepared as described by many authors [17, 26, 28, 29], only the required concentration of the metal oxide precursor was added to the GO suspension before mobilized by ultrasonic nebulizer.

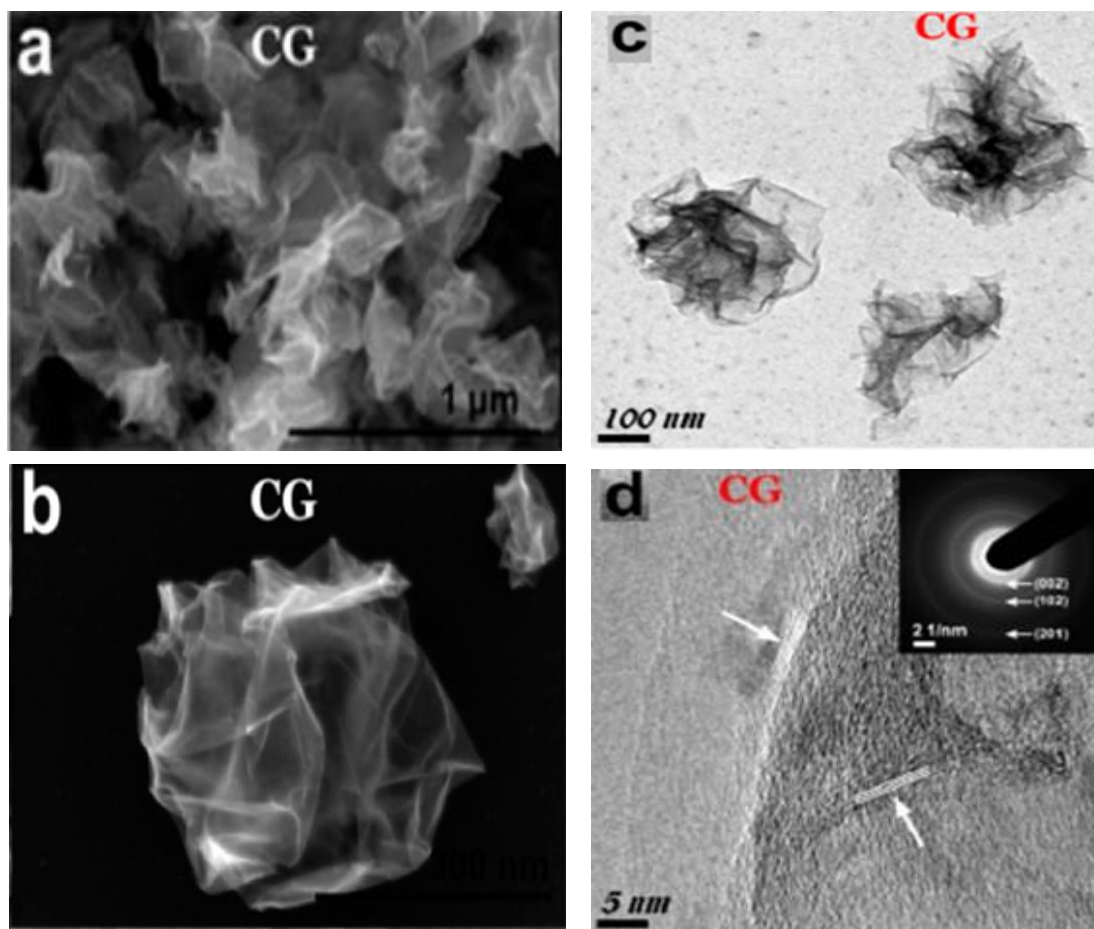


Fig. 2: SEM images of bare CG low and high magnification (a,b) and TEM and HRTEM images of bare CG balls (c,d) [26]. Copyright 2012, American Chemical Society.

The crumpled graphene–MoO₂ composites were directly prepared by spray pyrolysis from a stable graphene oxide colloidal solution in the presence of Mo ions. A quartz reactor of 1200 mm length and 50 mm diameter was used, and its temperature was maintained at 900 °C. The air flow rate (carrier gas) was 5 L.min⁻¹. As-prepared crumpled graphene–MoO₂ composite powders were post-treated at 300 °C under an air atmosphere to form MoO₃-based composite powders [28].

Fig.3 represent the formation mechanism of the crumpled graphene–MoO₂ composite powders through spray pyrolysis. Micrometer-sized droplets were formed by applying an ultrasonic nebulizer to a colloidal spray solution containing well dispersed few-layer GO and ammonium molybdate [30]. The colloidal solution was stable for several hours while being nebulized. Neither precipitation of GO to the bottom of the spray solution chamber nor its segregation occurred during nebulization. Fast droplet-drying and decomposition of both ammonium molybdate and GO occurred in the front side of the reactor, which was kept at 900 °C. Drying of these droplets formed the micrometer-sized crumpled GO powder. Precipitation and decomposition of ammonium molybdate formed uniformly dispersed MoO₂ nanopowders inside the crumpled GO under a N₂ atmosphere. GO sheets prevented the growth of MoO₂ nanocrystals to micrometer-sized aggregates. At the same time, the reduction of GO sheets resulted in the formation of a crumpled graphene–MoO₂ composite powder. Therefore, the crumpled graphene–MoO₂ composite powders were directly prepared by one-step spray pyrolysis. One particle of crumpled graphene–MoO₂ composite powder was formed from one droplet at the short residence time of the droplet or powder inside the reactor of 10 s. The crumpled graphene–MoO₂ composite powders formed by spray pyrolysis were post-treated at 300 °C under an air atmosphere to form the corresponding MoO₃-based composite powders [28].

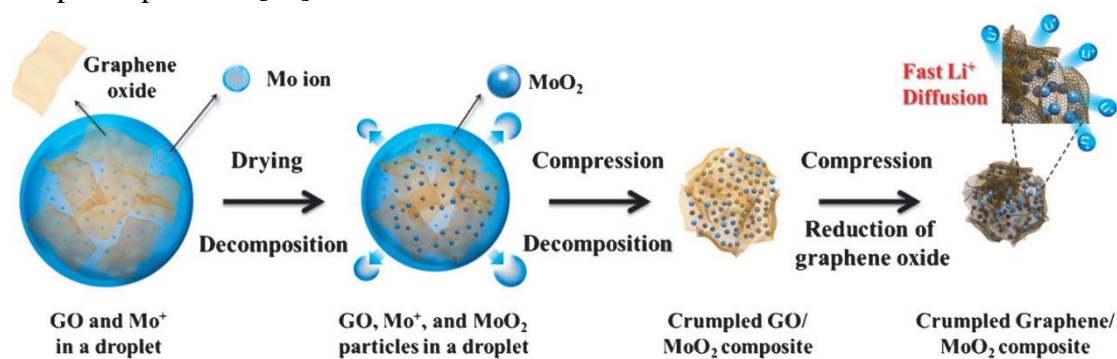


Fig. 3: Schematic diagram of the formation mechanism of the crumpled graphene–MoO₂ composite powders by one-pot gas phase reaction process [28]. Copyright 2014, Wiley-VCH Verlag GmbH & Co. KGaA, Weinheim.

The SEM and low-resolution TEM images indicated the presence of composite powders (Fig. 3(a-d)). Spherical particles were not shown in the SEM image of MoO₂ powders without graphene formed from the GO-free droplets. This might be due to the colloidal solution maintaining its stability during nebulization. MoO₂ nanocrystals and graphene sheets were observed in the high-resolution TEM image (Fig. 4d). The TEM images revealed that MoO₂ was uniformly distributed inside the crumpled graphene powders.

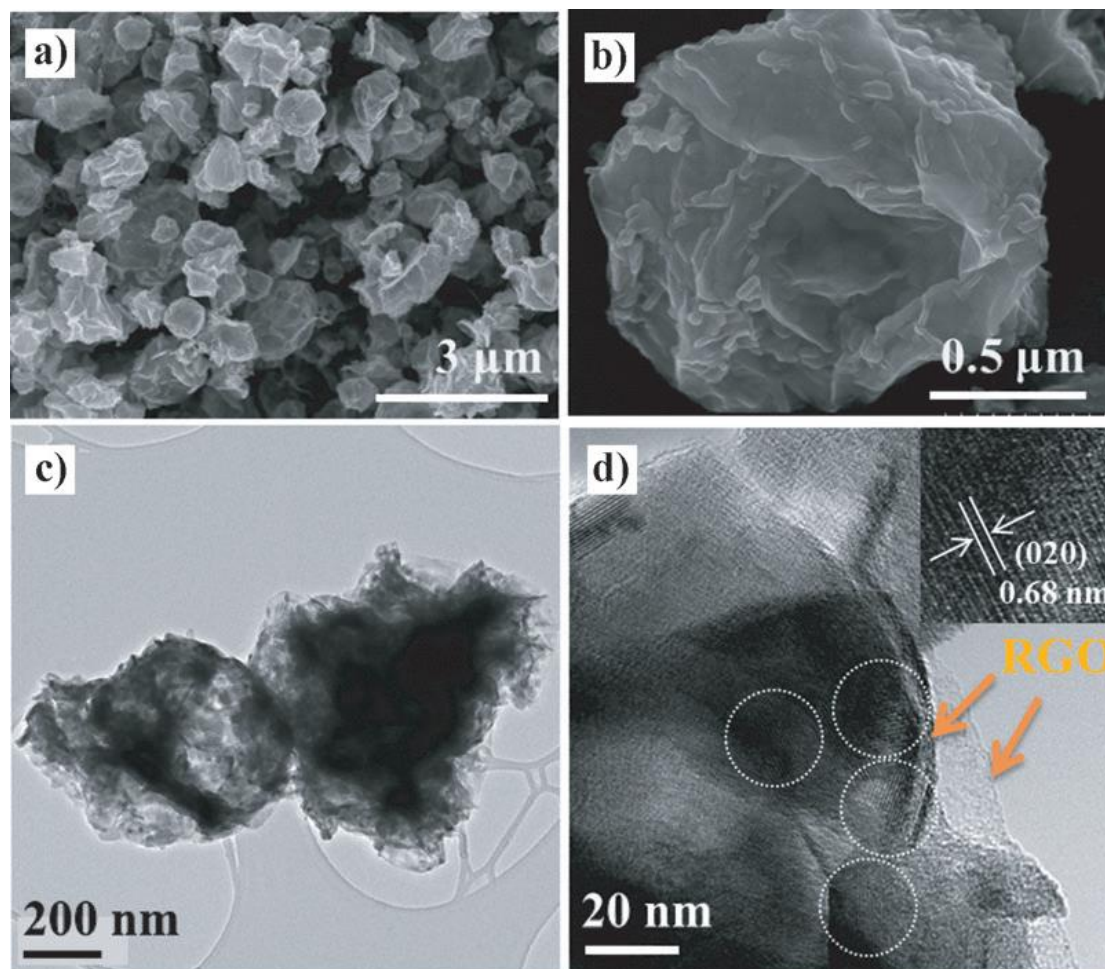


Fig. 4: Morphologies of the crumpled graphene–MoO₂ composite powders: a) and b) FE-SEM images, c) and d) TEM and HRTEM images [28]. Copyright 2014, Wiley-VCH Verlag GmbH & Co. KGaA, Weinheim.

By the same method Choi et al. [29] prepared Ni/NiO-crumpled graphene composite powders using Ni nitrate as a precursor for Ni. The SEM and TEM images shown in Fig 5(a-d) suggest that the composite powder particles had a crumpled structure. Ni/NiO nanoclusters several nanometers in size were uniformly distributed all over the graphene powder particles.

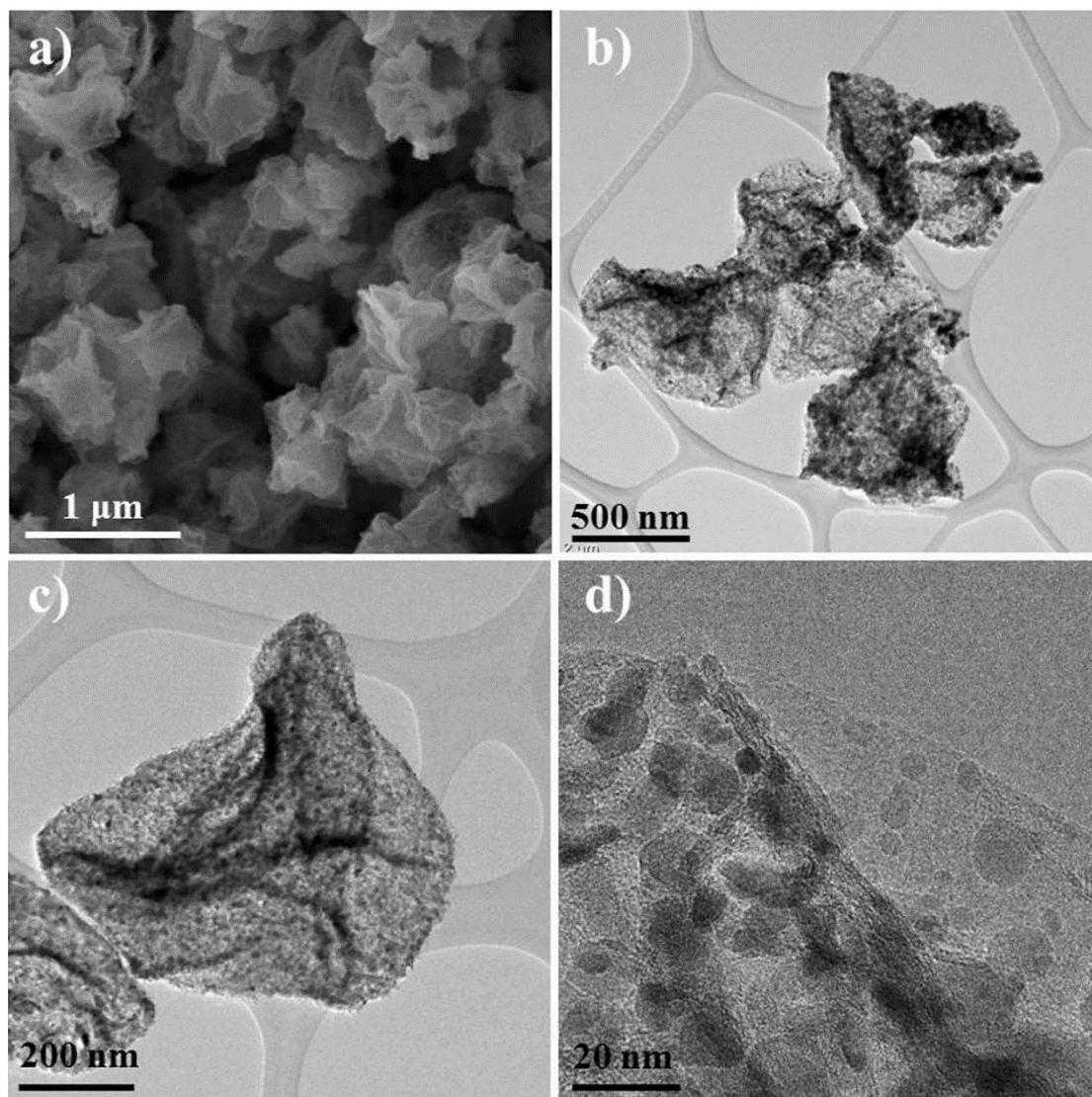


Fig. 5: Morphologies images of the Ni/NiO graphene composite powders prepared by spray pyrolysis: (a) SEM, (b)– (d) TEM [29]. Copyright 2014, Nature Publishing Group.

Crumpled reduced graphene oxide (rGO) nanoparticles were synthesized by ultrasonic aerosolization of GO suspensions with varying concentrations to a spray of approximately 2–10 μm diameter droplets, and then suspended in nitrogen gas flow. The GO mist in nitrogen gas was directed to a tube furnace for fast drying. After drying, the obtained rGO nanoparticles were captured on a polycarbonate filter [31].

The conceptual model for the aerosol formation of crumpled reduced GO particles is shown in Fig. 6. During drying, there is evidence that GO sheets tend to accumulate on the surfaces of the water droplet [32]. Near the end of the evaporation process, the spherical, onion peel- like multilayer GO film is collapsed by capillary forces into a folded GO nanoparticle with some characteristics of an empty nanosack [32]. The droplet surface acts as a template to guide the initial multilayer GO film formation, and the buckling from spherical geometry prevents further parallel stacking and retains a portion of the GO surface area [32].

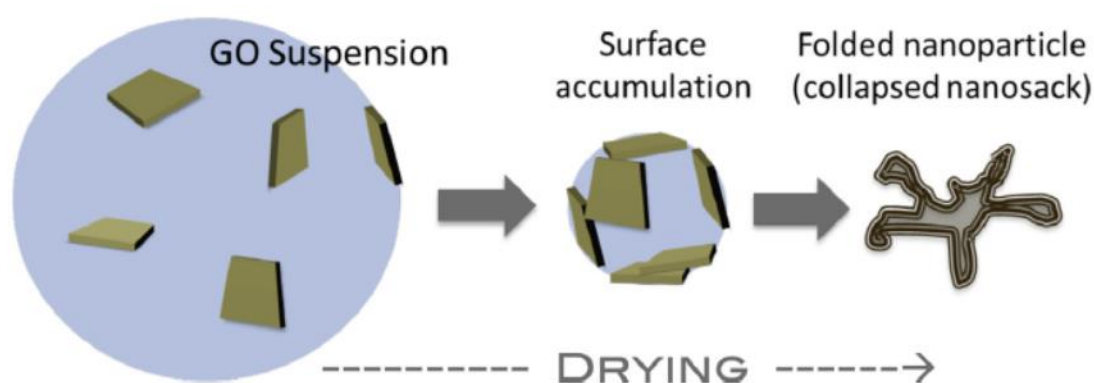


Fig. 6: Conceptual model of formation of crumpled reduced graphene oxide (rGO) nanoparticles during the drying process [31]. Copyright 2013, Elsevier Ltd.

2.1.1. Controlling the crumpling process

An aerosol-based process has been shown to be a rational method to realize the crumpling of GO nanosheets [9, 27]. The method is simple yet effective, with an extremely short processing time of several seconds [33, 34]. In addition, it is applied in a continuous manner, avoiding batch-to-batch variations. The crumpling of the 2D nanosheets, however, is complex, in which many parameters are involved [35]. Although the production of crumpled GO particles has been demonstrated using aerosol methods [9, 27–29, 36–38] systematic investigations on the correlations between the

confinement force and various parameters, such as evaporation rate and precursor concentration, have been rarely established. These factors that can affect the crumpling of reduced graphene sheets during aerosol process were investigated by [35].

2.1.1.1. Effect of evaporation rate

When droplets were aerosolized and underwent solvent evaporation, evaporation-driven crumpling of GO nanosheets, and further drying to form the final GO or reduced GO particles. The confinement force magnitude is a critical factor determining the morphology as well as the size of the dry GO particles. If the evaporation rate is slow, the confinement force is weak; hence only GO nanosheets with ripples (the so-called rippled GO [35, 39]) are formed (Fig. 7). On the other hand, crumpled GO balls are obtained when the confinement force is high due to rapid evaporation [35].

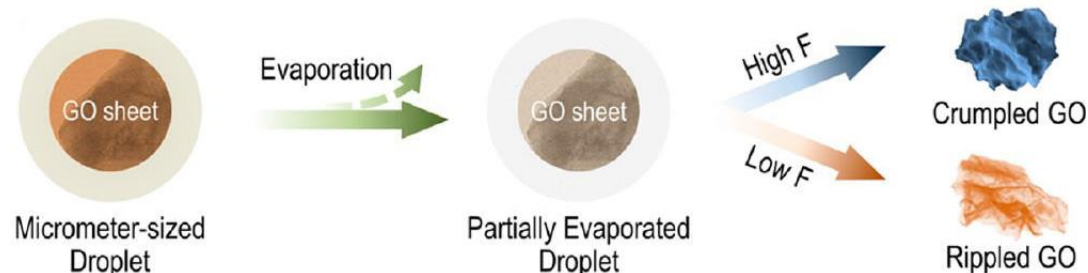


Fig. 7: The possible formation mechanism of crumpled GO [35]. Copyright 2012, American Chemical Society.

At temperatures of 200 °C, due to the weak confinement force generated by slow water evaporation the GO nanosheets are warped with ripples and ridges, but no crumpled GO balls were observed (Fig. 8(a, e)). The collected GO sample at this temperature has a pale yellow color (see the digital photo in Fig. 8(a, e)), indicating a low reduction percentage of GO to graphene. At temperatures of 400 °C and higher, crumpled GO particles were formed. A typical crumpled GO particle is highlighted in Fig. 8b (inset), which has a quasi-spherical morphology with relatively smooth surfaces. With increasing furnace temperature, more sharp ridges emerged on the crumpled GO particles (see inset in Fig. 8c). At even higher temperatures, such as 1000 °C, crumpled GO particles also tended to agglomerate due to sintering effect (Fig. 8(d, h)) [35, 40].

The GO samples color were changed from pale yellow to dark brown to black with increasing the furnace temperature. This has been suggested as partial restoration of the π network within the carbon structure (thermal reduction) and has been witnessed through chemical reduction of the GO sheets [35, 41].

Scanning mobility particle sizer (SMPS, TSI Inc.) was used for the in-line particle size measurements of GO particles. A typical particle size distribution (PSD) of the crumpled GO particles synthesized from a diluted GO aqueous suspension is shown in Fig. 9a. The geometric mean diameter (D_{pg}) of the crumpled GO particles decreases with increasing evaporation rate (open squares with solid line, Fig. 9b) [35]. The reason for this is attributed to the increased confinement force as the solvent evaporation rate increased. Although the determination of the confinement force exerted on the GO nanosheets is complex due to the large number of physical and geometric uncertainties [27], the correlation between the confinement force and solvent evaporation rate is of vital importance and should be understood quantitatively.

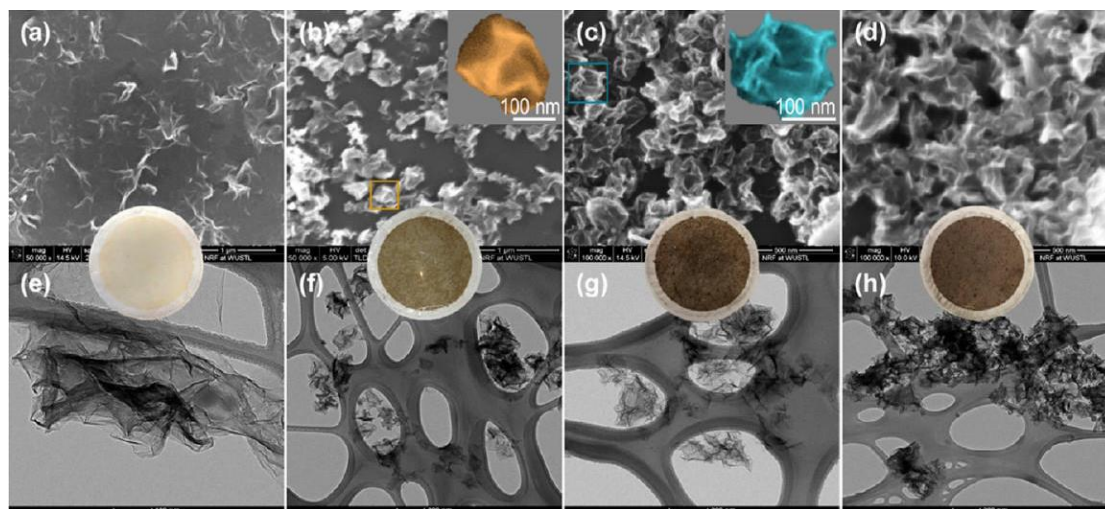


Fig. 8: Morphology evolution of GO particles as a function of furnace temperature. (a–d) FESEM images and (e–h) corresponding TEM images. (a,e) 200 °C, (b,f) 400 °C, (c,g) 800 °C, and (d,h) 1000 °C. The spherical inset at each condition is the corresponding digital photo of GO collected on a filter. Individual crumpled GO particles are highlighted in panels b (gold) and c (aqua) [35]. Copyright 2012, American Chemical Society.

2.1.1.2. Effect of heating

It is clear that the removal of water from GO nanosheets drives the crumpling process, the so-called evaporation-induced crumpling [9, 27]. The furnace temperature is therefore the important parameter as it determines the evaporation rate. Previous research on the thermal stability analysis of self-adhered membranes, however, indicated that the heating has no significant effect on the crumpling process [10, 27, 42]. To verify this effect, Wang et al [35] added diffusion dryers in front of the furnace (see inset in Fig. 9a). The purpose of adding diffusion dryers was to absorb water from droplets before their entering into the furnace. By a simple calculation, to absorb almost all water from droplets two diffusion dryers are enough. Therefore the crumpling should happen mostly inside the diffusion dryers rather than inside the furnace in the case of adding dryers [35]. Figure 9b shows the particle sizes of crumpled GO particles as a function of evaporation rate under different configurations of diffusion dryers.

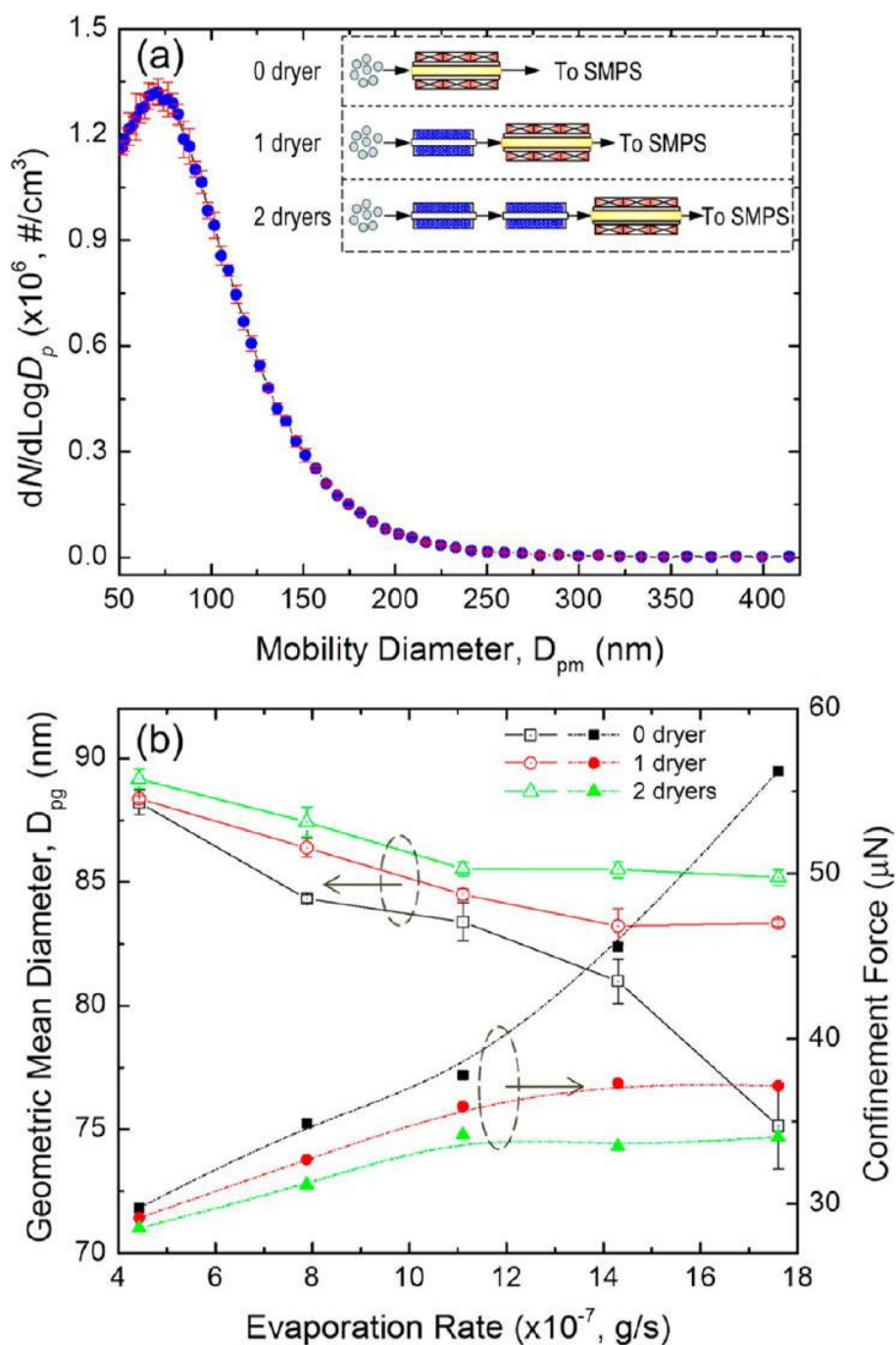


Fig. 9: Particle size measurements and confinement force calculations. (a) A typical PSD of crumpled GO particles synthesized at 400 °C from 0.3 mg/mL suspension measured by SMPS. (b) Geometric mean diameters of crumpled GO particles and the corresponding confinement force as a function of evaporation rate. The above measurements and calculations were carried out under the following conditions: $P_{\text{neb}} = 96.53 \text{ kPa}$ ($D_d = 2.82 \text{ }\mu\text{m}$) and $C = 0.3 \text{ mg/mL}$ [35]. Copyright 2012, American Chemical Society.

As explained above, with increasing furnace temperature the particle size decreases significantly in the case of no diffusion dryer installed. However, with diffusion dryers installed, the temperature effect becomes insignificant, where the particle size curves are rather flat (constant size). Furthermore, in the case of two dryers installed, the particle sizes are generally larger, and they did not decrease after temperatures increased from 600 to 1000 °C (corresponding to 1.11×10^{-6} to 1.76×10^{-6} g/s). The obtained larger particle sizes are due to the weaker confinement force exerted on GO nanosheets resulting from slow evaporation rate (at room temperature inside the dryers). Wang et al results also confirmed that without evaporation of water in the furnace, the furnace temperature has no significant effect on the crumpling process [35].

2.1.1.3. Effect of precursor concentration

The precursor concentration is an important factor to be taken into account, which has been investigated by Wang et al [35]. From the results, the confinement force decreases with the precursor concentration. With increasing precursor concentration, the particle size also increases based on the mass conservation. The particle size, however, is inversely proportional to the confinement force. Therefore, the results are the compromise between the precursor concentration and particle size.

2.1.1.4. Effect of pH

pH is another crucial parameter to be considered that is closely related to the physiological activity of GO aqueous suspension [43]. The effect of pH on the stability of aqueous GO solution has also been studied by [35]. The results reveal that the zeta potential increases with pH, indicating the increase in electrostatic repulsive force, which is responsible for stabilization (Fig. 10) [44, 45]. It is therefore expected that the number of multilayered GO sheets inside a crumpled GO particle may increase with decreasing zeta potential. However, there are no significant size and morphology variations of the crumpled GO particles prepared from GO aqueous solutions with different pH based on TEM (Fig. 11) as well as SMPS analyses (Fig. 12). The reason may be due to the smaller magnitude of the electric repulsive force as compared to the

corresponding confinement force [35], which needs further investigation in the near future.

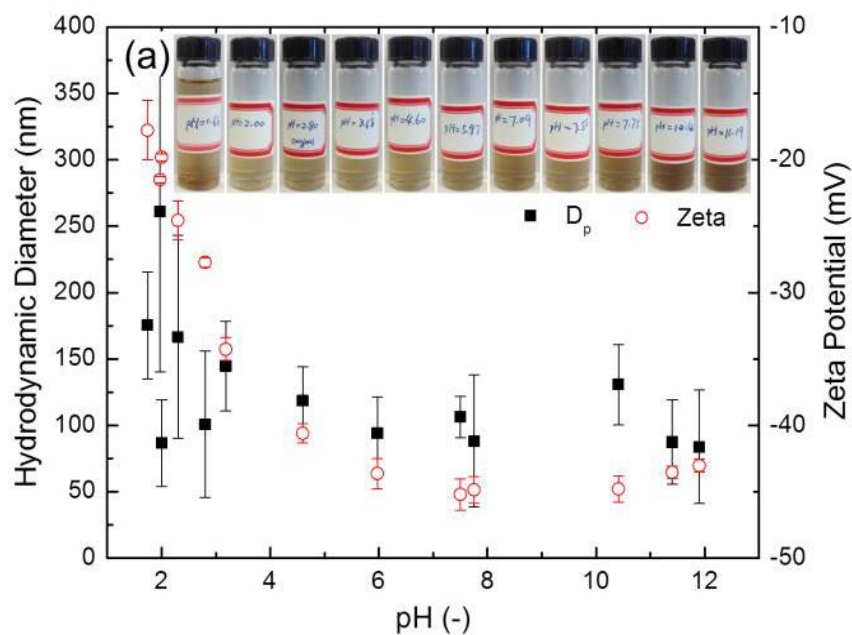


Fig. 10: pH effect on the size and surface properties of graphene oxide. (a) Dynamic particle diameter and zeta potential [35]. Copyright 2012, American Chemical Society.

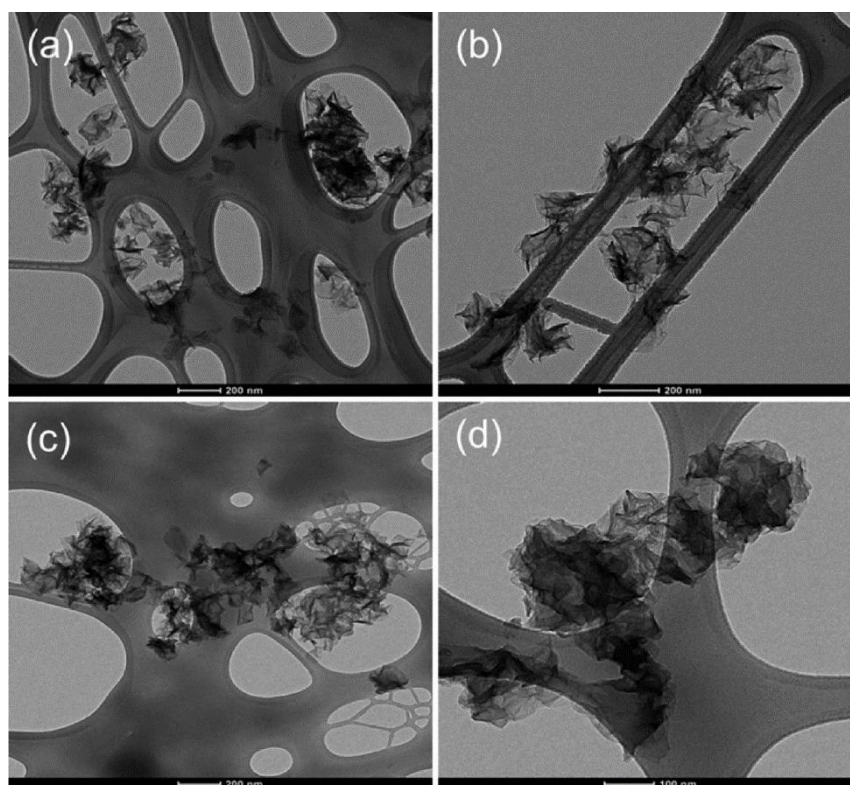


Fig. 11: TEM images of the crumpled GO particles as a function of pH: (a) 2.80, (b) 4.16, (c) 7.19, and (d) 10.02. The crumpled GO was synthesized from a diluted GO suspension ($C = 0.3$ mg/mL) at 400 °C [35]. Copyright 2012, American Chemical Society.

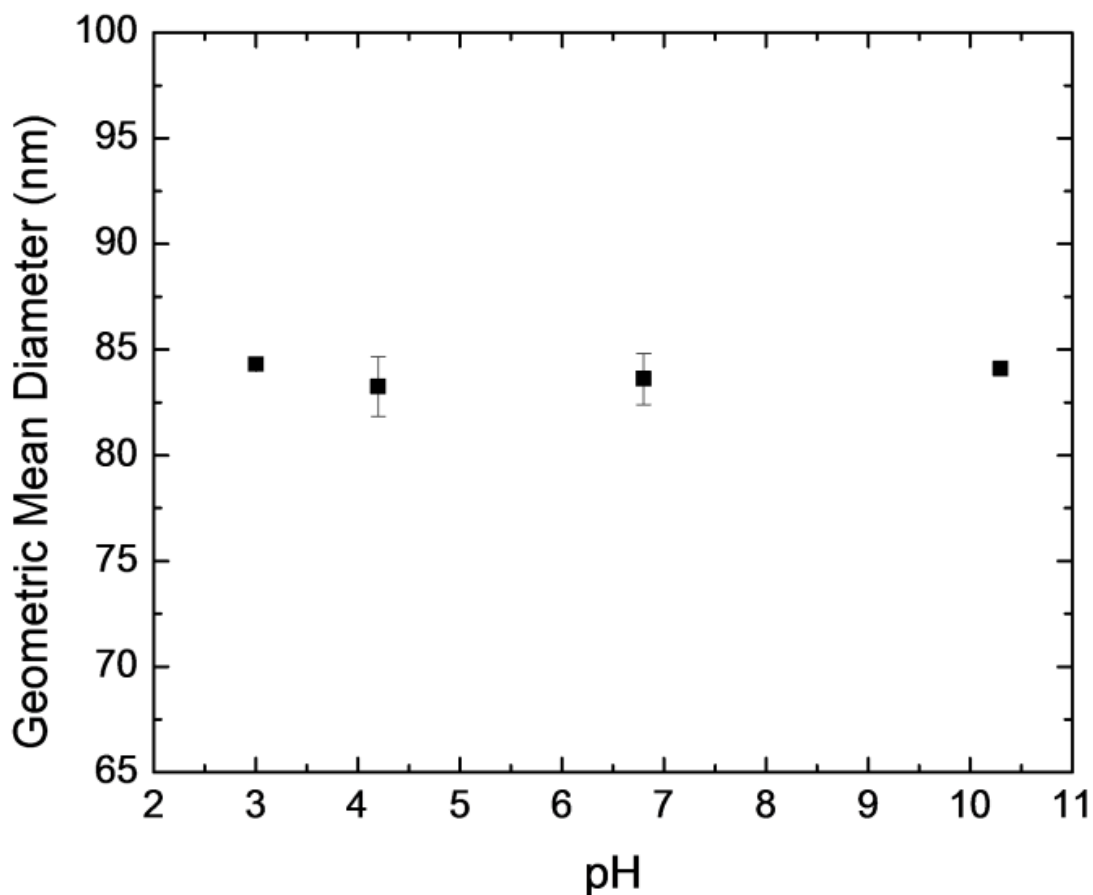


Fig. 12: pH effect on the particle size of crumpled GO particles measured by SMPS [35]. Copyright 2012, American Chemical Society.

2.2. Hydrothermal method

For preparing Fe_2O_3 nanospindles with crumpled reduced graphene oxide, Bai et al [46] synthesized graphite oxide from natural flake graphite by a modified Hummers method [47], then they dispersed the prepared graphite oxide and $\text{Fe}(\text{NO}_3)_3 \cdot 9\text{H}_2\text{O}$ (as a precursor for Fe_2O_3) in de-ionized water by ultrasonication for 30 min to form a solution A. Solution B was prepared by dissolving 10 mL $\text{NH}_3 \cdot \text{H}_2\text{O}$ in 10 ml ethylene glycol (EG). Solution B was then added dropwise into the solution A and allowed for stirring for 30 min at room temperature. After that, solution was transferred to a Teflon-lined stainless steel autoclave, then was heated to 200 °C for 10 h. After the autoclave had cooled down to room temperature, the resultant black product was separated by centrifuging, washed with de-ionized water and ethanol several times, and dried at 45 °C in a vacuum oven [46].

Typical FESEM images of crumpled reduced graphite oxide (CRGO)-Fe₂O₃ composite are shown in Fig. 13. From the low-magnification FESEM image (Fig. 13a), it can be clearly seen that the composite consists of many Fe₂O₃ nanoparticles and RGO nanosheets. The RGO nanosheets were naturally crumpled and curved with petal-like shapes. The Fe₂O₃ nanoparticles were densely and freely dispersed on the CRGO nanopetals. The high-magnification image (Fig. 13b) shows that the Fe₂O₃ nanoparticles were of spindle shapes. Some Fe₂O₃ nanospindles were supported by CRGO nanosheets, while others were wrapped in CRGO nanosheets, just like the rice-hull structure with parts of the hulls destroyed and their rice exposed in a pile of unhusked rice.

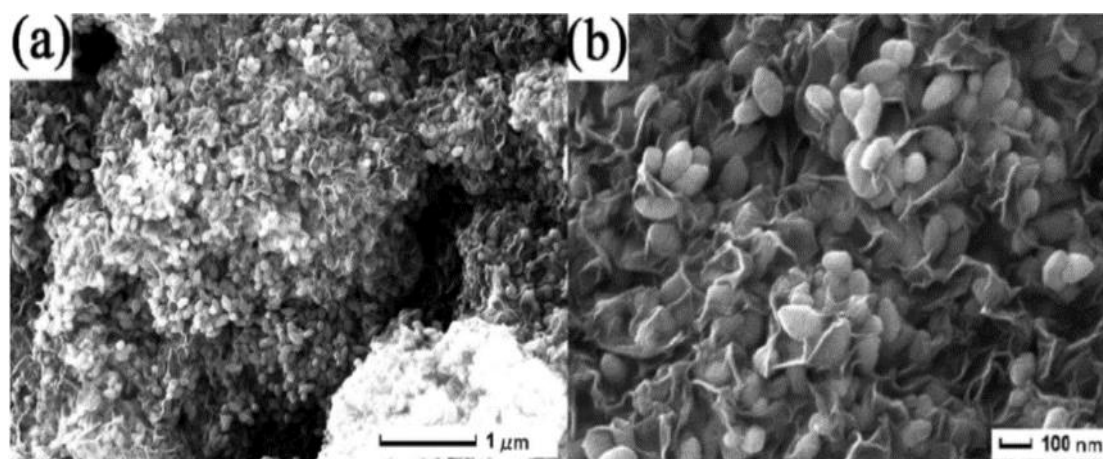


Fig. 13: (a, b) FESEM images of RGO-Fe₂O₃ composite [46]. Copyright 2012, The Royal Society of Chemistry

By the same method, crumpled reduced graphene oxide-poly(*p*-phenylenediamine) (rGO-PpPD) hybrids were prepared [48]. rGO-PpPD hybrids were prepared by heat treatment of GO [47] aqueous dispersion in the presence of *p*PD. In a typical run, 2 mL of GO dispersion (1 mg/ml) was added into 20 mL of H₂O, followed by addition of 0.2 g of *p*PD. After sonication for 10 min, this mixture was heated to 80 °C for 2 h. After that, the rGO-PpPD hybrids were collected by centrifugation at 10000 rpm for 10 min and washed with H₂O for twice to remove the excessive *p*PD.

SEM image of rGO-PpPD hybrids are shown in Fig. 14a. It is seen that the sample shows a typically crumpled morphology, a layer-like structure with a lateral dimension up to several micrometers, which is consistent with previous reports on crumpled

graphene-based materials. The crumpled morphology of rGO-PpPD hybrids thus obtained was also confirmed by the TEM image, as shown in Fig. 14b.

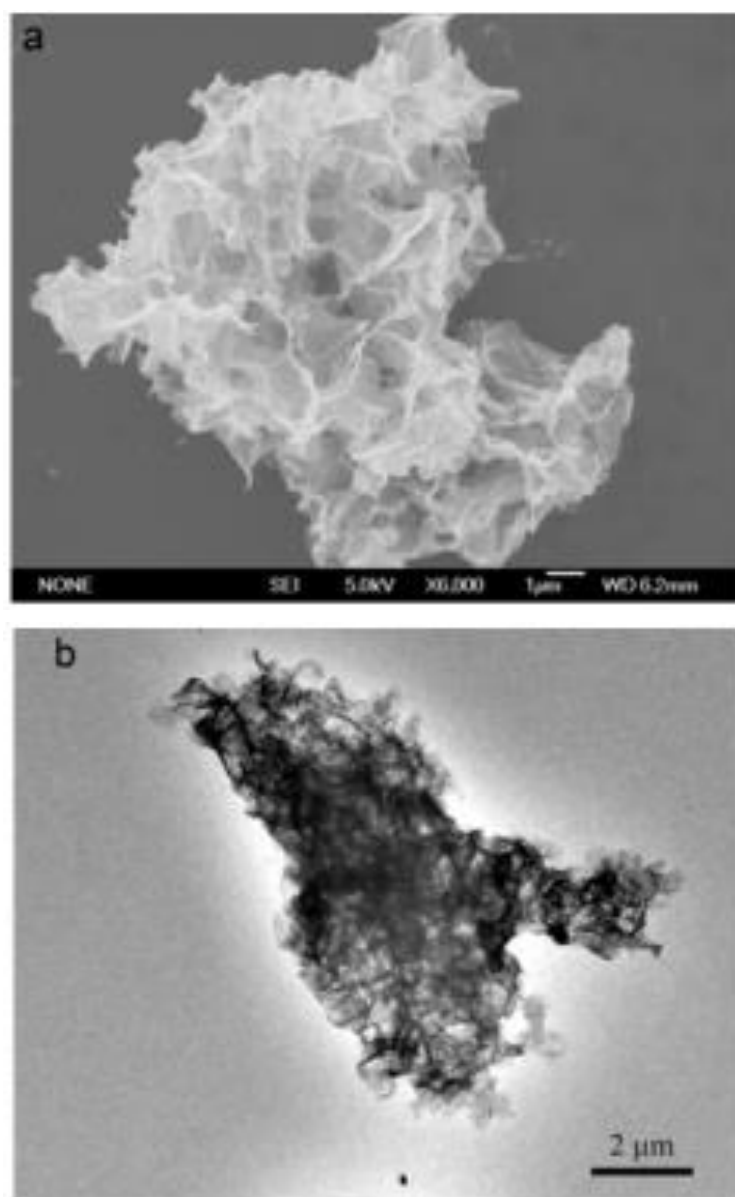


Fig. 14: (a) SEM and (b) TEM images of rGO-PpPD hybrids [48]. Copyright 2013, The Royal Society of Chemistry

2.3. Thermal reduction of graphene oxide method

Crumpled and planar graphene materials were prepared by hydrogen gas reduction of graphene oxide [49]. GO was deposited on nickel foam using electrophoretic deposition

(EPD). In EPD experiment, GO was dispersed in absolute ethanol by ultrasonication. In order to charge the GO, 10^{-5} to 10^{-4} mol of $\text{Mg}(\text{NO}_3)_2 \cdot 6\text{H}_2\text{O}$ were added into the suspension as electrolyte for EPD. Two 5 cm-diameter nickel foam were used as EPD electrodes, and were put into the suspension and kept parallel (see Fig. 15). A dc voltage of 50V for 13 min was applied on the EPD electrodes and thus the charged GO were attracted towards the cathode. Afterwards, the GO based electrodes were treated in a pure hydrogen gas environment at various temperatures from 300 to 600 °C for 30 min each with a ramping speed of 2 °C per min.

The morphological structure of the bare nickel foam and hydrogen gas treated graphene oxide (hGO) covered nickel foam treated respectively at 500 and 600 °C were investigated by SEM and shown in Fig. 16. For the bare nickel foam, its porosity is slightly above 95%, with an original thickness of 1.6 mm. The intrinsic open cell structure of the foam, as shown in Fig. 16a, provides a lot of space for graphene materials to deposit, as illustrated in Fig. 16b.

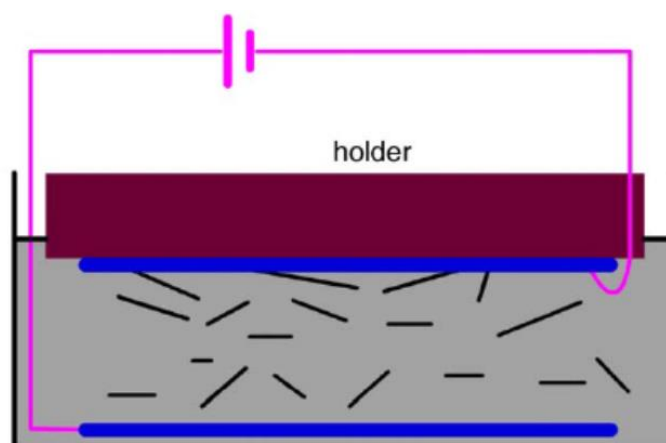


Fig. 15: Schematic diagram of the electrophoresis process for the deposition of GO [50]. Copyright 2006, Elsevier.

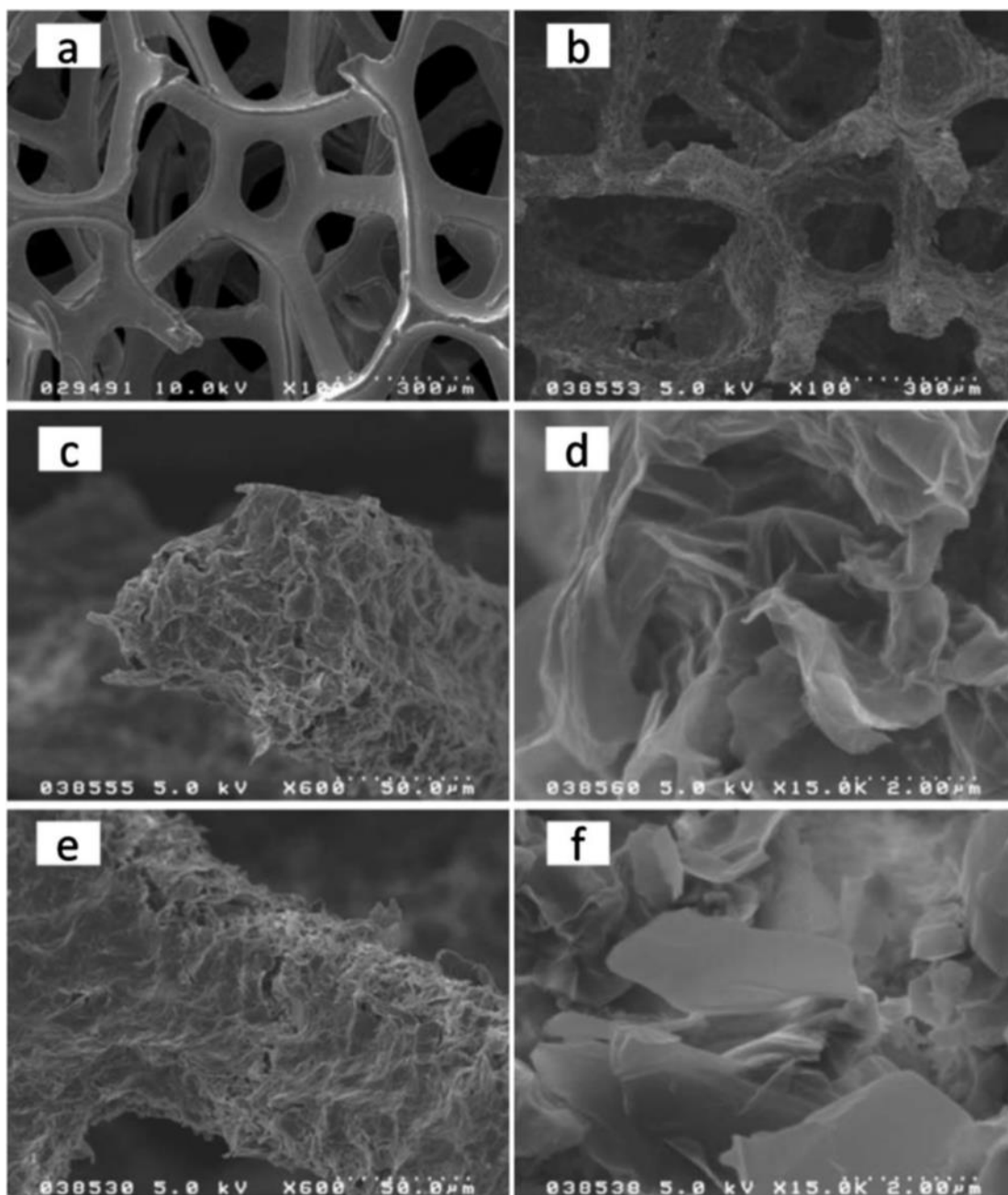


Fig. 16: SEM images of bare nickel foam (a), hGO covered nickel foam treated at 500 °C (b–d) and 600 °C (e and f) with different magnifications [49]. Copyright 2013, The Royal Society of Chemistry.

Satisfactory deposition uniformity was achieved by using EPD. At higher magnifications in Fig. 16c and d, the hGO materials treated at 500 °C were crumpled rather than flat and similar structures were found when treated at 300 and 400 °C. During the removal of oxygen containing groups over this temperature range, the graphene basal plane was wrinkled due to the local strain difference induced by the breakage and reformation of chemical bonds [49]. The crumpled structure contributed to the separation of graphene layers. Conversely, the hGO material started to be graphitized into a more layered but flatter sheet structure, as shown in Fig. 16e and f, when the treatment temperature increased to 600 °C [49].

Flame induced reduction method was used for preparation of reduced crumpled graphene [51]. Firstly, the GO [47] powder was impregnated by a flammable polar solvent such as ethanol, methanol and acetone. The wet GO powder was ignited using an ordinary matchstick under ambient conditions (Fig. 17). Immediately, the fluffy black powder was floated over the flame and collected by the metal wire mesh. Interestingly, this reduction process was very rapid and the GO powder was partially reduced, as indicated by the color change from deep brown to black. The possible mechanism based on the flame induced reduction of GO assisted by flammable polar solvents was investigated. The precursor GO, as synthesized by liquid phase oxidation and intercalation of natural graphite, exhibits an expanded interlayer space of up to 0.6–0.8 nm and highly hydrophilic surface. The material will be easily solvated or swelled when exposed to vapor or immersed in polar liquid solvents. Additionally, the flame is the visible, gaseous part of fire, which is caused by a highly exothermic reaction taking place in a thin zone. If hot enough, the gases may become ionized to produce plasma. Sufficient energy in the flame will excite the electrons in some of the transient reaction intermediates (e.g. carbon free radicals), resulting in the emission of visible light as these substances release their excess energy. Taking ethanol as an example, the GO powder can be swelled after mixing with ethanol. The combustion of ethanol provides not only high temperatures but also carbon sources. Thus, the GO powder can be reduced within several seconds without any metal catalysts [51].

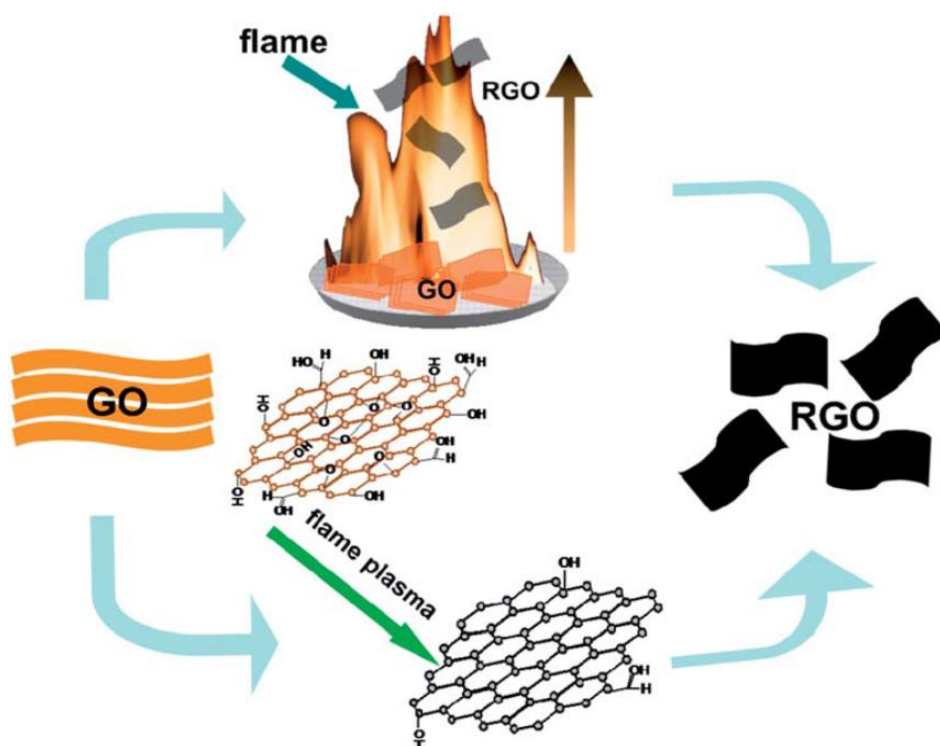


Fig. 17: Schematic illustration of preparation of rGO by a flame induced reduction method [51]. Copyright 2014, The Royal Society of Chemistry.

From the FESEM images (Fig. 18a-c), all rGO samples exhibit a typical curved/wrinkled appearance, as a result of the decomposition of the oxygen functional groups that leads to graphene-like sheets with a disordered stacking. Notably, for graphene, contact between different regions of graphene could lower the total energy through van der Waals cohesion and stabilize the crumpled phase [17].

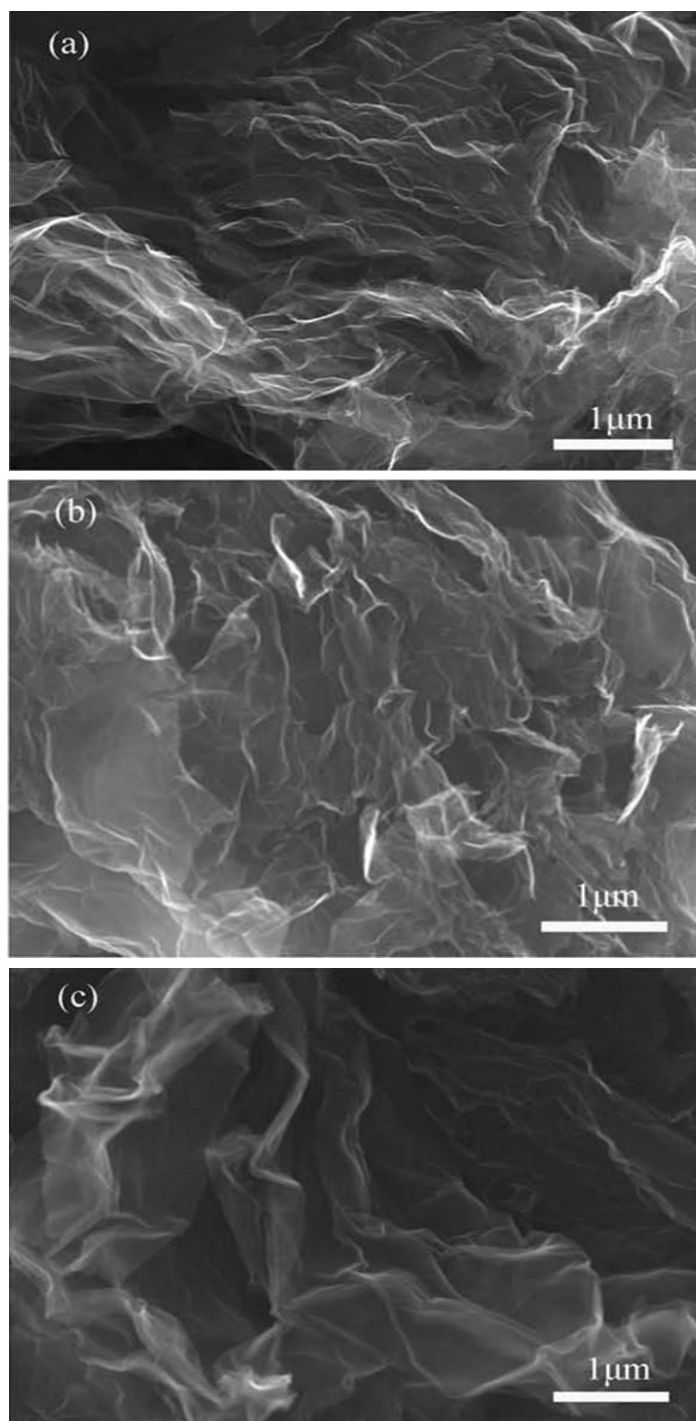


Fig. 18: SEM images of (a) ethanol-rGO, (b) acetone-rGO and (c) methanol-rGO [51]. Copyright 2014, The Royal Society of Chemistry.

2.4. Fast cooling method

Highly crumpled graphene sheets (HCGSs) have been prepared through freezing a chemically reduced graphene oxide (CRG) aqueous suspension using liquid nitrogen [52]. As described in Fig. 19, GO dispersion was sonicated for 30 min. Then, hydrazine solution was added and the dispersion was transferred in a 250 mL round-bottom flask and the pH of the suspension was adjusted to 10 using dilute sodium hydroxide solution, then refluxed at 100 °C for 24 h. Subsequently, the solid was filtered, and washed several times with distilled water. Afterwards, the black solid was added into 500 mL of distilled water and sonicated for 1 h to form dispersion, which was immediately frozen with liquid nitrogen. The frozen solid was transferred into a house domestic refrigerator for 12 h. Finally, the ice solid was melted naturally at room temperature, filtered and dried at 100 °C for 12 h in a vacuum oven. For comparison purpose, Yan et al [52] synthesized the frozen chemically reduced graphene (FCRG) sample according to the above process without the freezing with liquid nitrogen but was frozen in a domestic refrigerator (-4 °C).



Fig. 19: schematically describes the whole synthetic procedure for the fabrication of HCGSs [52]. Copyright 2013, The Royal Society of Chemistry

From the SEM image, it can be observed that each individual graphene sheet aggregates with each other to form big, thick and dense particles in dry state (Fig. 20a). After the freezing treatment using liquid nitrogen, the resulting HCGSs exhibit porous structure composed of numerous crumpled and curved sheets (Fig. 20b, c). There are considerable macropores with the diameters ranging from several hundred nanometers to a few micrometers [52].

TEM observations of the HCGSs show obvious crumpled structure and folded regions in their basal planes (Fig. 21a, b). It is worth noting that the faster cooling is, the more crumpled wrinkles form on the sheets, meaning that fast growth speed of ice crystal is favorable for the formation of crumpled and folded graphene [52]. More interestingly, abundant pores with the sizes of ~ 2 nm induced by tiny ice crystal punching are clearly observed on the sheets of HCGSs (Fig. 21c). In the case of FCRG, it exhibits relatively less crumples compared with HCGSs but more than CRG while retaining the two-dimensional planar structure (Fig. 20d and Fig. 21d).

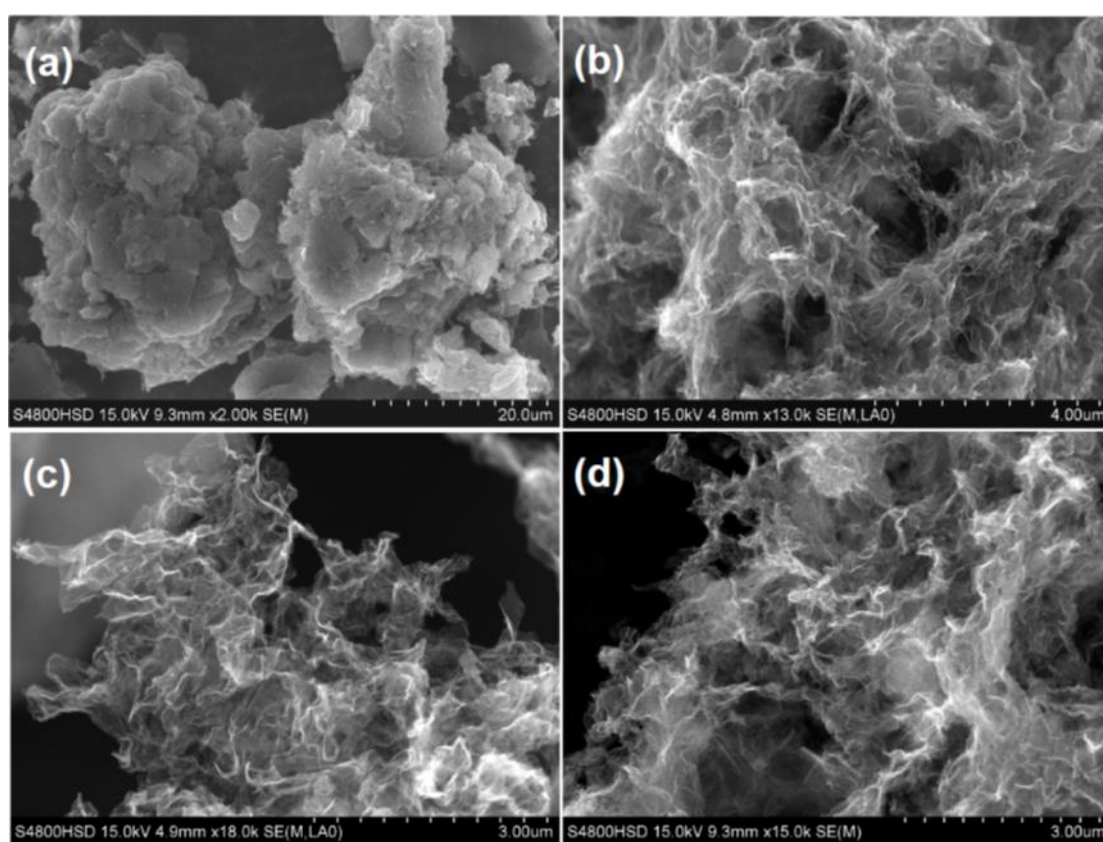


Fig. 20: SEM images of (a) CRG, (b, c) HCGSs and (d) FCRG [52]. Copyright 2013, The Royal Society of Chemistry

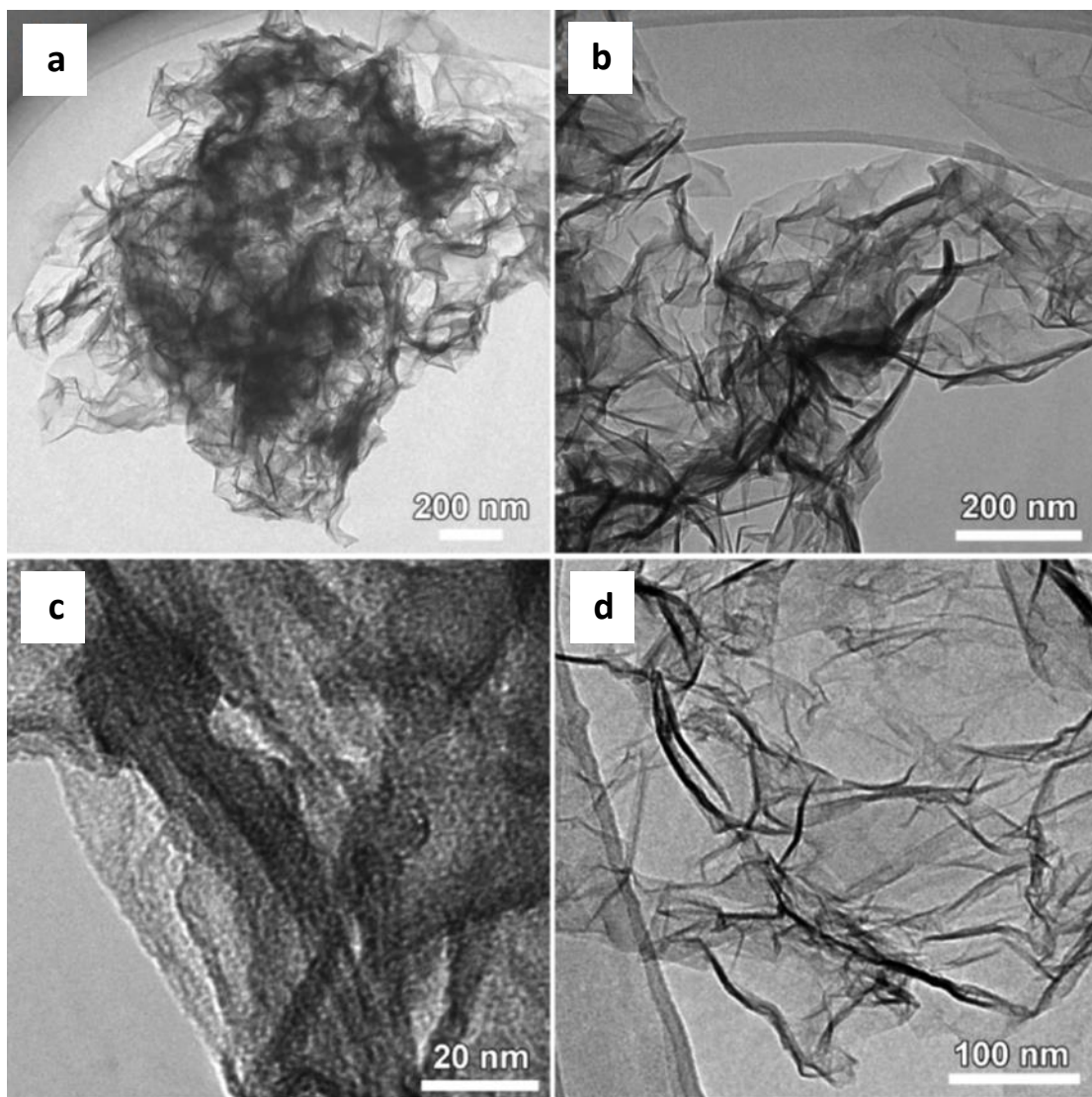


Fig. 21: TEM images of (a-c) HCGSs and (d) FCRG [52]. Copyright 2013, The Royal Society of Chemistry

2.5. Mechanical method

2.5.1. Fabrication of graphene paper

Electrolyte-mediated graphene paper was fabricated according to the method reported previously [53, 54]. 100 mL 0.5 mg mL⁻¹ of highly concentrated graphene oxide (GO) solution was mixed with 0.2 mL hydrazine (35 wt% in water) and 0.35 mL ammonia (28% wt% in water) in a glass jar. The jar was heated in an oil bath (~100 °C)

with vigorous stirring for 3 hr. The reduced graphene oxide solution was then ready for further use.

Graphene paper in the form of hydrogel was formed by vacuum filtration of the as prepared reduced graphene oxide solution through a mixed nitrocellulose filter membrane (47 mm in diameter, 0.05 mm pore size) [55]. The vacuum was immediately disconnected once no reduced graphene oxide solution was left on the surface of filtrated graphene paper. The thickness of each graphene paper fabricated can be controlled by adjusting the volume of the reduced graphene oxide solution. After removing the remaining ammonia and hydrazine by deionized water, the graphene paper was immersed in 5 M H₂SO₄/H₂O miscible solution for 24 hour. The electrolyte of H₂SO₄ was then exchanged with water in the hydrogel of graphene paper and trapped between graphene sheets in graphene paper after vacuum treatment (Fig. 22)[55]. Then the electrolyte mediated graphene paper is ready for further use.

2.5.2. *Crumpling and unfolding graphene paper*

Fig. 23(a–c) illustrate the procedure for crumpling graphene papers bonded on elastomer films. A square-shaped elastomer film, VHB acrylic 4910 with thickness of 1 mm was biaxially stretched along two orthogonal in-plane directions by strains of $\epsilon_{pre1} = \Delta L_1/L_1$ and $\epsilon_{pre2} = \Delta L_2/L_2$, where L_1 and L_2 are the side lengths of the undeformed elastomer, and ΔL_1 and ΔL_2 are the corresponding changes in lengths in the deformed elastomer (Fig. 23). Since the elastomer film is highly stretchable, the pre-strains ϵ_{pre1} and ϵ_{pre2} are set in a range from 50% to 400%. The as-prepared graphene paper was then bonded onto the pre-strained elastomer film by a dry-transfer method [18] (Fig. 22). Thereafter, the pre-strains in the elastomer film were relaxed along two directions sequentially (Fig. 22, Figs. 23(a–c)) to crumple the graphene paper [55].

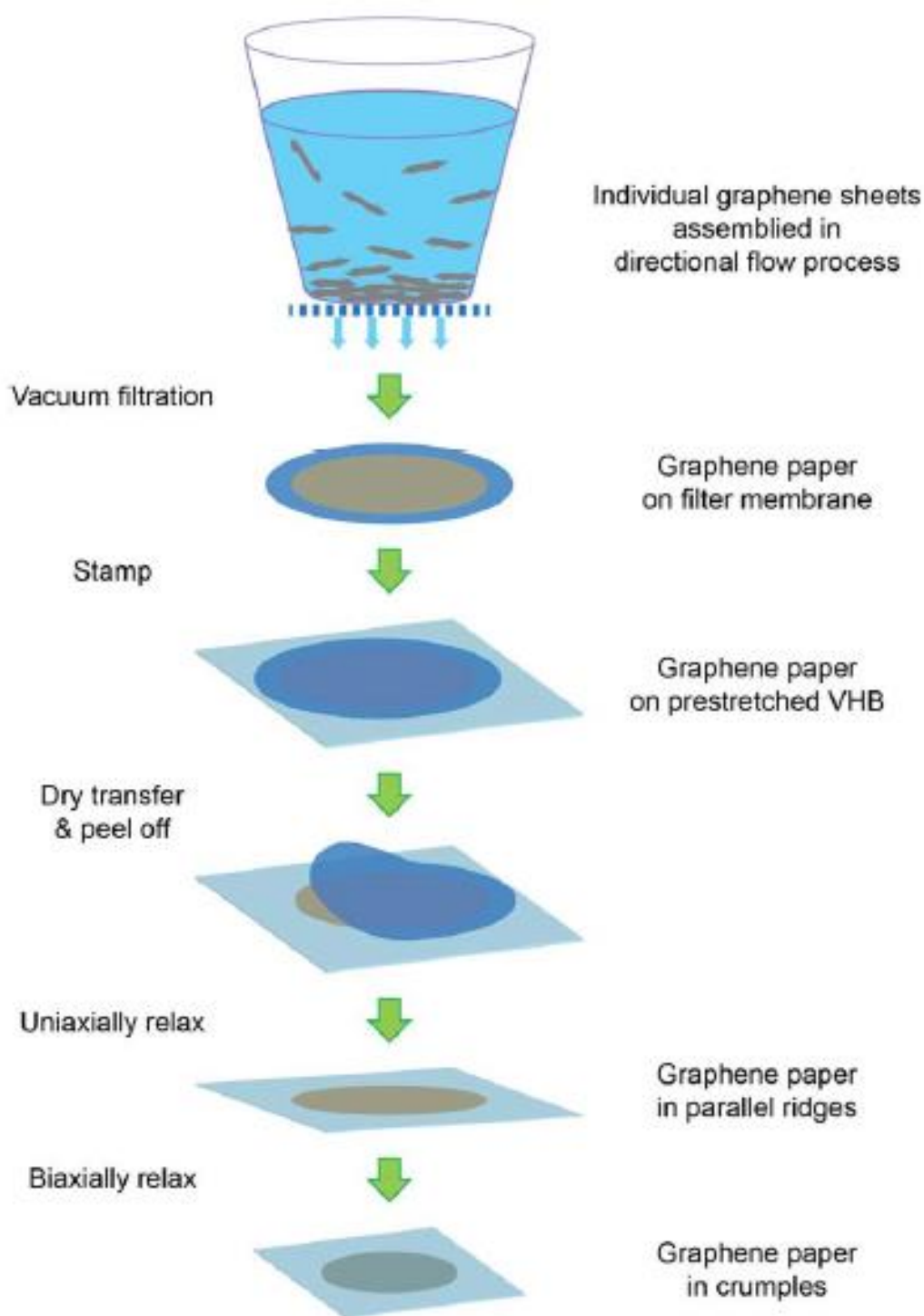


Fig. 22: Schematic illustration of the fabrication process of the crumpled graphene paper [55]. Copyright 2014, Nature Publishing Group.

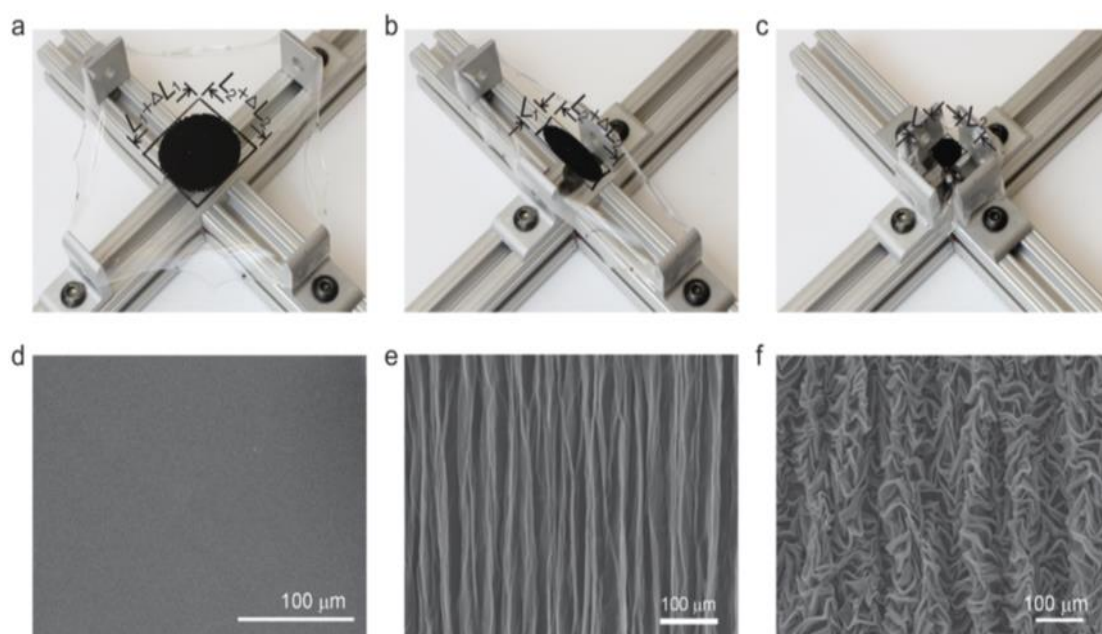


Fig. 23: Fabrication of crumpled-graphene papers. (a–c) Photographs of the simple procedure for crumpling the graphene papers: (a) a flat graphene paper is bonded on a biaxially pre-stretched ($\epsilon_{\text{pre}1} = \epsilon_{\text{pre}2} = 400\%$) elastomer film, which is then (b) uniaxially and (c) biaxially relaxed. (d–f) SEM images of microscopic patterns formed in the graphene paper: (d) the initially flat graphene paper forms (e) parallel ridges as the elastomer film is uniaxially relaxed, and (f) crumpled patterns as the film is biaxially relaxed. The thickness of the graphene paper is, 2 mm measured at dehydrated state [55]. Copyright 2014, Nature Publishing Group.

2.5.3. Crumpling control

Because crumpling of graphene can strongly affect its properties and the performance of graphene-based devices and materials [9, 56-59], it is highly desirable to control reversible wrinkling and crumpling of graphene. Although it has been shown that thermal expansion and substrate regulation can induce reversible wrinkling of graphene [60-63] and capillary compression can crumple microscopic graphene flakes into particles [9, 32], it is still not clear how to reversibly crumple and unfold large-area graphene films in a controlled manner.

The controlled folding and unfolding of crumpled graphene films has been demonstrated by [18]. They reported an approach to reversibly control the crumpling and unfolding of large-area graphene sheets. They show with experiments, atomistic simulations and theory that, by harnessing the mechanical instabilities of graphene

adhered on a biaxially pre-stretched polymer substrate and by controlling the relaxation of the pre-strains in a particular order, graphene films can be crumpled into tailored self-organized hierarchical structures.

Zang et al [18] deposited a film of few-layer graphene (3-10 layers) on a nickel film by chemical vapour deposition and then transferred to a polydimethylsiloxane (PDMS) stamp. An elastomer film based on acrylic is biaxially stretched to three to five times its original dimensions (that is, pre-strained by 200-400%) and held at the pre-stretched state. The graphene film is then transferred to the pre-stretched elastomer substrate by stamping [60]. Thereafter, the pre-strains in the substrate are relaxed sequentially along two pre-stretched directions, as illustrated in Fig. 24a. During relaxation, the lateral dimensions of the transferred graphene film reduce macroscopically by the same ratio as those of the substrate. Microscopically, however, the graphene film develops wrinkles (Fig. 24b) and delaminated buckles (Fig. 24c) when the substrate is relaxed uniaxially, and becomes crumpled (Fig. 24d) when the substrate is relaxed biaxially. If the relaxed substrate is biaxially stretched back, the crumpled graphene film can be unfolded to a relatively flat state (Fig. 24e). The crumpling - unfolding process is reversible over multiple cycles under the control of substrate deformation (Fig. 25). The method is also applicable to few-layer graphene grown on copper films.

The basic mechanisms that control the crumpling and unfolding of graphene were discussed by [18]. As the pre-stretched substrate is gradually relaxed along one direction, the apparent length of the graphene film reduces from L_0 at the initial (flat) state to L at the present state (Fig. 24a). The macroscopic compressive strain in the graphene film along the relaxed direction was defined as (Eq. 1) [18]:

$$\varepsilon_G = \frac{(L_0 - L)}{L_0} \quad (1)$$

The compressive strain in graphene can be calculated as (Eq. 2) [18]:

$$\varepsilon_G = \frac{(\varepsilon_{pre} - \varepsilon)}{(\varepsilon_{pre} - 1)} \quad (2)$$

Where ε_{pre} is the pre-strain of the substrate and ε is the tensile strain in the substrate at the present state. When the compressive strain in the graphene film reaches a critical value, wrinkles develop with an initial wavelength (Eq. 3)[18, 61, 64, 65].

$$\lambda_0 = 2\pi h \left[\frac{E}{12\Lambda\mu_s(1-\nu^2)} \right]^2 \quad (3)$$

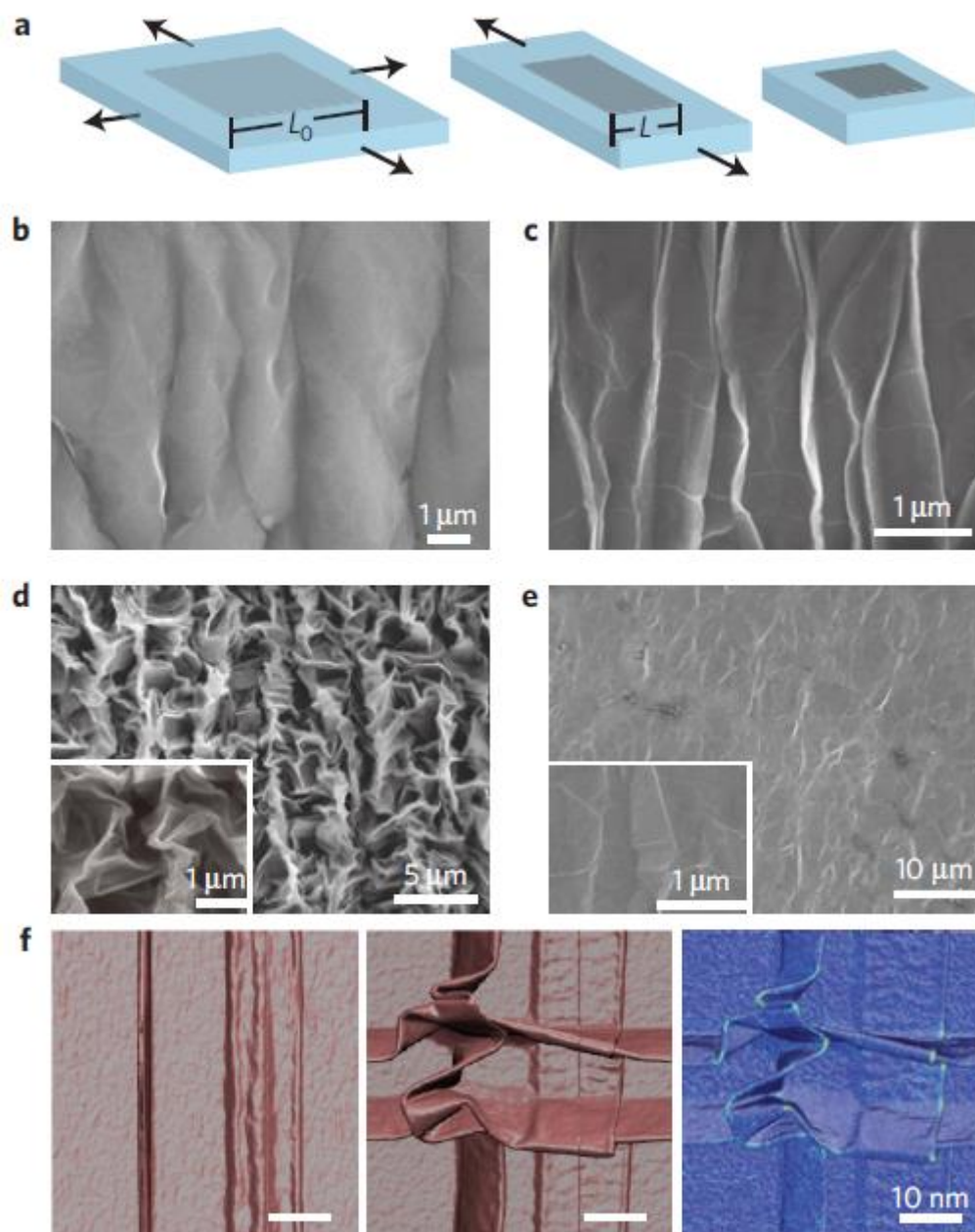


Fig. 24: Controlled crumpling and unfolding of large-area graphene sheets. **a**, Schematic illustration of macroscopic deformation of a graphene sheet on a biaxially pre-stretched substrate. **b–e**, SEM images of patterns developed on the graphene sheet: first wrinkles form (**b**), then delaminated buckles as the substrate is uniaxially relaxed (**c**), followed by crumples as the substrate is biaxially relaxed (**d**), which unfold as the substrate is biaxially stretched back (**e**). **f**, Atomistic modelling results of the crumpling of a single-layer graphene under uniaxial compression, and biaxial compression, followed by a visualization of the Mises stress distribution (from left to right). Stress concentrations (visualized in red) are observed near highly deformed regions [18]. Copyright 2012, Nature Publishing Group.

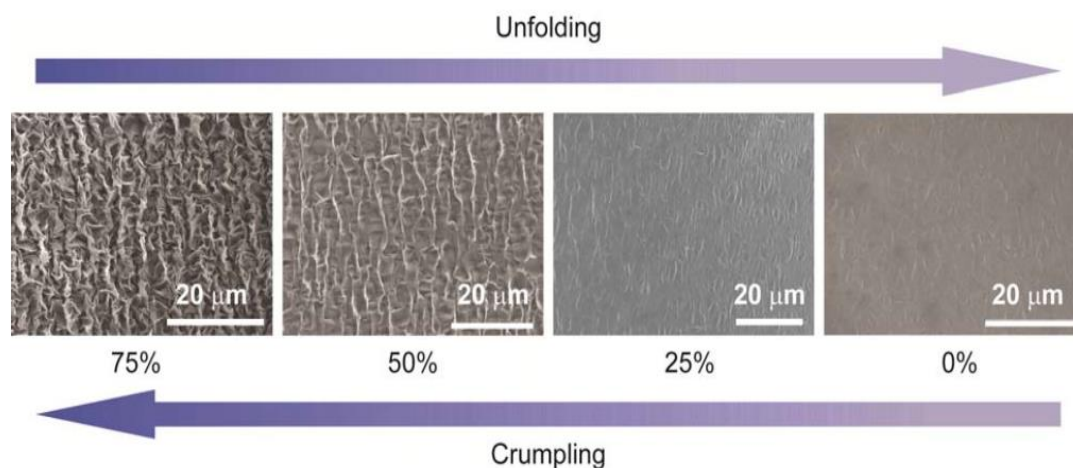


Fig. 25: Reversible crumpling and unfolding of a graphene film by controlling the biaxial compressive strain in the graphene through stretching/relaxing the polymer substrate. SEM images of the graphene film under various biaxial compressive strains: 75%, 50%, 25%, and 0% [18]. Copyright 2012, Nature Publishing Group.

Where E and ν are Young's modulus and Poisson's ratio of graphene, respectively, μ_s the shear modulus of the substrate taken to be a neo-Hookean material, h the thickness of the graphene film and $\Lambda = (1 + (1 + \varepsilon_{pre})^3)/2(1 + \varepsilon_{pre})$. Taking $E = 1$ TPa, $\nu = 0.165$, $\varepsilon_{pre} = 200\%$ and $\mu_s \approx 20$ kPa, They obtain $\lambda_0 \approx 611h$ [66]. Because the number of graphene layers ranges from 3 to 10, the initial wavelength is evaluated to be 0.6-2.1 μm , consistent with experimental results (Fig. 24b) [18, 61, 65].

Under further uniaxial compression, a pattern of parallel ridges develops with wavelengths of 0.2 - 2 μm (Fig. 24c). By sectioning the graphene film, Zang et al [18] find that the ridges are due to buckling of delaminated regions of the graphene on substrate. The delaminated buckles may initiate from the hills of the wrinkles of graphene [67] and/or defects on the graphene/polymer interface [67-69]. Once initiated, the delaminated buckles will propagate until the decrease of the graphene-substrate system's elastic energy balances the increase of its interfacial energy [67-69]. Macroscopic and microscopic delaminations of films on compressed substrates have been extensively studied [67, 68] and applied [70, 71]. However, the first observation of patterns of delaminated buckles in large-area graphene films on polymer substrates was presented by Zang et al [18], which is assessed using a close integration of experiment and atomistic simulation.

The crumpling of graphene films under biaxial compression leads to a surface structure that is distinct from the one formed under uniaxial compression. As discussed above, a pattern of parallel delaminated buckles forms in graphene on the substrate when relaxed in one direction (Fig. 24c). As the substrate is subsequently relaxed in the other direction, the delaminated buckles are compressed along their ridges, and thus buckle and collapse (Fig. 24d). Furthermore, a new set of delaminated buckles develop perpendicular to the previous ones. The intersection of two orthogonal buckles gives rise to an interesting crumpling pattern with ridges and vertices (Fig. 24d). Complementary atomistic simulation done by Zang et al reveals high stress concentrations around the ridges and vertices, as shown in Fig. 24f [18]. If the substrate is simultaneously relaxed in the two directions, the crumpling also occurs but leads to more irregular patterns. Furthermore, it is noted that the crumpling of delaminated graphene is distinct from the hierarchical folding of perfectly bonded films under biaxial compression that was reported [72]. Once the relaxed substrate is biaxially stretched (to its initial length), the parts of the graphene film adhered on the substrate will pull on the delaminated parts, unfolding the crumpled graphene film (Fig. 24e). If the stretched substrate is relaxed again, the crumpling will reoccur. The graphene film can maintain its integrity over multiple crumpling - unfolding cycles (that is, >50) with a few unconnected cracks emerging (Fig. 24e) [18].

3. Applications

Due to the unique structural property, graphene is provided with a series of prominent intrinsic chemical and physical features, such as strong mechanical strength (~ 1 TPa) [66, 73], extraordinarily high electrical and thermal conductivity [74-76], and large surface area ($2675 \text{ m}^2/\text{g}$) [77]. These outstanding and intriguing features make this extremely versatile carbon material promising for various practical applications, including high-performance nanocomposites [4, 78], transparent conducting films [74, 75, 79], sensors [80, 81], actuators [82-84], nanoelectronics [85, 86], and as promising electrode material for energy storage devices [87-89].

Two-dimensional (2D) shape of graphene is desirable for many of its applications, it actually limits graphene's potential to be fully realized in scaled up energy devices. For example, 2D graphene sheets can easily stack to form lamellar microstructures parallel to the current collectors, especially when compressed during electrode preparation. This could affect the device performance adversely in two ways: The effective surface area of the electrodes can be reduced due to aggregation of graphene sheets. The horizontal alignment of the graphene stacks can hinder electron and ion transport since both prefer the direction perpendicular to the current collector [17]. This makes it hard to achieve scalable device performance as the loading level of the active material increases.

To solve these problems, several general methods have been developed. Within the paradigm of colloidal chemistry one can introduce electrostatic repulsion between the sheets by chemically tuning the surface charge of graphene and tailoring the graphene - solvent interactions [90-92]. On the other hand, one can insert molecular or nanostructured spacer materials to prevent the stacking of graphene sheets [93]. However, it is not obvious how these two approaches can alter the orientation of graphene lamella. Alternative strategy was developed for making graphene resist aggregation by crumpling the 2D sheets into fractal-dimensional paper-ball-like structure [9]. Like paper balls, crumpled graphene balls are remarkably aggregation-resistant [17]. They are dispersible in nearly arbitrary solvents without the need for additional chemical functionalization and remain individually dispersible even after high-pressure compression. Since crumpled graphene balls have more open structure, they have higher specific surface area than the stacked flat sheets.

3.1. Crumpled graphene for supercapacitor

Supercapacitors (also known as electrochemical capacitors (ECs) or ultracapacitors), represent a unique class of electrical energy storage devices, which has attracted increasing attention because of their high power density, fast charge–discharge rate and long cycle life [94]. ECs can be classified into electrical double layer capacitors (EDLC) and pseudo-capacitors (PC) [95]. Due to their high power densities and long-term cycling stability, EDLCs have been extensively explored and become a promising device in high power electronic devices, electric vehicles (EVs) and hybrid electric vehicles (HEVs) [96].

Crumpled graphene balls (CGB), a new type of carbon with a crumpled sphere structure of the graphene sheet, have recently been prepared from aqueous graphene oxide (GO) nanosheets by capillary force associated with rapid drying of the solvent and physical deformation through an aerosolization process as described previously [9, 26, 27, 35, 36, 97-99]. This process could transfer the graphene from a 2D sheet to a 3D crumpled structure, which has higher specific surface area than the stacked 2D graphene sheets [9]. Of more interest, the CGB structure is rigid and can easily sustain its structure after being immersed in an electrolyte solution and is remarkably aggregation-resistant [9]. Though the CGB structure contains a lot of advantages, there is still a need to further improve its efficiency in mass transport, electron transfer, and utilization [100].

Many authors [101-105] used graphene in supercapacitors due to its high electrochemical performance but, the main obstacle face them is the aggregation of the reduced graphene sheets and dramatically decreases the surface area, leading to a poor capacitance [96]. For increasing the surface area and decreasing the agglomeration of the reduced graphene sheets great efforts were devoted to crumple the graphene sheets [38].

Nitrogen-doped and crumpled graphene sheets were used for improving the supercapacitance [38]. Graphene oxide was pre-treat by a facile thermal expansion method followed by nitrogen doping into graphene oxide (NtGO) with a hydrothermal process with hexamethylenetetramine (HMT). The thermal expansion process makes the produced graphene crumpled, which can suppress the aggregation of graphene sheets during the subsequent drying process after hydrothermal doping. HMT acts as

both reducing agent and N source for doping and the consecutive hydrothermal process enabled the nitrogen doping reaction to proceed on both sides of GO, leading to uniform nitrogen doping in graphene. This differs from the nitrogen doped graphene produced using ammonia gas as the nitrogen source, in which the reaction mostly occurred on the exposed surface of carbon nanostructures, thereby resulting in inhomogeneous [96] and low nitrogen doping, of the order of 2–3 at% [106].

The thermal expansion on the supercapacitance of nitrogen-doped graphene nanosheets was investigated by Zou et al [38]. Fig. 26a shows the cyclic voltammetry (CV) curves of different electrodes at the scan rate of 20 mV s^{-1} . There is no distinctive peak in the CV curve of tGO while a pair of redox peaks in the CV curves of NRGO and NtGO were observed, which are caused by the nitrogen doping induced pseudo-capacitance [107]. The rectangular CV curves indicate the ideal double layer capacitor nature with a charge–discharge process. Additionally, the cell with NtGO electrode (red line) exhibits much larger current than the electrode of tGO (black) and NRGO (blue), indicating increased capacitance due to thermal expansion. The improved capacitance of NtGO can also be observed from the galvanostatic charge–discharge curves at a discharge current density of 1 A g^{-1} as shown in Fig. 26b. The specific capacitance of NtGO is 270 F g^{-1} at the current density of 1 A g^{-1} (Table 1), while those of tGO and NRGO are 121 and 169 F g^{-1} respectively. The energy density (E) of NtGO at current density of 1 A g^{-1} is 24 Wh kg^{-1} [38]. The capacitance retention of NtGO is 97% after 2000 cycles. The results again highlight that NtGO has excellent electrochemical stability and a high degree of reversibility [38].

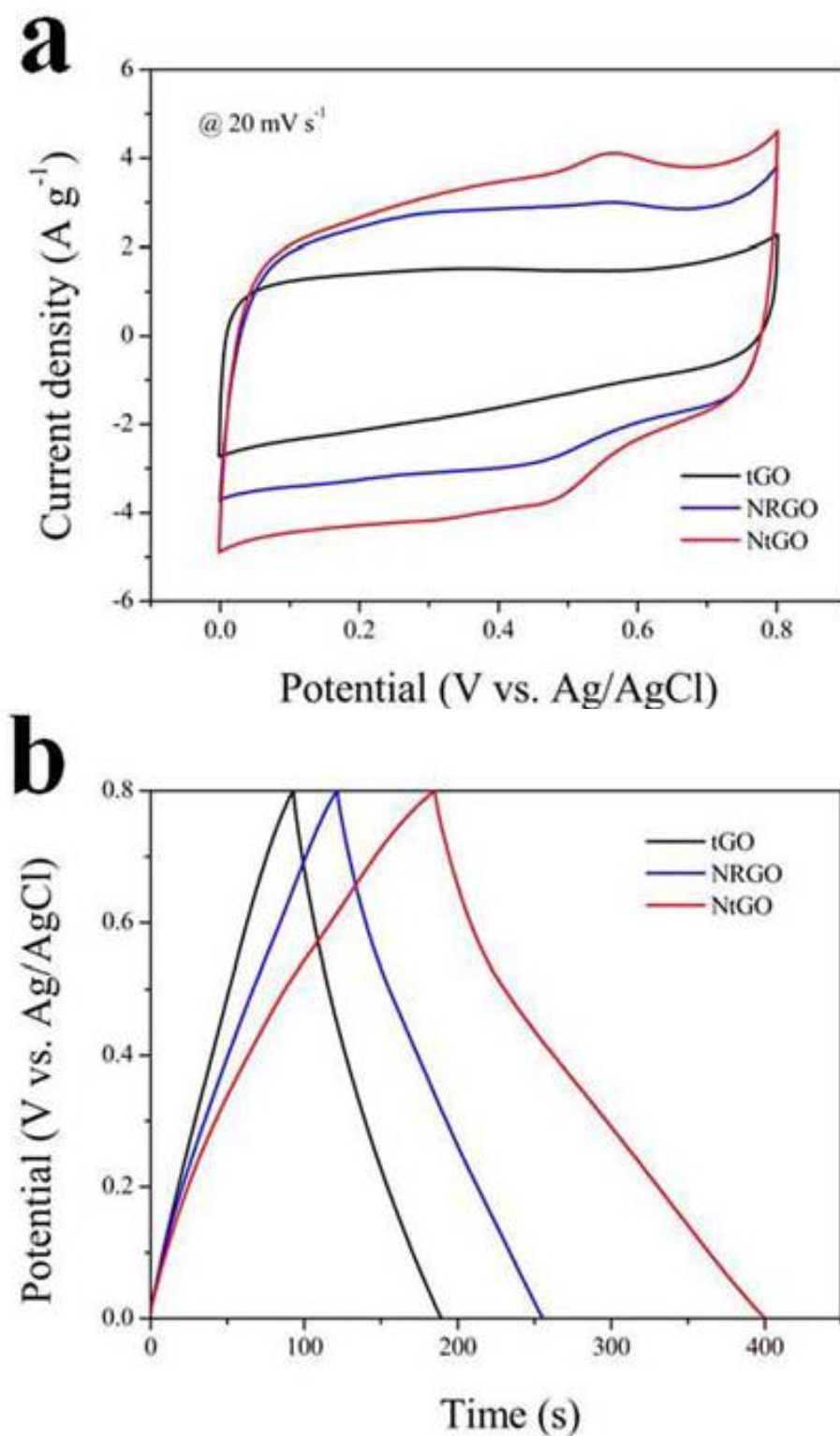


Fig. 26: Electrochemical performance of tGO, NRGO and NiGO using a three-electrode cell in 1 M H_2SO_4 . (a) CVs of as-prepared samples at the scan rate of $20\ mV\ s^{-1}$. (b) Galvanostatic charge-discharge curves of as-prepared samples at discharge current density of $1\ A\ g^{-1}$ [38]. Copyright 2014, The Royal Society of Chemistry.

Wen et al [96] synthesized crumpled nitrogen-doped graphene (C-NGNSs) with low cost and effectively at a very high yield. The C-NGNSs show unique crumpled structures with a high pore volume as high as $3.42 \text{ cm}^3 \text{ g}^{-1}$ and high nitrogen doping. These unique properties endow them as a promising electrode for supercapacitors with high capacity, excellent rate capability, and long-term stability. The C-NGNSs calcined at $900 \text{ }^\circ\text{C}$ (C-NGNSs-900) possess a specific capacitance of approaching 248.4 F g^{-1} at 5 mVs^{-1} (Table 1), which is four times and twice higher than the specific capacity for thermally reduced graphene sheets (TRGSs) (51.7 F g^{-1}) and chemically-reduced graphene (106.3 F g^{-1}), respectively, the electrolyte was $1.0 \text{ M [Bu}_4\text{N]BF}_4$ acetonitrile (CH_3CN) solution. Notably, the capacitance shows only a slight decrease to 183.3 F g^{-1} even at a scan rate of $1,000 \text{ mV s}^{-1}$, while the TRGSs and chemically-reduced graphene only show a capacity of 26.73 and 71.04 F g^{-1} at the same scan rate, suggesting a good rate capability for C-NGNSs-based supercapacitors. The specific capacitance for TRGSs-900 was calculated as 245.9 , 238.8 , 233.3 , and 226.5 F g^{-1} at current densities of 1.0 , 2.0 , 5.0 , and 10.0 A g^{-1} , respectively [96].

The electrochemical stability of C-NGNSs-900-based supercapacitors with organic electrolytes was evaluated using the galvanostatic charge–discharge technique at a current density of 1.0 A g^{-1} . It retained about 96.1% of the initial capacitance after 5000 cycles. These results again highlight that C-NGNSs have excellent electrochemical stability and a high degree of reversibility [96].

Crumpled nitrogen-doped graphene–ultrafine Mn_3O_4 nanohybrids (CNGMNs) were synthesized under hydrothermal conditions [108]. They used the prepared nanohybrids CNGMNs materials as electrodes for supercapacitors, which exhibit improved capacitance approximately 6 times better than that of the Mn_3O_4 counterpart and display exceptional rate capability and cycling stability ($\sim 98.7\%$ retention after 2000 cycles)[108]. Such anomalous electrochemical performances compared with Mn_3O_4 and $\text{rGO-Mn}_3\text{O}_4$ are mainly due to nitrogen-doping with a high content ($5.04 \text{ atom}\%$) in the graphene lattice, which provides active sites for adsorbing ions and accelerating electron transfer and also participates in electrochemical reactions directly accompanying the high electrochemical utilization of well-dispersed ultrafine Mn_3O_4 nanoparticles on the crumpled NG sheets [108]. This method may also be used for

hybridization of crumpled nitrogen doped graphene with other metal oxides for the development of novel high-performance supercapacitors.

The specific capacitances of the CNGMNs electrode at current densities of 1, 2, 3, 4, and 5 A g⁻¹ were measured to be 205.5, 185.6, 166.6, 158.2 and 152.3 F g⁻¹, respectively (Fig. 27, Table 1) [108]. It is evident that the specific capacitance of CNGMNs slightly decreases with the increase of charge–discharge rates, suggesting outstanding rate capability of the CNGMNs electrode. Even at 10 A g⁻¹, it still delivers a comparable rate capacitance of around 110 F g⁻¹.

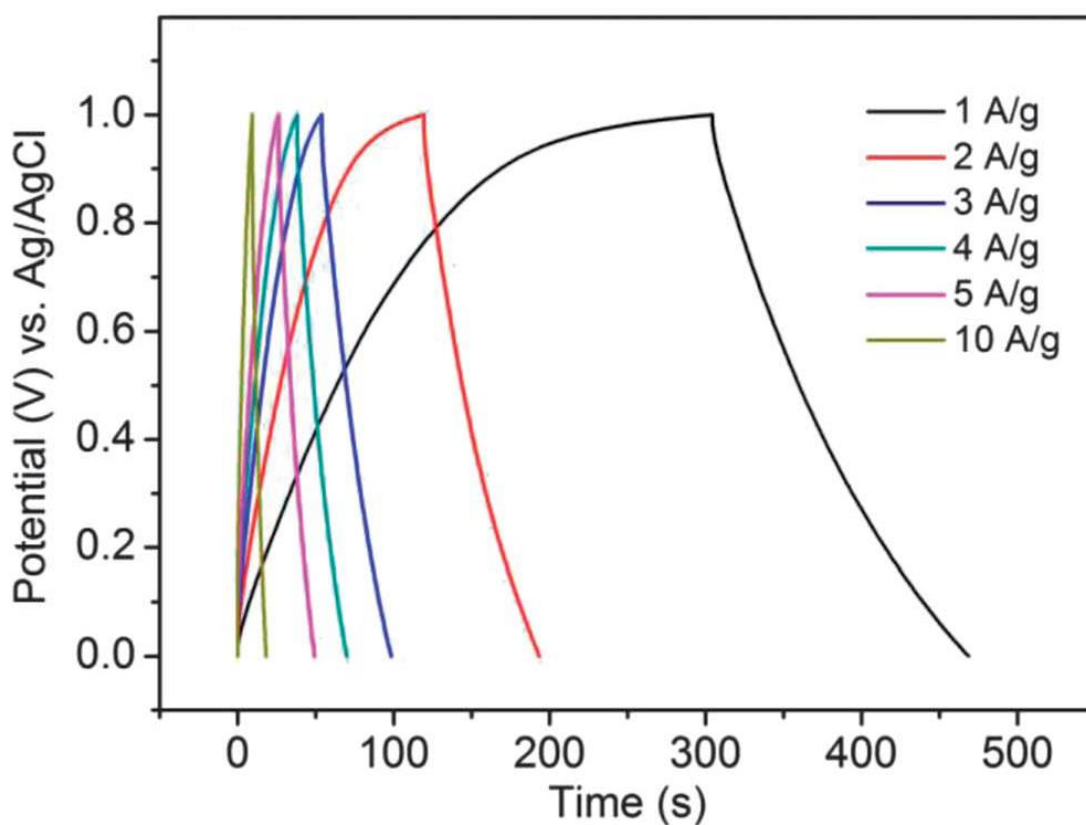


Fig. 27: Charge discharge curves of CNGMNs at different current densities [108]. Copyright 2013, The Royal Society of Chemistry.

Other types of graphene materials have also been studied as a working media for supercapacitors [109-111], such as various thermally reduced graphene oxide (rGO) [38, 110, 112]. Meanwhile, to further improve the efficacy of the working media, hydrogen gas treatment has also been proposed, increasingly adopted and proved to be an effective approach to enhance the electrochemical performance of CNT [50], TiO₂ [113], and graphene oxide based supercapacitors [114, 115]. However, surprisingly, in all the existing studies, such a treatment for graphene materials was only conducted at limited conditions, e.g., 200 °C only, and a disappointingly small specific capacitance was obtained [114, 115].

The effect of hydrogen gas treatment on the electrochemical performance of graphene materials in supercapacitors was investigated [49]. First, the cathodic deposition of graphene oxide on the surface of nickel foam through a simple custom-made EPDS device was conducted [50], and then the hydrogen gas treatment of the deposited nickel foam to produce supercapacitor electrodes was implemented as described previously [49]. The obtained hGO material was crumpled when treated at 200 to 500 °C and then returned to flat at 600 °C (See Fig. 16). During the process, the resulting graphene materials would be wrinkled or curved rather than flat, responsible for the improved electrode performance: the optimal temperature was 500 °C, leading to a reasonably high specific capacitance (110 F g⁻¹ at 10 mV s⁻¹) and outstanding cycling stability (no reduction for 2000 cycles) [49].

The cyclic voltammetry behavior of the as-prepared electrodes treated at various temperatures were examined and shown in Fig. 28a [49]. The nearly rectangular shape of the CV curves indicated a small equivalent series resistance (ESR) and a good charge transfer property within the electrodes [116, 117]. As seen from the curves, the best treatment temperature was shown to be around 500 °C, where the maximum area enclosed in the CV curve was achieved. The averaged specific capacitances at 20 mV s⁻¹ for the as-prepared electrodes were derived to be 58.5, 79.0 and 102.5 F g⁻¹ when treated at 300, 400 and 500 °C, respectively. The structural and electrochemical properties of hGO treated at 200 °C were studied previously and a small specific capacitance of 38.5 F g⁻¹ was observed [114, 115], likely because the large amount of remaining oxygen containing groups led to a low electrical conductivity.

When hGO based electrodes were treated at around 500 °C, the crumpled structure of graphene materials would keep graphene layers from densely restacking, so as to maintain a higher surface area. The near linear relationship between the specific

capacitance and treatment temperature in Fig. 28b was mainly attributed to the increase in both surface area and electrical conductivity [118], induced by the exfoliation and deoxygenation processes. However, once the treatment temperature was increased to 600 °C, a non-rectangular CV curve as shown in Fig. 28a and correspondingly, a dramatic specific capacitance loss as shown in Fig. 28b occurred, in spite of the possibility that the electrical conductivity enhancement continued at higher temperature. In other words, the likely reason for the disappointing electrochemical behaviour of the resulting electrode is that, the flat structure of the graphene material (see Fig. 16f) leads to the dense restacking of graphene layers and thus the reduced surface area, dominantly causing the performance deterioration [49].

The charge–discharge duration decreased as the current density increased from 1 to 2 and then to 3 A g⁻¹. As a result, the specific capacitances calculated from the discharge curves decreased from 96 to 86 and then to 81 F g⁻¹, respectively [49].

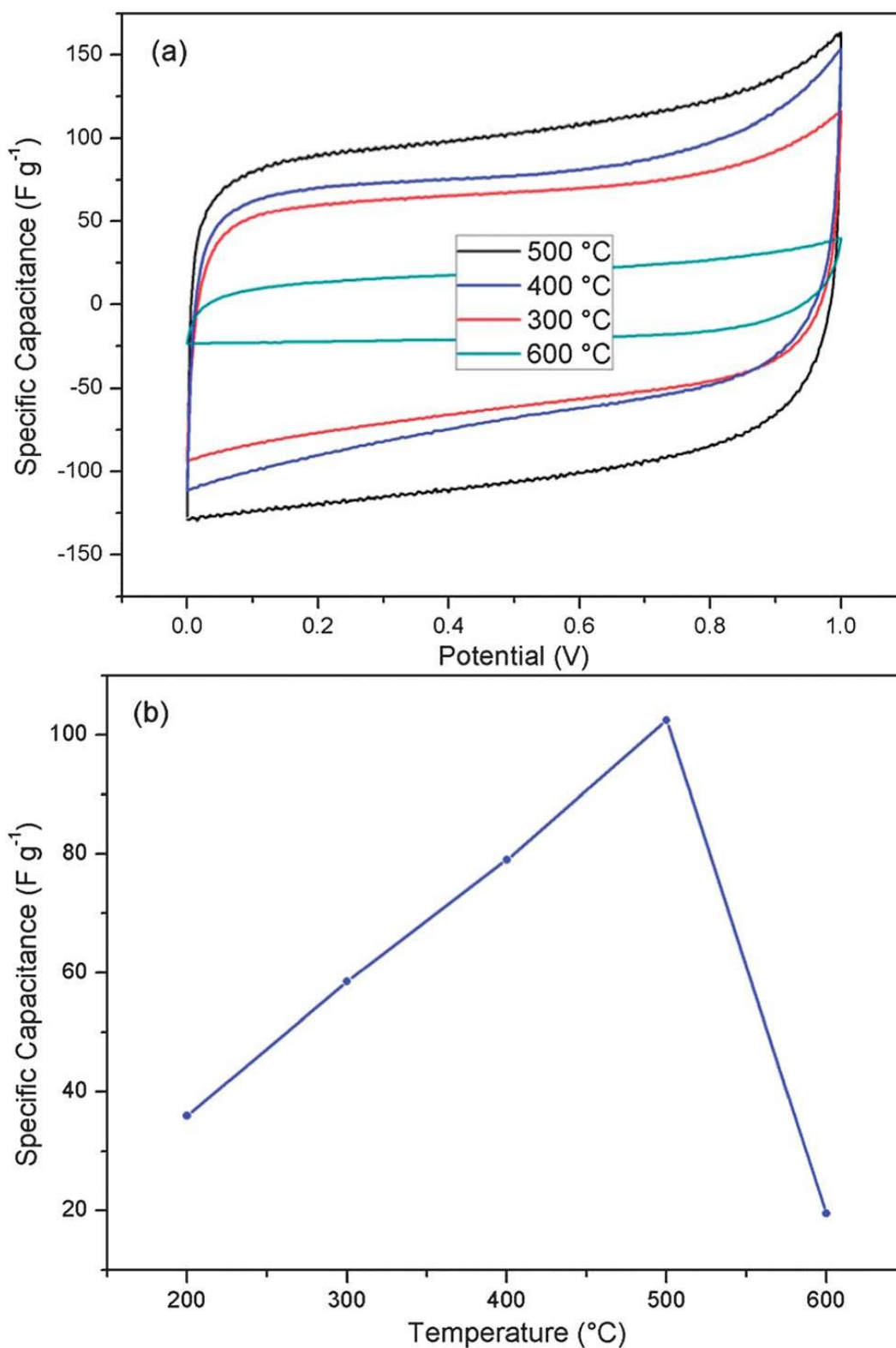
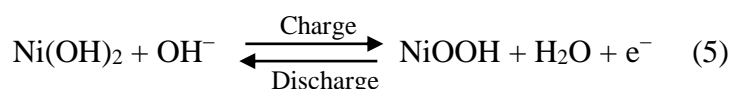


Fig. 28: Cyclic voltammograms (CVs) of hGO based electrodes treated at 300, 400, 500 and 600 °C (a), and the resulting specific capacitance at 20 mV s⁻¹ as a function of treatment temperature (b) [49]. Copyright 2013, The Royal Society of Chemistry.

It is noted that transition metal phosphide have metalloid properties, superior electrical conductivity and high theoretical capacity value (Ni_2P : ca. 1886 F g^{-1}) [119-121]. Unfortunately, the transition metal phosphide is limited by poor cyclic performance due to the structural degradation of the electrode through the redox process. An advanced approach to hybridize the electrode materials for high specific capacitance by adding electrochemical active materials Ni_2P to conductive graphene sheets (GS) matrix was used [122]. The electrochemical properties of the $\text{Ni}_2\text{P}/\text{GS}$ composite were evaluated as electrode for supercapacitors. Fig. 29a shows the typical cyclic voltammetry curves of the $\text{Ni}_2\text{P}/\text{GS}$ composites with various sweep rates ranging from 1 to 50 mV s^{-1} . The shape of the CV curves clearly reveals the pseudocapacitive characteristics. Specifically, a pair of redox peaks can be observed in all sweep rates. The electrochemical reaction mechanism is the transformation between $\text{Ni}(\text{OH})_2$ and NiOOH [121]. The anodic peak of CV curve is characteristic of the oxidation of $\text{Ni}(\text{OH})_2$ to NiOOH , and the cathodic peak corresponds to the reverse process.



The average specific capacitance of the $\text{Ni}_2\text{P}/\text{GS}$ composite electrode can be calculated from the CV curves in Fig. 29a by integrating the area under the current-potential curve according to equation 6 [122, 123].

$$C = \frac{1}{mv(V_a - V_c)} \int_{V_a}^{V_c} I(V) dV \quad (6)$$

In which \mathbf{I} (A) stands for the current, \mathbf{m} (g) is the mass of the active material in the electrode, \mathbf{v} (V s^{-1}) is the scan rate, \mathbf{V}_a and \mathbf{V}_c are the maximum and minimum voltage in the CV curve, respectively. The average specific capacitance of the $\text{Ni}_2\text{P}/\text{GS}$ composite was calculated to be 2240.8, 1248.4, 700.4, 562.9 and 390.9 F g^{-1} at the scan rates of 1, 5, 10, 20 and 50 mV s^{-1} , respectively (Table 1). However, the specific capacitance of the composite electrode decreased with the increase of the scan rates. Since the redox reactions are usually dependent on the insertion-deinsertion of protons from the electrolyte [124, 125]. At lower scan rates, the diffusion of ions from the electrolyte can enter into almost all the effective holes of the electrode. While with the increase of scan rate, the effective interaction between the ions and the electrode is

greatly reduced, which led to a lower specific capacitance. The CV curves of Ni₂P/GS composite and Ni foam were also conducted, shown in the inset in Fig. 29a. The background signal due to the Ni foam was virtually negligible, which is consistent with previous work [121, 126]. As shown in Fig. 29b, a linear relationship is observed between anodic peak current and scan rate based on the results of CV, which suggests a diffusion-limited reaction for the redox reaction of the Ni₂P/GS electrode. Fig. 29c shows the discharge curves of the Ni₂P/GS composite in a potential range of 0-0.55 V at current densities between 5 and 50 mA cm⁻². A distinct plateau region can be observed during the process, which is consistent with the CV results. The nonlinear charge/discharge profiles further verified the pseudocapacitive behavior. In the discharge curves from 0.55 to 0.3 V vs. Hg/HgO, there is a variation in the slope of the time dependence of the potential, which originates from electrochemical adsorption-desorption or a surface redox reaction on the electrode-electrolyte interface (pseudocapacitive behavior). The theoretical specific capacitance of the Ni₂P/GS composite is calculated to be 1689 F g⁻¹ based on Faraday's law. The specific capacitance is calculated by equation 7 [122, 127]:

$$C = \frac{I\Delta t}{m\Delta V} \quad (7)$$

In which **I** (A) is the discharge current, Δt (s) is the discharge time, ΔV (V) is the voltage ranged and m (g) is the mass of the active material in the electrode. Notably, the specific capacitance is as high as 1912, 1745, 1483 and 888 F g⁻¹ at the discharge current densities of 5, 10, 20 and 50 mA cm⁻², respectively. This suggests that about 46.4% of the capacitance is still retained when the charge-discharge rate is increased from 5 to 50 mA cm⁻². In addition, the cycling stability of the Ni₂P/GS electrode is also evaluated by the repeated charging-discharging measurement at a constant current density of 5 mA cm⁻², as shown in Fig. 29d. The specific capacitance increased during the first 200 cycles, which resulted from the activation process for the Ni₂P/GS electrode. After this process, the specific capacitance decreased from 1912 to 1473 F g⁻¹ after the subsequent 2300 cycles. More importantly, the Columbic efficiency was nearly 100% for each cycle of charge and discharge (inset in Fig. 29d). These results revealed the high specific capacitance and good rate capability of the Ni₂P/GS composite material for high-performance electro-chemical pseudocapacitor [122].

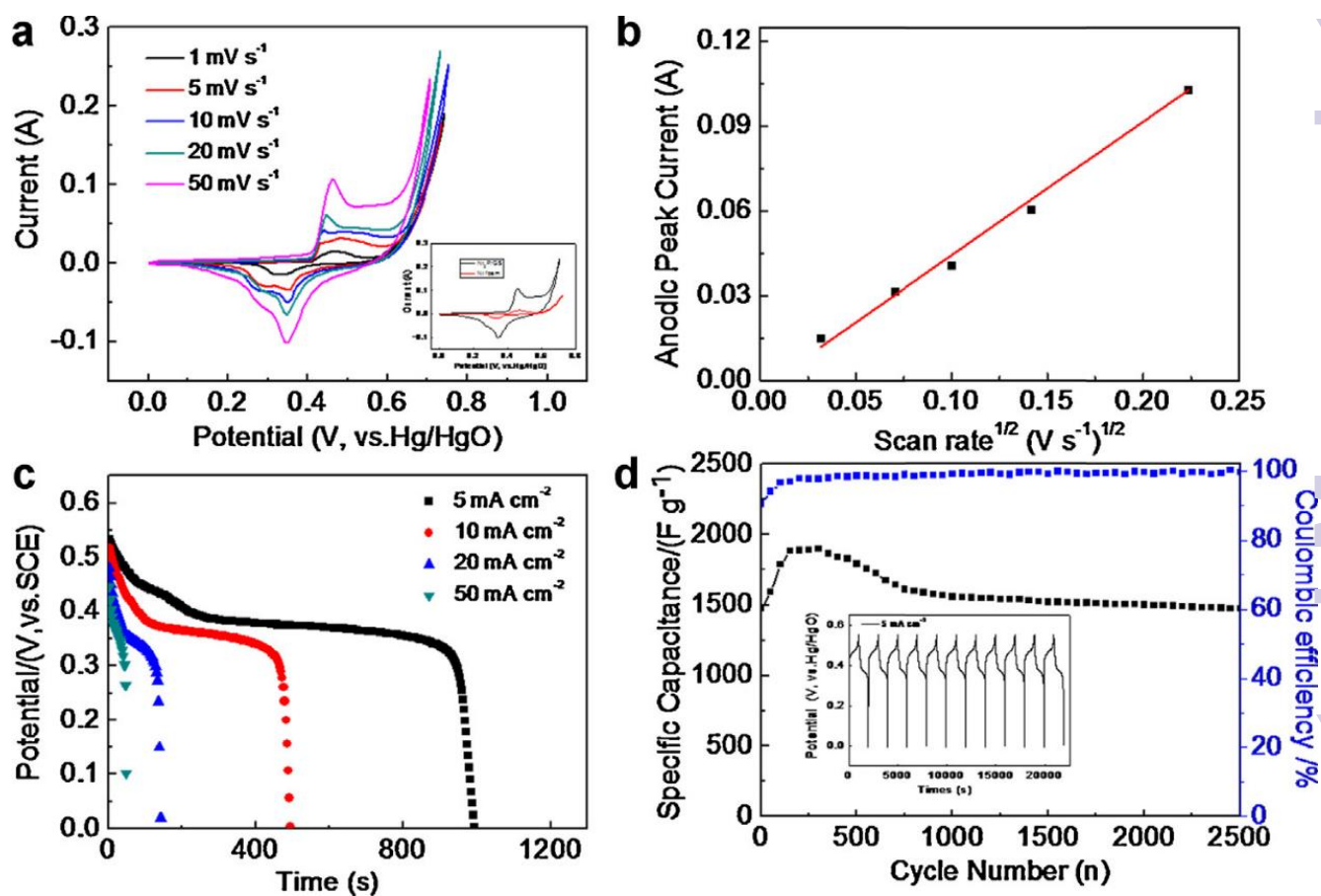


Fig. 29. Electrochemical characterizations of Ni₂P/GS composite. (a) CV curves of Ni₂P/GS electrode at various scan rates, (inset in a) CV curves of the Ni₂P/GS composite and Ni foam at the scan rate of 50 mV s⁻¹, (b) Dependence of the current on scan rate^{1/2} plot for the Ni₂P/GS electrode, (c) Galvanostatic discharge curves of Ni₂P/GS electrode at various discharge current densities, (d) Dependences of the discharge specific capacitance and the coulombic efficiency on the charge-discharge cycle numbers, galvanostatic charge and discharge curves of the Ni₂P/GS electrode at a current density of 5 mA cm⁻² (inset) [122]. Copyright 2014, Elsevier.

The electrochemical supercapacitive properties of the crumpled rGO produced by a flame-induced reduction of GO powder immersed in a flammable polar solvent such as ethanol, methanol and acetone under ordinary conditions (See Fig. 17) [51] were evaluated in a KOH aqueous electrolyte. The flammable polar solvent not only plays an important role in swelling and heating up the GO powder, but also acts as carbon sources. This new reduction method offers the advantages of simplicity, rapidity, high efficiency, energy saving, low cost and mass production of graphene. The methanol-rGO, ethanol-rGO and acetone-rGO samples (Fig. 18) have a high surface area of 421,

500 and 384 m² g⁻¹, while the specific capacitances are 260, 221 and 200 F g⁻¹ in a three-electrode setup, respectively. The good supercapacitive performances of methanol-rGO and ethanol-rGO in KOH aqueous solutions are benefited from the combination of high surface area, the residual oxygen containing groups and wrinkled morphologies. This scalable and environmentally friendly methodology will shed light for tunable surface chemistry of high quality graphene materials for potential applications in energy storage, catalysis and thermal management. The specific capacitance was calculated from the galvanostatic discharge branch. Under a specific current density of 0.1 A g⁻¹, the specific capacitances of methanol-rGO, ethanol-rGO and acetone-rGO were calculated to be 260, 224.5 and 212.6 F g⁻¹, respectively [51].

Carbon nanotube (CNT)/crumpled graphene balls (CGB) hybrid by direct growth of CNTs on the CGB surface was prepared for supercapacitor application [100]. The prepared hybrid has a unique hierarchical structure because the CGB surface is decorated with porous CNT-networks (p-CNTn) and thus has a variety of advantages for supercapacitor applications, as show in Fig. 30 [100]. The out-stretched tips of the CNTs offer multiple conducting channels to improve the charge transfer between the CGBs and between the CGBs and the current collector. In addition, the porous networks constructed by the CNTs afford easy and quick channels for mass (e.g., ion and electrolyte) transport. Moreover, the CGB structure, benefiting from its rigidity, guarantees the stability of the 3D hierachical structure [100].

CGB/Fe₃O₄ nanocrystal hybrids were produced by the previously reported one-pot ultrasonic nebulizer-based spray method [26, 97]. Fe₃O₄ nanocrystals grew from the precursor Fe³⁺ ions and deposited on both external and internal surfaces of the CGBs during the solvent evaporation and the GO crumpling process [100]. CNTs were grown on the CGB surface through a chemical vapor deposition (CVD) method with Fe as the catalyst (the product are shown in Fig 31). The typical growth process included a reduction of the CGB/Fe₃O₄ hybrids with H₂ and a CVD growth of CNTs with C₂H₂ gas as the carbon source.

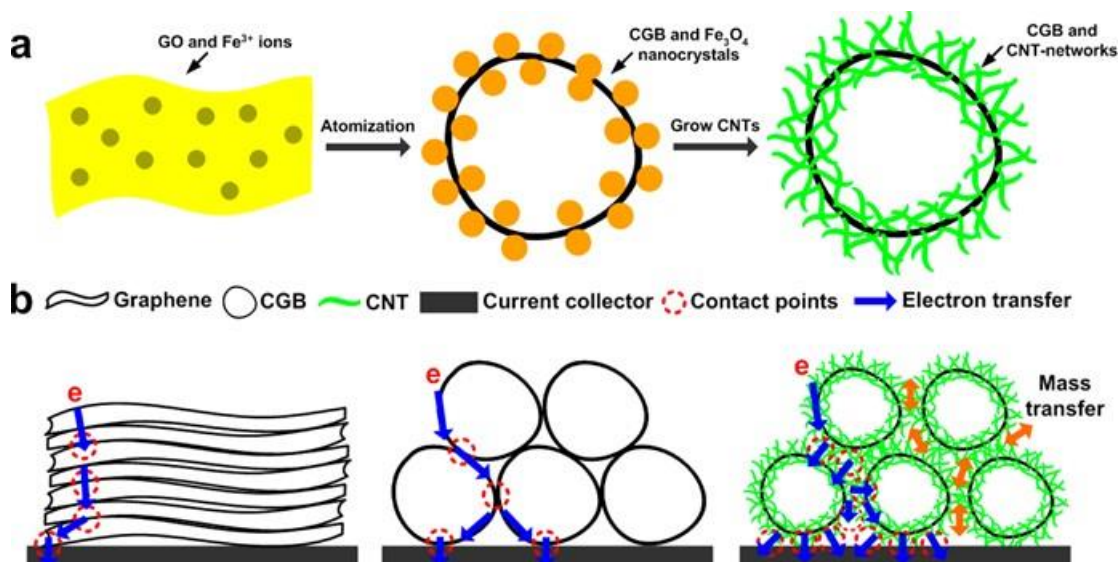


Fig. 30: (a) Schematic illustration of the p-CNTn/CGB hybrid preparation method. (b) Schematic illustrations of electron transport between the flat graphene, CGBs, and p-CNTn/CGB hybrids and current collector, respectively [100]. Copyright 2014, American Chemical Society

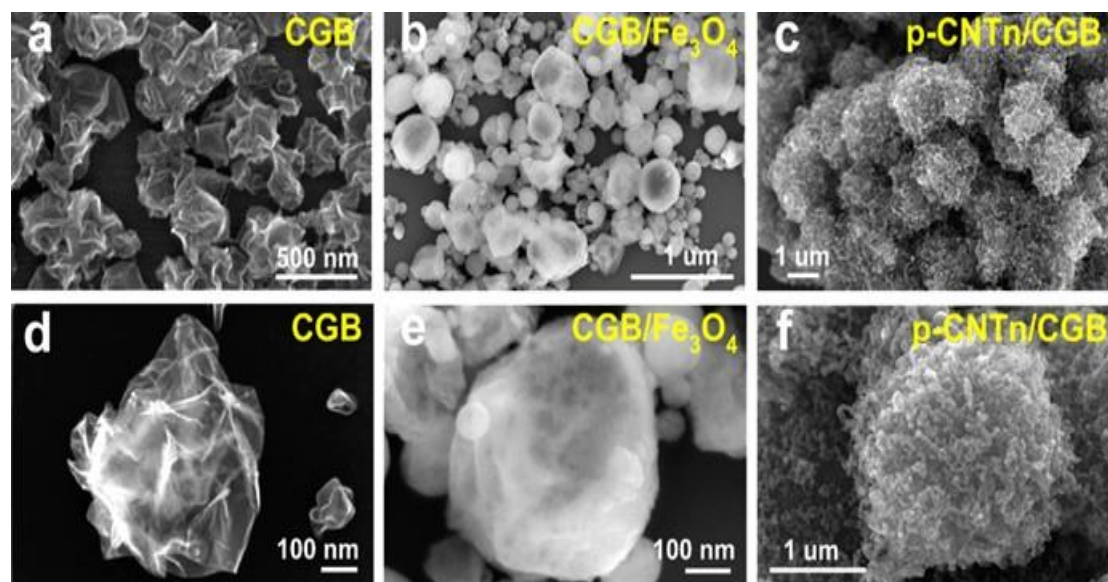


Fig. 31: SEM images of (a, d) CGBs, (b, e) CGB/ Fe_3O_4 hybrids, and (c, f) p-CNTn/CGB hybrids [100]. Copyright 2014, American Chemical Society

CNTs on the CGB surface are favorable for supercapacitors because the CNTs could work as both active materials and conducting channels to improve the contact for charge transfer between the CGBs and the current collector. As shown in Fig. 30b, for flat graphene sheets and CGBs, there are a limited number of contact spots at the contact interfaces among the active materials and between the active materials and the current collector. For these cases, electrons have to travel a long way to reach, go through, and spread into the current collector during the charge/discharge processes [128]. The considerable constriction/spreading resistance will certainly affect the capacitor performance as a result of an obstructive electron transport, especially when running at high discharge rates. In contrast, as shown in Fig. 30b, with CNT-networks bridging the active materials and the current collector, the tips and sidewalls of the CNTs could provide numerous contact spots/pathways, significantly facilitating the electron transport during charge/discharge processes. To evaluate the performance of the p-CNTn/CGB hybrids as electrode materials in a supercapacitor, Mao et al [100] assembled two-electrode symmetric coin cells with p-CNTn/CGB hybrids, RGO sheets, and CGBs as active materials, Ni foam as the current collector, and a 6 M KOH aqueous solution as the electrolyte.

The electrochemical capacitive properties of the cell were characterized by a cyclic voltammetry test. Fig. 32a-c show the CVs of p-CNTn/CGB-, CGB-, and RGO based supercapacitors at different scan rates from 10 to 1000 mV/s, respectively. For the p-CNTn/CGB cell, the CV basically maintained its rectangular shape as the scan rate increased, which is completely different from the CGB and RGO cells that show distinct distorted shapes at a high scan rate. To make a close comparison among the three cells, CVs at low scan rate (10 mV/s) and high scan rate (1000 mV/s) are shown in Fig. 32d and e, respectively. At a low scan rate, CVs from all cells have a nearly rectangular shape, indicating good capacitor characteristics (Fig. 32d). However, by carefully viewing the transition parts connecting the reverse sweeps at around 0 and 0.9 V potentials, it was found that the slopes of $\Delta I/\Delta V$ of the p-CNTn/CGB cell is larger than those of the RGO and the CGBs, which indicates better charge/discharge-rate responses of the p-CNTn/CGB cell to the applied potential [95]. This trend becomes more significant when the scan rate increases, as shown in Fig. 32e; the shapes of the CVs for RGO and CGBs are greatly distorted when the scan rate reaches 1000 mV/s. As a comparison, with an increase in scan rate, the p-CNTn/CGB cell still maintained a well rectangular shape of the CV curve. All of these results demonstrated that the p-

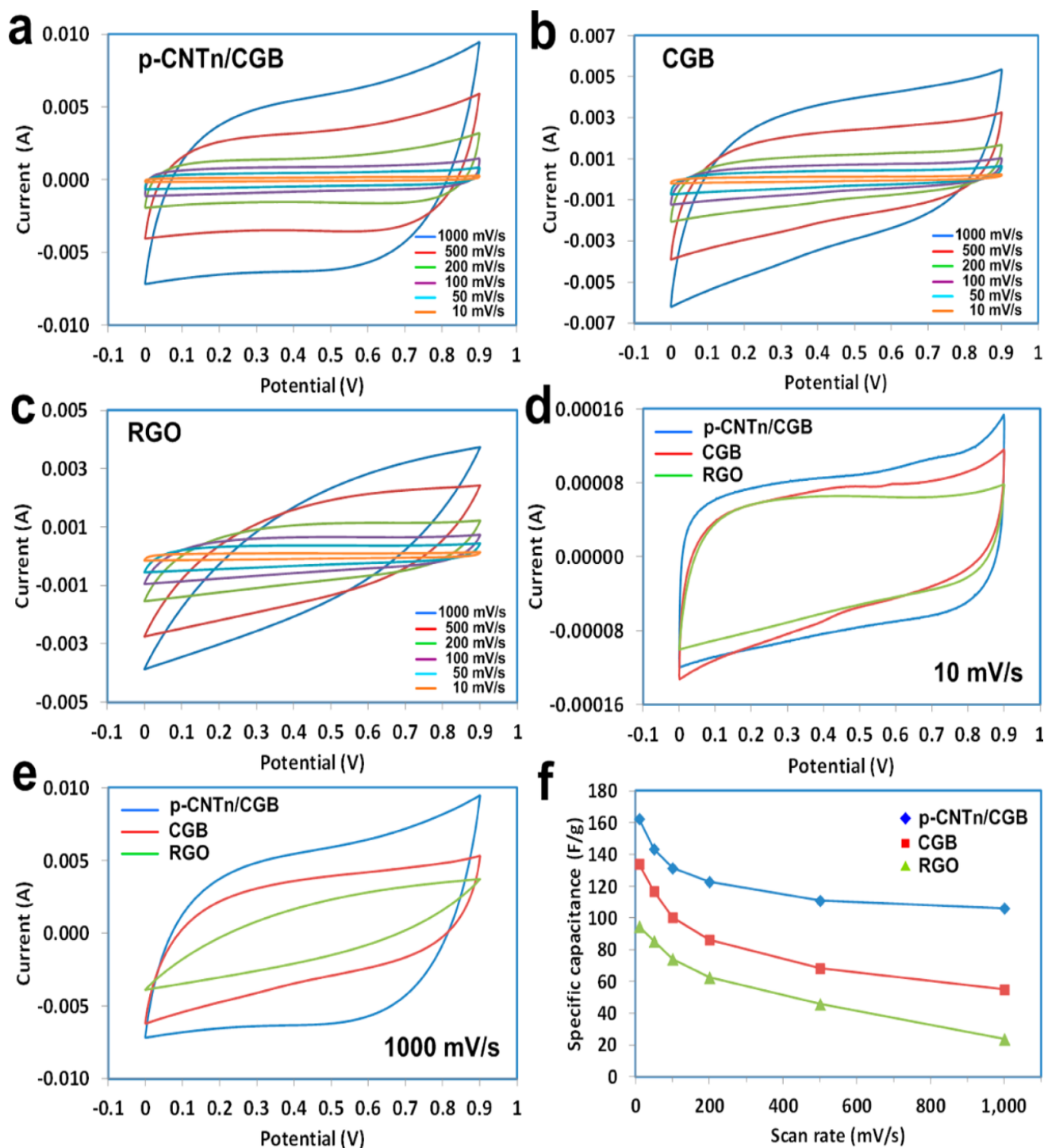


Fig. 32: Double-layer electric capacitor performance of the p-CNTn/CGB, CGB, and RGO cells with a loading of 0.13, 0.12, and 0.22 mg/cm², respectively. Electrolyte: 6 M KOH aqueous solution. (a, b, and c) CVs of the p-CNTn/CGB, CGB, and RGO cells at different scan rates from 10 to 1000 mV/s, respectively. (d) CVs of different cells at a scan rate of 10 mV/s. (e) CVs of different cells at a scan rate of 1000 mV/s. (f) The dependences of specific capacitances on potential scan rates of the p-CNTn/CGB, CGB, and RGO cells [100]. Copyright 2014, American Chemical Society.

CNTn/CGB cell possessed a better rate performance [100]. The specific capacitance of single electrode of the cells was calculated based on the scan rates and response currents in the CV curves. As shown in Fig. 32f, the p-CNTn/CGB cell shows a specific capacitance of 162.3 F/g at 10 mV/s, which decreased to 106.1 F/g (34.7% decrease) when the scan rate increased to 1000 mV/s. In contrast, the specific capacitances of the CGBs and the RGO sheets showed much larger decreases of 59.0% (from 133.9 to 54.9 F/g) and 74.9% (from 94.6 F/g to 23.8 F/g) when the scan rate increased from 10 mV/s to 1000 mV/s, respectively. The results from the CV tests have further proved that by using a porous CNT network as the conducting channel between the CGBs and the current collector, both the specific capacitance and the rate capabilities of the supercapacitor are greatly improved [100].

The specific capacitance of the p-CNTn/CGB cell calculated from galvanostatic discharge curves showed much less decrease at a high discharge current density. The specific capacitance of the p-CNTn/CGB cell decreased 52.1% from 202.0 to 96.7 F/g when the current density increased from 0.325 to 65 A/g, while the specific capacitances of the CGB and RGO cells decreased 80.9% from 176.4 to 33.7 F/g and 81.2% from 135.6 to 25.5 F/g, respectively, when the current density increased for two hundred times [100].

Highly crumpled graphene sheets (HCGSs) fabricated through freezing a chemically reduced graphene oxide aqueous suspension using liquid nitrogen [52] was used as electrode for supercapacitor. Due to their unique highly crumpled architectures (See Fig. 20 and 21) with high specific surface area and large pore volume, HCGSs exhibit high specific capacitance of 259 F g⁻¹, excellent rate capability and cycling stability (only 7% deterioration of the initial capacitance after 5000 cycles) [52]. Therefore, those intriguing electrochemical performances endow graphene material as a promising candidate electrode for high-rate supercapacitors.

Zang et al [55] reported a simple and low-cost method to fabricate extremely stretchable and high-performance electrodes for supercapacitors based on new crumpled-graphene papers (See Fig. 23). Electrolyte-mediated-graphene paper bonded on a compliant substrate can be crumpled into self-organized patterns by harnessing mechanical instabilities in the graphene paper. As the substrate is stretched, the crumpled patterns unfold, maintaining high reliability of the graphene paper under multiple cycles of large deformation. Supercapacitor electrodes based on the crumpled

graphene papers exhibit a unique combination of high stretchability (e.g., linear strain, 300%, areal strain, 800%), high electrochemical performance (specific capacitance in the range of 166-196 F g⁻¹ at a discharge rate of 1 A g⁻¹), and high reliability (e.g., over 1000 stretch/relax cycles) [55].

Active materials	Specific capacitance (F/g)	CV scan Rate (mV/s)	Specific capacitance (F/g)	Charge/ Discharge current density	Loading of active materials (mg/cm ²)	Electrolyte
Ni₂P/CGS [122]	2240.8	1				
	1248.4	5	1912	5(mAcm ⁻²)		
	700.4	10	1745	10	3	2 M KOH
	562.9	20	1483	20		
	390.9	50	888	50		
CG [49]	110	10	96	1 (A/g)		6 M KOH
	102.5	20	86	2	1.5 - 5.5	
			81	3		
N-doped CGO [38]			270	1 (A/g)		1 M H ₂ SO ₄
			230	2	1	
			182	10		
ethanol-rGO methanol-rGO acetone-rGO [51]			260, 98.9			6 M KOH
			224.5, 95.7	0.1, 20		
			212.6, 12.9	(A/g)		
CG-Mn₃O₄ [26]			1027	5 (A/g)		1.0M Na ₂ SO ₄
			404	40		
p-CNTn/CGBs [100]	162.3	10	202	0.325 (A/g)	0.13	6 M KOH
	106.1	1000	96.7	65		
Crumpled N doped porous GSs-900 [96]	248.4	5	245.9	1 (A/g)		1.0 M (Bu ₄ N)BF ₄ acetonitrile
			238.8	2	5	
			233.3	5		
			226.5	10		
Crumpled N doped porous GSs-900 [96]	302	5			5	6 M KOH
porous and highly crumpled graphene [52]	212	5	259	1 (A/g)		6 M KOH
	166	500	184	20		
Crumpled nitrogen-doped graphene-ultrafine Mn₃O₄ [108]			205.5	1 (A/g)		0.5 M Na ₂ SO ₄ solution with 5 mM NaHCO ₃
			185.6	2		
			166.6	3	7.8	
			158.2	4		
			152.3	5		
			110	10		
Stretchable crumpled-graphene papers [55]			166–196	1 (A/g)		1.0 M H ₂ SO ₄

Table 1. Supercapacitor performance of crumpled graphene-based active materials.

3.2. Crumpled graphene in Lithium-ion batteries

Lithium-ion batteries (LIBs), a lithium ion-induced device for electricity supply, have received great research interest due to increasing the needs to portable high-performance energy storage devices [129, 130]. The rapid development of various electronic devices requires LIBs with higher energy density, however, the state-of-the-art LIBs do not meet the ever-growing performance requirements for practical applications. To further improve the performance of LIBs, extended efforts have been paid to the development of advanced electrode materials, especially the anodes with high energy density, good cycling stability and better rate capability [127, 131, 132]. The main problem is the large volume change induced electrode pulverization and severe aggregation during cycling process leads to the large irreversible capacity, poor cyclability and low rate capability, which limit its application in real batteries [133]. Therefore, developing high-performance electrode material remains a long standing challenge.

Ever since transition metal oxides were first found to be suitable as anodic materials for lithium-ion batteries, a number of metal oxides with different structures have been studied extensively [134-141]. Generally, metal oxides that exhibit high theoretical capacities have poor Li^+ storage/release properties, owing to the large changes that occur in their volume during cycling and because of their low electrochemical conductivities [134-141].

Graphite is usually employed as anode material for LIBs, which can deliver a maximum theoretical lithium storage capacity of 372 mA h g^{-1} . In order to improve the performance of LIBs, researchers do great efforts to find alternative anode materials with higher capacities. Recently, graphene, a two-dimensional material with a monolayer or a few layers of carbon atoms, has been found to show higher lithium storage capacity owing to its large surface to volume ratio and highly conductive nature [142]. Furthermore, enhanced cycling performance and lithium storage capacity could also be achieved with the composites of graphene and other inorganic compounds as the anode materials [143].

Hematite ($\alpha\text{-Fe}_2\text{O}_3$), an important transition metal oxide, has attracted much attention as an anode material of LIBs due to its high specific capacity, low cost and environmental friendliness [144, 145]. However, the low electrical conductivity and

inferior cycling stability during Li^+ insertion/extraction processes restrict its practical application. It is believed that the introduction of graphene could provide highly conductive channels for electron transport and form well-defined nanopores for fast ion diffusion [146]. Meanwhile, the surrounding graphene cushions the volume expansion of the anode material upon lithium insertion. Therefore, the syntheses of graphene-based Fe_2O_3 composites for enhanced Li^+ storage have recently been reported by several groups [147-149].

Composites of Fe_2O_3 nanospindles with crumpled reduced graphene oxide (CRGO) nanosheets were prepared (See Fig. 13) using a facile solvothermal synthesis method [46]. When Fe_2O_3 -CRGO composite applied as anode material for LIBs, the composite exhibited improved electrochemical performance, compared to bare Fe_2O_3 and CRGO (Fig. 33) [46]. It showed a large initial reversible charge capacity of 1556 mA h g^{-1} at the current density of 0.1 C ($1 \text{ C} = 1000 \text{ mA g}^{-1}$), and a high reversible capacity of 969 mA h g^{-1} was retained after 100 cycles (Fig. 34). At high current rates of 1 C and 5 C , large capacities of 368 and 336 mA h g^{-1} were also obtained after 100 cycles. The performance of CRGO- Fe_2O_3 composite is also better than those of previously reported RGO- Fe_2O_3 composites at the same current density. It is suggested that the enhanced performance of the composites is attributed to the CRGO nanosheets, which not only provide a highly conductive matrix for the diffusion of electrons and lithium ions, but also limit the volume expansion of Fe_2O_3 nanospindles by surrounding them and developing nanopores as buffer spaces during the lithium insertion and extraction reactions [150, 151]. The special nanostructure is responsible for the superior performance of the composites. Comparing with flat RGO nanosheets supported composites, the crumpled RGO nanosheets could provide a more multi-dimensional confinement of Fe_2O_3 nanospindles, which cushions the effect of the volume expansion during lithium insertion. Furthermore, the nanoporous structure has more void spaces to buffer the volume change [46].

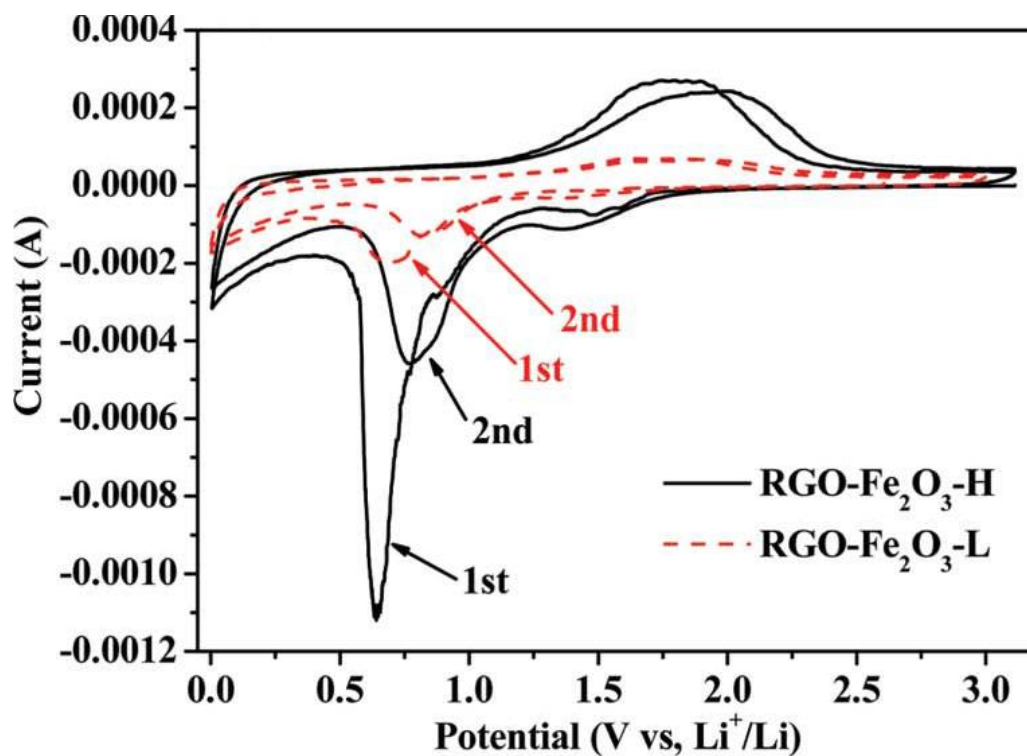


Fig. 33: Cyclic voltammetry of RGO-Fe₂O₃-H and RGO-Fe₂O₃-L composites for the first two cycles with a scan rate of 0.1 mV s⁻¹ (H and L: high and low Fe₂O₃ loadings) [46]. Copyright 2012, The Royal Society of Chemistry.

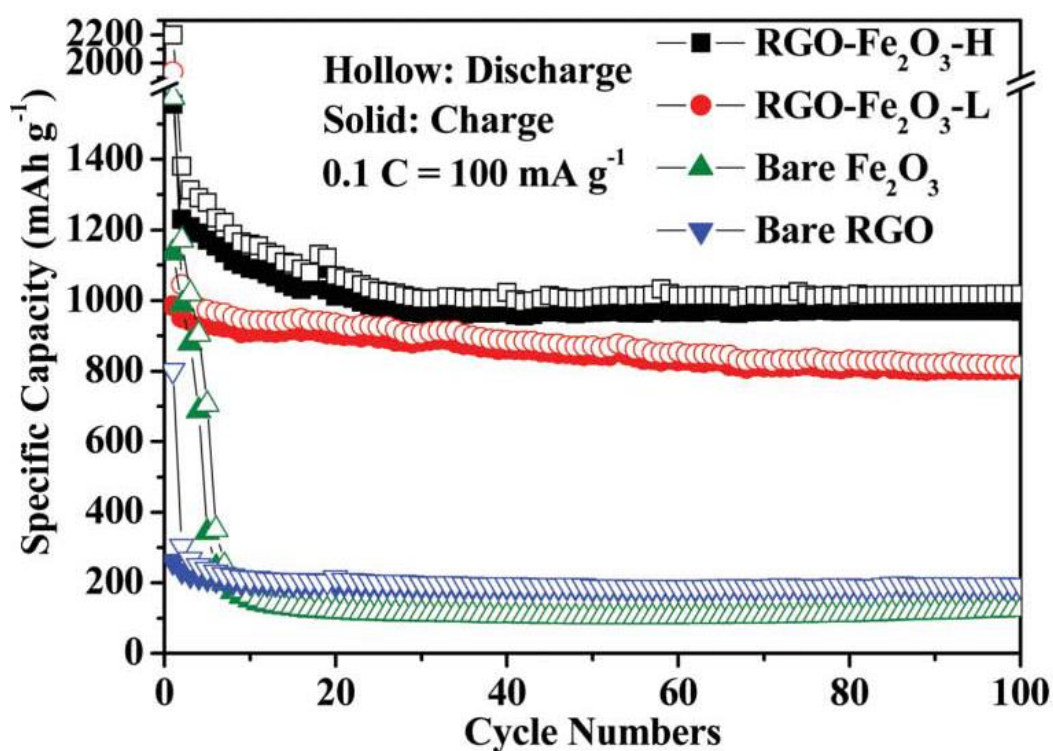


Fig. 34: The cycling performance of RGO-Fe₂O₃-H, RGO-Fe₂O₃-L, bare Fe₂O₃ nanospindles and bare RGO nanosheets at 0.1 C (H and L: high and low Fe₂O₃ loadings) [46]. Copyright 2012, The Royal Society of Chemistry.

Nanocluster Ni/NiO core-shell decorated crumpled graphene (Ni/NiO-graphene) were synthesized for using as an anodic material for lithium-ion batteries [29]. First, a crumpled graphene powder consisting of uniformly distributed Ni nanoclusters was prepared by one-pot spray pyrolysis as reported previously [17, 26-28]. This powder was subsequently transformed into the Ni/NiO-graphene composite by annealing at 300 °C in air as seen in Fig 35.

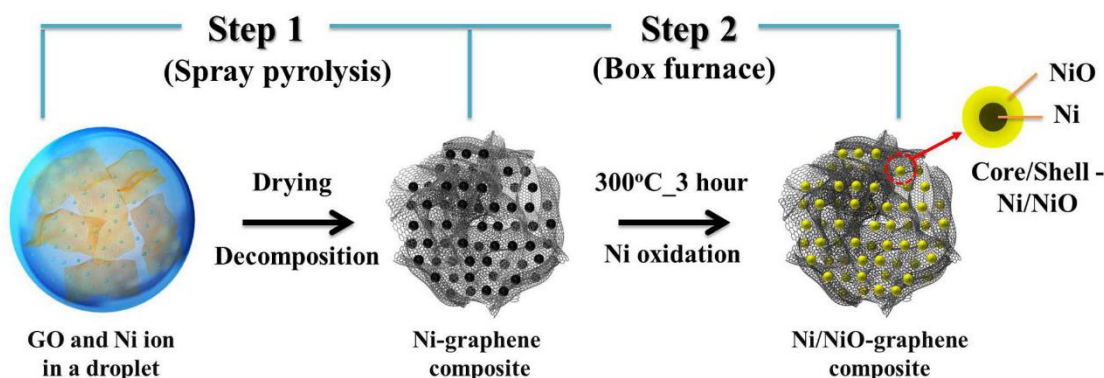


Fig 35: Formation mechanism of core-shell structured Ni/NiO nanocluster-decorated graphene (Ni/NiO-graphene) composite powder [29]. Copyright 2014, Nature publishing Group.

The electrochemical properties of the Ni/NiO-graphene composite powder were compared with those of NiO-Ni composite and pure NiO powders prepared by the same process. The Ni/NiO-graphene composite powder exhibited higher initial discharge and charge capacities and better cycling performance than those of the NiO-Ni composite and pure NiO powders [29]. The initial discharge and charge capacities of the Ni/NiO-graphene composite powder were 1156 and 845 mA h g⁻¹, respectively, and the corresponding initial coulombic efficiency was 73%. The discharge capacities of the Ni/NiO-graphene, NiO-Ni, and pure NiO powders after 300 cycles were 863, 647, and 439 mA h g⁻¹, respectively (Fig. 36) [29].

The Ni metal and graphene of the Ni/NiO-graphene composite were responsible for its superior electrochemical properties. The graphene layers retarded the destroy of the core-shell-structured Ni/NiO nanoclusters by large volume change and prevented Ni crystal growth during cycling [29].

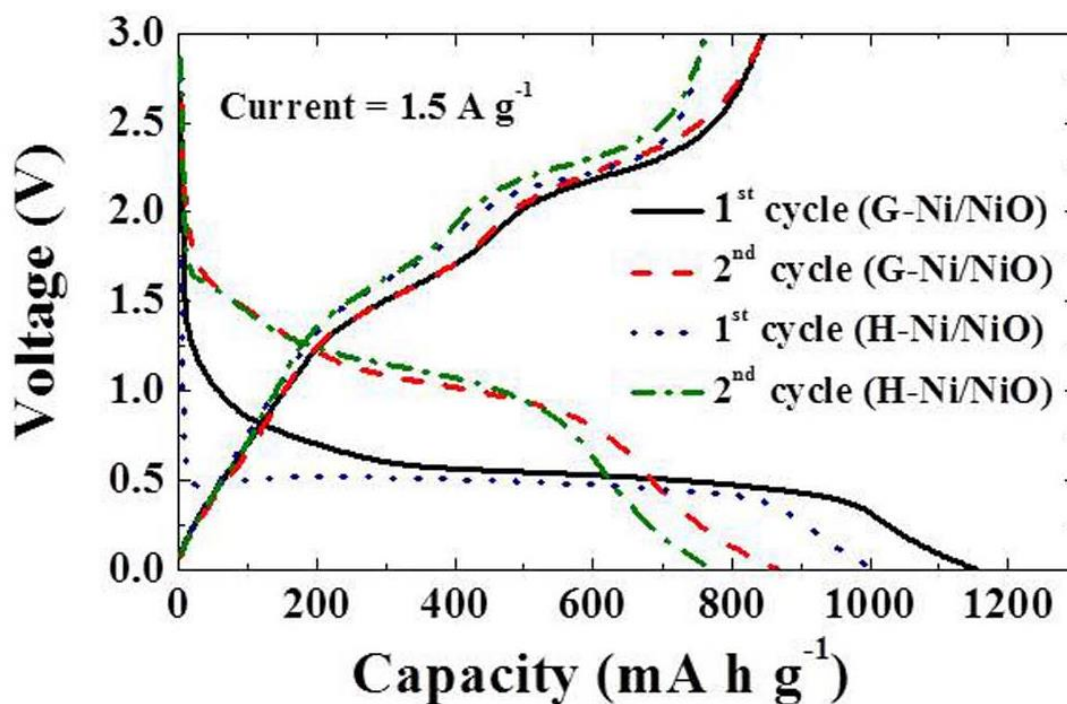


Fig. 36: First and second charge/discharge curves of the Ni/NiO-graphene and NiO-Ni [29]. Copyright 2014, Nature publishing Group.

The discharge capacities of the NiO-Ni composite powder, which had a high Ni/NiO weight ratio, increased for the first 5 cycles, and then decreased sharply for the next 70 cycles (Fig. 37). This decrease in the discharge capacity was inevitable, given the microscale structural damage that is incurred by NiO powders at high current densities, starting at the first cycle. Therefore, the increase in the discharge capacities of the NiO-Ni composite powder was due to the gradual activation of the Ni metal during the first 5 cycles. The step-by-step activation of Ni retarded the decrease in the discharge capacity of the Ni/NiO-graphene composite powder for the first several cycles. The discharge capacity of the pure NiO powder also increased slightly for the first 4 cycles (Fig. 37). In the case of the pure NiO powder, the incomplete lithiation of the thick NiO layer at a high current density of 1500 mA g^{-1} during the first discharge process increased the discharge capacity during the first 4 cycles. However, an increase in the discharge capacity was not observed in the case of the Ni/NiO graphene composite powder, owing to its low Ni content. The decrease in the discharge capacity of the Ni/NiO-graphene composite powder was lower than those in the cases of the NiO-Ni

composite and pure NiO powders during the first 70 cycles (Fig. 37). This was because of the structural stability of the Ni/NiO-graphene composite powder.

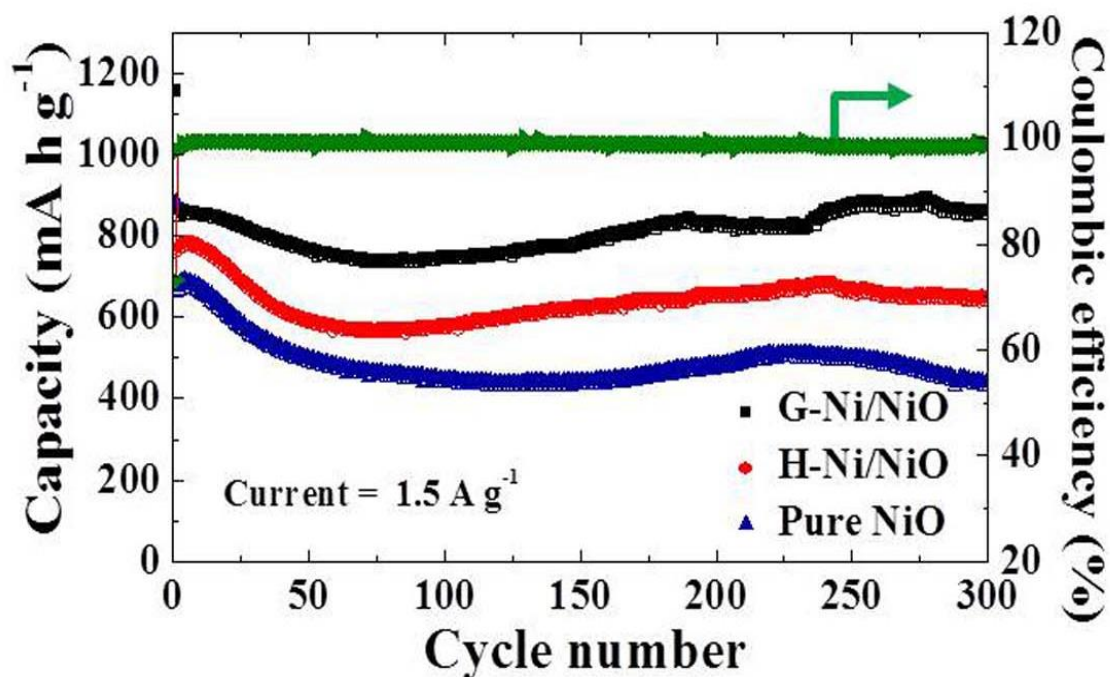


Fig. 37: Cycling performances of the Ni/NiO-graphene, hollow NiO-Ni and pure NiO at a current density of 1500 mA g^{-1} [29]. Copyright 2014, Nature publishing Group.

Silicon is a promising high-capacity anode material for Li ion batteries [152-154]. However, the large volume fluctuation upon Li^+ insertion/extraction can fracture the material [155], leading to fast capacity fading due to the loss of electrical continuity. Another problem is that cracking exposes the new surface of Si to the electrolyte solvents, which can decompose at low potential to deposit a solid electrolyte interphase (SEI) layer of lithiated compounds on the new Si surface [134, 156]. During charge/discharge cycling, the insulating SEI layer can grow thicker, which further degrades the capacity and cycling stability of the Si anode. In an operating battery cell, continuous growth of SEI layer will also gradually deplete the available Li^+ and the amount of electrolytes, thus deteriorating the overall performance.

It has been shown that various Si nanostructures [157] including nanowires [158, 159], nanotubes [160, 161], hollow spheres [162, 163], nanoparticles [164, 165], and nanoporous Si [166, 167] can withstand Li^+ insertion/removal without significant cracking or fracture. However, the formation of SEI layers on these bare Si

nanostructures (Fig. 38a) limits their Coulombic efficiency to be <99%, even after reaching steady state, which can drain the cathode and electrolyte in only tens of cycles. In comparison, the Coulombic efficiency of graphite anodes can readily reach 99.9% after the first few cycles [168]. One way to prevent the deposition of SEI on Si is to avoid its direct contact with the electrolyte solvent by applying a surface coating, which needs to be electrically conducting and permeable to Li^+ [36].

A conformal carbon coating on Si would rupture upon volume expansion, exposing Si to electrolytes for SEI deposition (Fig. 38b). Therefore, a new form of carbon coating that can accommodate the large volume expansion/contraction of Si is needed. This can be achieved by introducing void space between Si and its carbon coating. For example, Liu et al. reported a yolk-shell design of carbon-encapsulated Si (Fig. 38c) with high Coulombic efficiency up to 99.84% from cycle 500 to 1000 [169]. In their work first partially oxidize the Si nanoparticles to form a SiO_2 surface layer and then form a thin shell coating of polymer, which was later pyrolyzed to amorphous carbon. Upon HF etching to remove SiO_2 and reduce the size of the Si nanoparticles, void space was created inside the carbon hollow spheres that can accommodate volume expansion of Si during lithiation, thus preventing the rupture of the carbon shell and resulting in much improved cycling stability [169].

Submicrometer-sized capsules made of Si nanoparticles wrapped by crumpled graphene shells were made [36]. Aqueous dispersion of micrometer-sized graphene oxide (GO) sheets and Si nanoparticles were nebulized to form aerosol droplets as stated previously [26, 27], which were passed through a preheated tube furnace. Evaporation-induced capillary force wrapped graphene sheets around the Si particles, and heavily crumpled the shell. The crumpled graphene particles are remarkably stable against unfolding or collapsing due to the large number of π - π stacked folds. They are also aggregation resistant since the crumpled paper ball morphology prevents strong interparticle van der Waals attraction [36]. By adding additional components in the starting dispersion, crumpled graphene wrapped particles [32, 170] can be obtained after the aerosol synthesis, which can also be converted to hollow graphene capsules [170] after removing the particles.

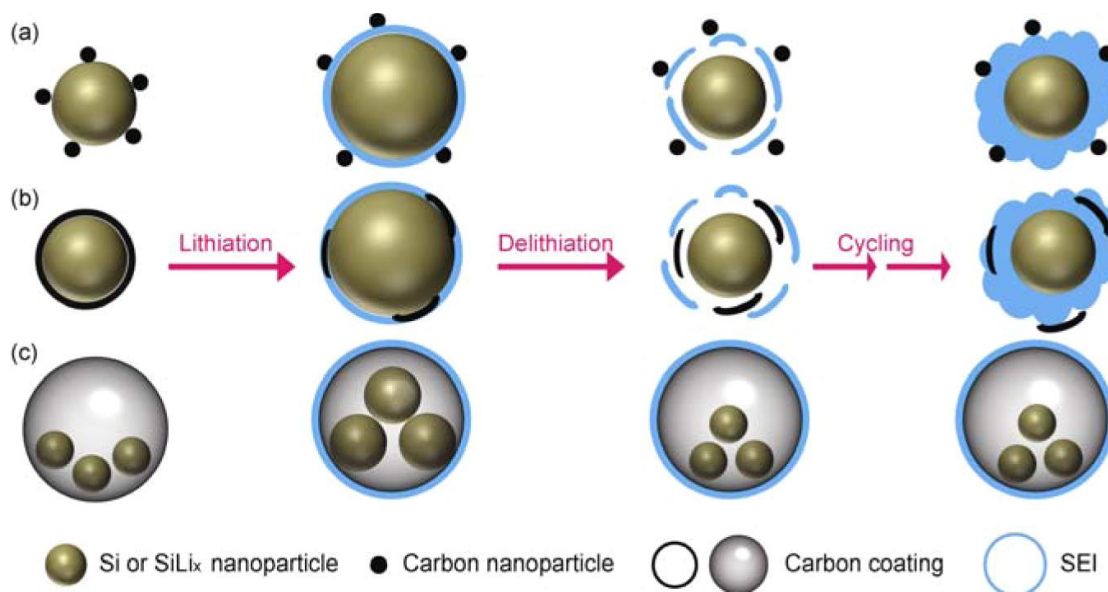


Fig. 38: Schematic drawings illustrating several types of carbon-coated Si nanoparticles during Li⁺ insertion/extraction. (a) Si decorated with carbon black binder particles. Incomplete surface coverage would lead to the deposition of insulating SEI on the Si surface, deactivating the particle. (b) Si with a continuous but conformal carbon coating. The carbon shell could rupture upon Si expansion, exposing the Si surface to SEI deposition. (c) Si in hollow carbon spheres, where the internal void space can accommodate Si volume expansion during lithiation, thus protecting the Si particles from SEI deposition [36]. Copyright 2012, American Chemical Society.

The storage capacities of the anodes made with the graphene-wrapped Si and with native Si were calculated based on the mass of the composite and the mass of bare Si nanoparticles, respectively [36]. For the crumpled graphene-encapsulated Si nanoparticles, the Coulombic efficiency for the first cycle was 73% when tested at a constant current density of 1 A/g (Fig. 39a). This was likely due to the irreversible lithium reaction with the residual functional groups in crumpled graphene and the initial SEI layer formation [36]. However, for the unprotected Si, the first-cycle efficiency was only 37%. The nearly doubled Coulombic efficiency for the first cycle suggests the effective insulation of Si from the electrolyte solvents by the crumpled graphene shell. The Coulombic efficiency of the composite capsules increased quickly, reaching 99% after 5 cycles and 99.5% after 50 cycles, which is higher than that of Si nanoparticles–graphene paper composite [171], and among the best results for nanostructured Si anode to date [158–167]. By contrast, bare Si particles exhibited only 90% Coulombic efficiency at the fifth cycle, and 95% at the 10th cycle. After the 20 cycles, the bare Si particles were severely deactivated, showing nearly 90% decrease in

capacity (Fig. 39b, green line) [36]. The low Coulombic efficiency and fast capacity fade of unprotected Si can be attributed to the loss of electrical connectivity due to the continuous growth of the SEI layer. Eventually, the growth of SEI layer would stop when the Si is completely covered, leading to gradually stabilized performance with improved Coulombic efficiency but very low capacity (Fig. 39a,b, green lines) [36]. For the composite capsules, since the crumpled shell can expand without cracking, the Si nanoparticles were effectively protected while maintaining electrical contact, leading to much higher Coulombic efficiency throughout cycling. They postulate that even if there were some pinholes on the crumpled graphene shell, they would be plugged effectively by the SEI layer that is developed there to form a protective shell around clusters of Si particles [36].

In this manner, the composite retains 83% of the charge capacity after 250 cycles. Half of the capacity loss occurred during the first 15 cycles, after which only about 0.05% of capacity loss was observed for each cycle, yielding a capacity about 940 mAh/g after 250 cycles. SEM observation (Fig. 39c) shows that the expected crumpled capsule morphology is retained [36].

Charge/discharge profiles of the composite capsules at various current densities ranging from 0.2 to 4 A/g, corresponding to an area density of around 0.05 to 1 mA/cm², are shown in Fig. 39d [36]. The composite delivered about 1200 mAh/g at a low current density of 0.2 A/g. The capacity of graphene is calculated from the second cycle of charge curve to be 338 mAh/g at 0.2A/g. Since graphene weighs 40% in the composite, considering it has reversible charge capacity, the contribution from Si particles would be around 1775 mA/g. This corresponds to a maximal lithiated state of Li_{1.85}Si. It is possible that due to the crumpled morphology, some regions of the composite may have poor electrical contact with the rest of the composite, and Si particles in these regions are not utilized [36]. Thus, the capacity of the composite capsules can be further improved if we can resolve this issue and utilize the Si nanoparticles more effectively. The highly crumpled graphene shell can accommodate the expansion/contraction of the encapsulated Si particles during charging/discharging without fracture, thus protecting the Si from SEI deposition. Encapsulation by crumpled graphene shells greatly improved the performance of the silicon as a Li ion battery anode including Coulombic efficiency, cycling stability, and rate capability [36].

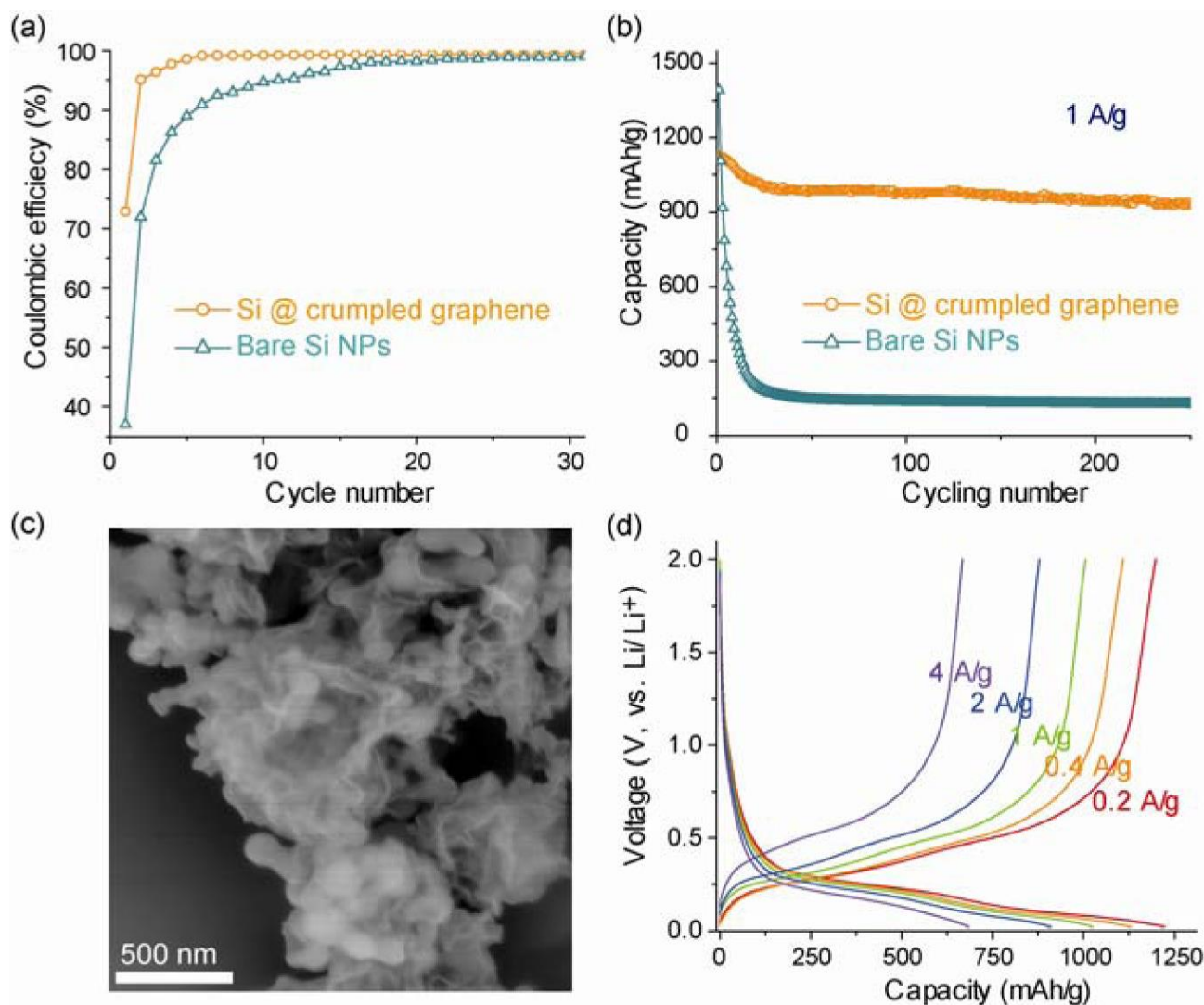


Fig. 39: Electrochemical performance of the capsules (Si@crumpled graphene). (a) Coulombic efficiency and (b) charge/discharge cycling test of the composite capsules in comparison to the unwrapped Si nanoparticles at a constant current density of 1 A/g. (c) SEM image of the capsules after 250 cycles showing that Si nanoparticles were still encapsulated in the crumpled graphene. (d) Galvanostatic charge/discharge profiles of the composite capsules electrode at various current densities ranging from 0.2 to 4 A/g [36]. Copyright 2012, American Chemical Society.

To buffer the particle pulverization that results from the inherent large volume variations (See Fig 40a), much research has focused on conductive encapsulation, mostly through carbon or conductive polymer coating [172, 173]. However, collapse of the shell and increasing of core-shell interspaces during long cycles will induce structure damage, conductivity deteriorating and further lead to the electrochemical performance fading (Fig. 40b).

To construct robust protection, Zhao et al. [174] suggested crumpled graphene as a stretchy protective shell with sustainable core-shell contact, yielding rapid strain-relaxation and sustainable electric contact simultaneously. They design CG encapsulated three dimensional (3D) electrode (Fig. 40c) through a contraction strain-driven crumpling method during liquid–solid transition of encapsulated particles [174].

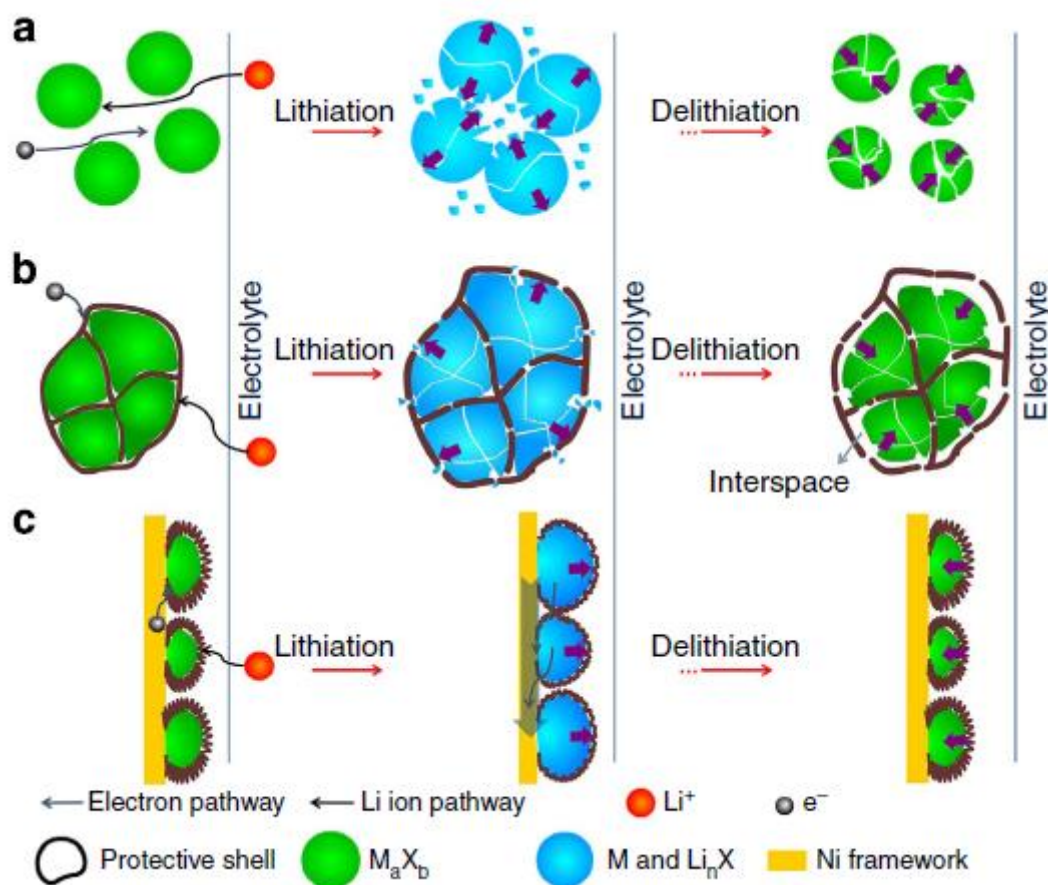


Fig. 40: Schematics of the electrochemical process in various configuration electrodes. (a) Bare particles undergo large volumetric change and tend to pulverize during cycling, resulting in poor cycling and rate performance. (b) Core–shell morphology provides a protective coating, but cracking of the shell as well as increasing of interspace between core and shell will occur on volume expansion and contraction. (c) In CG encapsulated 3D bicontinuous electrode, reversible unfolding/folding of CG buffers volume expansion and 3D configuration enhances the transport efficiency, resulting in high cycling stability and rate capability [174]. Copyright 2014, Macmillan Publishers Limited.

To evaluate the electrochemical performance and explore the influence of CG, they fabricated lithium batteries based on the $\text{Ni}_3\text{S}_2@\text{CG}/\text{Ni}$, $\text{Ni}_3\text{S}_2@0.05 \text{ CG}/\text{Ni}$ and $\text{Ni}_3\text{S}_2/\text{Ni}$ electrodes. The cycling performance of $\text{Ni}_3\text{S}_2@\text{CG}/\text{Ni}$ electrode was tested at a lower current density of 0.1 and 0.5 Ag^{-1} from 1.0 to 3.0 V for 100 charge/discharge cycles (Fig. 41a). An initial capacity of 1,036 mAhg^{-1} can be obtained and stabilized to over 900 mAhg^{-1} after 100 cycles at a current density of 0.1 Ag^{-1} , which is over five times improvement compared with the commercialized graphite ($\sim 200 \text{ mAhg}^{-1}$) [175]. When the current density increases to 0.5 Ag^{-1} , the specific capacity can reach 682 mAhg^{-1} and maintain 654 mAhg^{-1} after 100 cycles, with capacity retention up to 96%, which shows over one order of magnitude improvement compared with $\text{Ni}_3\text{S}_2/\text{Ni}$ electrode ($\sim 7\%$ capacity retention at 0.5 A g^{-1} after 100 cycles). Crumpling of graphene and newly formed interfaces of metal and lithium sulphides both enlarge the interspatial area and lead to additional capacity [174].

The capacity of $\text{Ni}_3\text{S}_2@\text{CG}/\text{Ni}$ can reach 2,165 mAhg^{-1} at a current density of 0.1 Ag^{-1} and 884 mAhg^{-1} at a current density of 8 Ag^{-1} with voltage from 0.01 to 3.0 V (Fig. 41b) [174]. Additional studies carried out at rates of 8, 10 and 20 Ag^{-1} for extended number of charge–discharge cycles (Fig. 41c) yield no capacity fading in 640, 660 and 1,000 cycles, which highlight the substantial improvement afforded by CG compared with baseline $\text{Ni}_3\text{S}_2/\text{Ni}$ electrode. The $\text{Ni}_3\text{S}_2@0.5\text{CG}/\text{Ni}$ and $\text{Ni}_3\text{S}_2/\text{Ni}$ electrodes had lower capacity, poorer cycling stability and rate performance (Fig. 41a,c) due to the lack of sufficient protection from CG [174]. This improvement is due to the fact that the crumpled structure with enhanced wettability, anisotropic adhesion can realize efficient mass transfer and further yield optimized electric double layer structure.

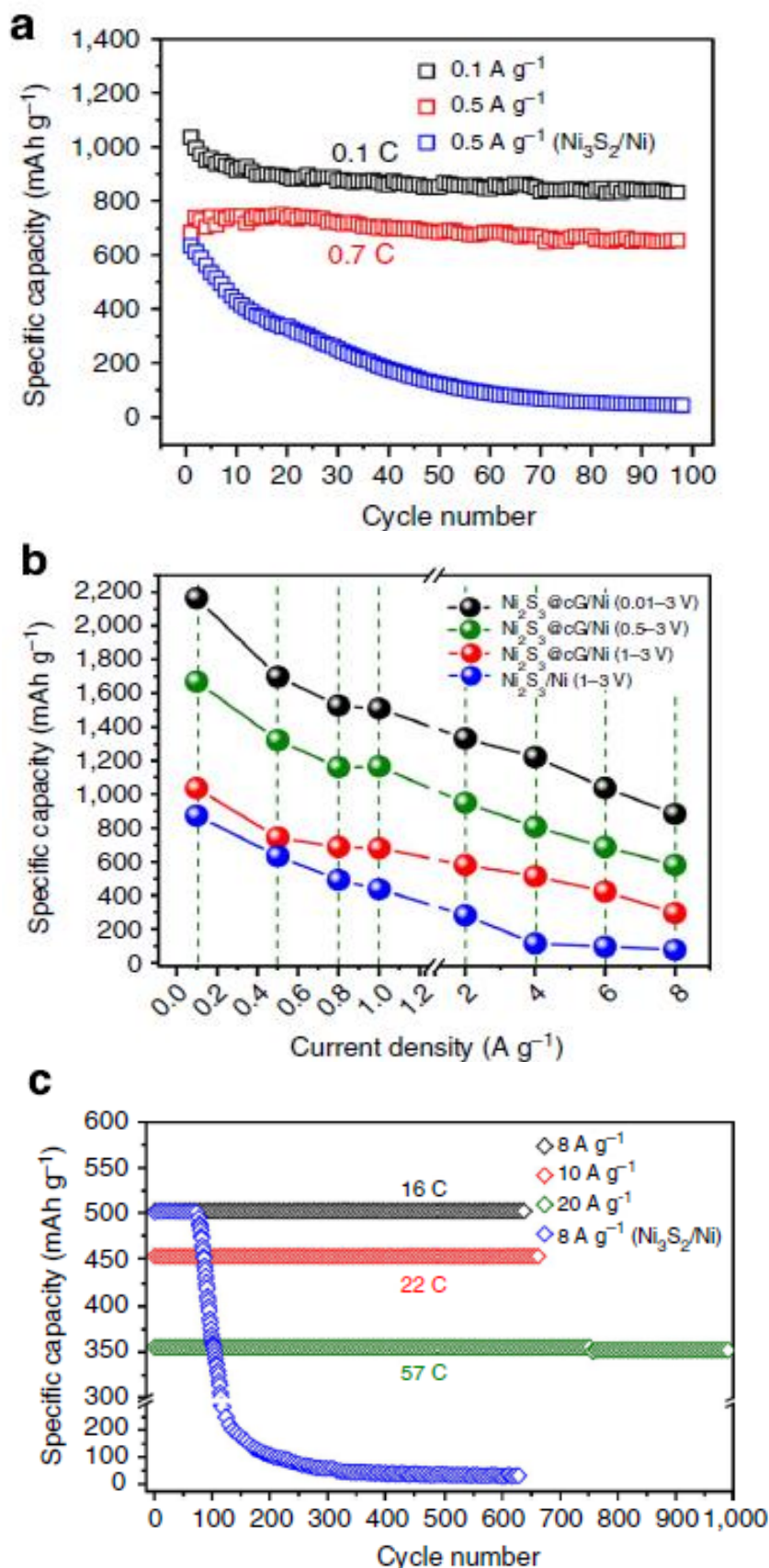


Fig. 41: (a) Cycling performance at current density of 0.1, 0.5 A g^{-1} , (b) Rate performance of $\text{Ni}_3\text{S}_2@\text{CG}/\text{Ni}$ and $\text{Ni}_3\text{S}_2/\text{Ni}$ electrode. (c) Cycling performance at current densities of 8, 10 and 20 A g^{-1} with voltage from 0.01 to 3 V [174]. Copyright 2014, Macmillan Publishers Limited.

Crumpled graphene–MoO₃ were used as anode for lithium ion batteries [28]. First, crumpled graphene–MoO₂ composite powders were prepared by means of spray pyrolysis as state previously [26, 27, 36] and from a stable graphene oxide colloidal solution in the presence of Mo ions. Second, the crumpled graphene–MoO₂ composite powders are transformed into MoO₃-based composite powders after post-treatment at 300 °C [28].

The crumpled graphene–MoO₃ powders exhibit superior electrochemical behavior compared to that of pure MoO₃ as an anode material for lithium-ion batteries. The initial discharge capacities of the graphene-MoO₃ composite and bare MoO₃ powders at a current density of 2 A/g are 1490 and 1225 mAhg⁻¹, respectively. The capacity retention of the graphene-MoO₃ composite is 87% after the first cycle, whereas that of bare MoO₃ is 47%, as measured after 100 cycles. The reversible discharge capacity of the graphene-MoO₃ composite decreases slightly from 1228 to 845 mAhg⁻¹ as the current density increases from 0.5 to 3 A/g [28].

4. Conclusion

In this review the recent progresses on the preparation and morphology of crumpled graphene were discussed. Five main methods on preparing crumpled graphene were discussed in detail, such as aerosol spray drying, hydrothermal, thermal reduction of graphene oxide, fast cooling of graphene oxide, and mechanical method. Crumpled graphene seemed to be very promising for applications in the fields where extremely large specific surface area is required such as in supercapacitor and Li ion batteries. It has unique properties such as, aggregation-resistant and rigid structure which enable it to sustain its structure easily after being immersed in an electrolyte solution. These properties endow it as a promising electrode for supercapacitors with high capacity, excellent rate capability, and long-term stability. In Li ion batteries crumpled graphene nanosheets, not only provide a highly conductive matrix for the diffusion of electrons and lithium ions, but also limit the volume expansion of the active anode materials by surrounding them and developing nanopores as buffer spaces during the lithium insertion and extraction reactions. Encapsulation of the active anode materials by crumpled graphene shells greatly improved the performance of the silicon as a Li ion battery anode including Coulombic efficiency, cycling stability, and rate capability.

Though current results have indicated that crumpled graphene is very promising for energy storage devices, however, there are still many challenges that must be addressed for these material reach their full potential. For example, the mass production of crumpled graphene. The number of layers of GO used in aerosol spray process has a great effect on the surface area of the produced crumpled graphene, because single layer graphene has the highest surface which will be maintained by crumpling, but till now, many efforts have been devoted to develop synthetic methods for graphene, while it is still difficult to obtain more than 90% even 100% single-layer graphene in mass production.

According to the discussions in this review, crumpled graphene can be obtained by different methods, but till now there no any articles about what is the differences in properties between each one and what is the advantages of each method compared to the other. Therefore, due to the crumpled graphene structure contains a lot of advantages, there is still a need to further investigation and improvement its efficiency in mass transport, electron transfer, and utilization.

References

- [1] Novoselov KS, Geim AK, Morozov S, Jiang D, Zhang Y, Dubonos S, et al. Electric field effect in atomically thin carbon films. *science*. 2004;306(5696):666-9.
- [2] Kamat PV. Graphene-based nanoarchitectures. Anchoring semiconductor and metal nanoparticles on a two-dimensional carbon support. *The Journal of Physical Chemistry Letters*. 2009;1(2):520-7.
- [3] Farghali A, Bahgat M, El Rouby W, Khedr M. Preparation, decoration and characterization of graphene sheets for methyl green adsorption. *Journal of Alloys and Compounds*. 2013;555:193-200.
- [4] Stankovich S, Dikin DA, Dommett GH, Kohlhaas KM, Zimney EJ, Stach EA, et al. Graphene-based composite materials. *Nature*. 2006;442(7100):282-6.
- [5] Rao CeNeR, Sood AeK, Subrahmanyam KeS, Govindaraj A. Graphene: The New Two-Dimensional Nanomaterial. *Angewandte Chemie International Edition*. 2009;48(42):7752-77.
- [6] Ng YH, Lightcap IV, Goodwin K, Matsumura M, Kamat PV. To what extent do graphene scaffolds improve the photovoltaic and photocatalytic response of TiO₂ nanostructured films? *The Journal of Physical Chemistry Letters*. 2010;1(15):2222-7.
- [7] Kamat PV. Graphene-based nanoassemblies for energy conversion. *The Journal of Physical Chemistry Letters*. 2011;2(3):242-51.
- [8] Dreyer DR, Park S, Bielawski CW, Ruoff RS. The chemistry of graphene oxide. *Chemical Society Reviews*. 2010;39(1):228-40.
- [9] Luo J, Jang HD, Sun T, Xiao L, He Z, Katsoulidis AP, et al. Compression and aggregation-resistant particles of crumpled soft sheets. *Acs Nano*. 2011;5(11):8943-9.
- [10] Cranford SW, Buehler MJ. Packing efficiency and accessible surface area of crumpled graphene. *Physical Review B*. 2011;84(20):205451.
- [11] Zhang L, Zhang F, Yang X, Long G, Wu Y, Zhang T, et al. Porous 3D graphene-based bulk materials with exceptional high surface area and excellent conductivity for supercapacitors. *Scientific reports*. 2013;3:1408.

- [12] Balankin AS, Ochoa DS, León EP, de Oca RCM, Rangel AH, Cruz MÁM. Power law scaling of lateral deformations with universal Poisson's index for randomly folded thin sheets. *Physical Review B*. 2008;77(12):125421.
- [13] Balankin AS, Huerta OS. Entropic rigidity of a crumpling network in a randomly folded thin sheet. *Physical Review E*. 2008;77(5):051124.
- [14] Zhao Z, Wang X, Qiu J, Lin J, Xu D, Zhang Ca, et al. Three-Dimensional Graphene-Based Hydrogel/Aerogel Materials. *Rev Adv Mater Sci*. 2014;36:137-51.
- [15] Ovid'ko I. Mechanical properties of graphene. *Reviews on Advanced Materials Science*. 2013;34:1-11.
- [16] Ovidko I. Review on grain boundaries in graphene. Curved poly-and nanocrystalline graphene structures as new carbon allotropes. *Rev Adv Mater Sci*. 2012;30:201-24.
- [17] Luo J, Jang HD, Huang J. Effect of sheet morphology on the scalability of graphene-based ultracapacitors. *ACS nano*. 2013;7(2):1464-71.
- [18] Zang J, Ryu S, Pugno N, Wang Q, Tu Q, Buehler MJ, et al. Multifunctionality and control of the crumpling and unfolding of large-area graphene. *Nature materials*. 2013;12(4):321-5.
- [19] Lobkovsky AE, Witten T. Properties of ridges in elastic membranes. *Physical Review E*. 1997;55(2):1577.
- [20] Witten T. Stress focusing in elastic sheets. *Reviews of Modern Physics*. 2007;79(2):643.
- [21] Meyer JC, Geim AK, Katsnelson M, Novoselov K, Booth T, Roth S. The structure of suspended graphene sheets. *Nature*. 2007;446(7131):60-3.
- [22] Duan WH, Gong K, Wang Q. Controlling the formation of wrinkles in a single layer graphene sheet subjected to in-plane shear. *Carbon*. 2011;49(9):3107-12.
- [23] Naumov I, Bratkovsky A. Gap opening in graphene by simple periodic inhomogeneous strain. *Physical Review B*. 2011;84(24):245444.
- [24] Miranda R, de Parga ALV. Graphene: Surfing ripples towards new devices. *Nature nanotechnology*. 2009;4(9):549-50.
- [25] Baimova J, Korznikova E, Dmitriev S, Liu B, Zhou K. Review on crumpled graphene: unique mechanical properties. *Reviews on Advanced Materials Science*. 2014;39(1).

- [26] Mao S, Wen Z, Kim H, Lu G, Hurley P, Chen J. A general approach to one-pot fabrication of crumpled graphene-based nanohybrids for energy applications. *ACS nano*. 2012;6(8):7505-13.
- [27] Ma X, Zachariah MR, Zangmeister CD. Crumpled nanopaper from graphene oxide. *Nano letters*. 2011;12(1):486-9.
- [28] Choi SH, Kang YC. Crumpled Graphene–Molybdenum Oxide Composite Powders: Preparation and Application in Lithium-Ion Batteries. *ChemSusChem*. 2014;7(2):523-8.
- [29] Choi SH, Ko YN, Lee J-K, Kang YC. Rapid continuous synthesis of spherical reduced graphene ball-nickel oxide composite for lithium ion batteries. *Scientific reports*. 2014;4.
- [30] Jian Z, Zhao L, Wang R, Hu Y-S, Li H, Chen W, et al. The low-temperature (400° C) coating of few-layer graphene on porous $\text{Li}_4\text{Ti}_5\text{O}_{12}$ via $\text{C}_{28}\text{H}_{16}\text{Br}_2$ pyrolysis for lithium-ion batteries. *RSC Adv*. 2012;2(5):1751-4.
- [31] Guo F, Creighton M, Chen Y, Hurt R, Kulaots I. Porous structures in stacked, crumpled and pillared graphene-based 3D materials. *Carbon*. 2014;66:476-84.
- [32] Chen Y, Guo F, Jachak A, Kim S-P, Datta D, Liu J, et al. Aerosol synthesis of cargo-filled graphene nanosacks. *Nano letters*. 2012;12(4):1996-2002.
- [33] Wang WN, Iskandar F, Okuyama K, Shinomiya Y. Rapid Synthesis of Non-Aggregated Fine Chloroapatite Blue Phosphor Powders with High Quantum Efficiency. *Advanced Materials*. 2008;20(18):3422-6.
- [34] Wang W-N, Kaihatsu Y, Iskandar F, Okuyama K. Highly luminous hollow chloroapatite phosphors formed by a template-free aerosol route for solid-state lighting. *Chemistry of Materials*. 2009;21(19):4685-91.
- [35] Wang W-N, Jiang Y, Biswas P. Evaporation-induced crumpling of graphene oxide nanosheets in aerosolized droplets: confinement force relationship. *The Journal of Physical Chemistry Letters*. 2012;3(21):3228-33.
- [36] Luo J, Zhao X, Wu J, Jang HD, Kung HH, Huang J. Crumpled graphene-encapsulated Si nanoparticles for lithium ion battery anodes. *The Journal of Physical Chemistry Letters*. 2012;3(13):1824-9.
- [37] Jang HD, Kim SK, Chang H, Roh K-M, Choi J-W, Huang J. A glucose biosensor based on TiO_2 –graphene composite. *Biosensors and Bioelectronics*. 2012;38(1):184-8.

- [38] Zou Y, Kinloch IA, Dryfe RA. Nitrogen-doped and crumpled graphene sheets with improved supercapacitance. *Journal of Materials Chemistry A*. 2014;2(45):19495-9.
- [39] Fasolino A, Los J, Katsnelson MI. Intrinsic ripples in graphene. *Nature materials*. 2007;6(11):858-61.
- [40] Hinds WC. *Aerosol technology: properties, behavior, and measurement of airborne particles*: John Wiley & Sons; 2012.
- [41] Zhu Y, Murali S, Cai W, Li X, Suk JW, Potts JR, et al. Graphene and graphene oxide: synthesis, properties, and applications. *Advanced materials*. 2010;22(35):3906-24.
- [42] Tallinen T, Åström J, Kekäläinen P, Timonen J. Mechanical and thermal stability of adhesive membranes with nonzero bending rigidity. *Physical review letters*. 2010;105(2):026103.
- [43] Shih C-J, Lin S, Sharma R, Strano MS, Blankschtein D. Understanding the pH-dependent behavior of graphene oxide aqueous solutions: a comparative experimental and molecular dynamics simulation study. *Langmuir*. 2011;28(1):235-41.
- [44] Li X, Zhang G, Bai X, Sun X, Wang X, Wang E, et al. Highly conducting graphene sheets and Langmuir–Blodgett films. *Nature nanotechnology*. 2008;3(9):538-42.
- [45] Hasan SA, Rigueur JL, Harl RR, Krejci AJ, Gonzalo-Juan I, Rogers BR, et al. Transferable graphene oxide films with tunable microstructures. *ACS nano*. 2010;4(12):7367-72.
- [46] Bai S, Chen S, Shen X, Zhu G, Wang G. Nanocomposites of hematite (α -Fe₂O₃) nanospindles with crumpled reduced graphene oxide nanosheets as high-performance anode material for lithium-ion batteries. *RSC Advances*. 2012;2(29):10977-84.
- [47] Hummers Jr WS, Offeman RE. Preparation of graphitic oxide. *Journal of the American Chemical Society*. 1958;80(6):1339-.
- [48] Liu S, Yu B, Zhang T. Preparation of crumpled reduced graphene oxide–poly (p-phenylenediamine) hybrids for the detection of dopamine. *Journal of Materials Chemistry A*. 2013;1(42):13314-20.

- [49] Zhang S, Pan N. Supercapacitor performance of crumpled and planar graphene materials produced by hydrogen gas reduction of graphene oxide. *Journal of Materials Chemistry A*. 2013;1(27):7957-62.
- [50] Du C, Pan N. Supercapacitors using carbon nanotubes films by electrophoretic deposition. *Journal of Power Sources*. 2006;160(2):1487-94.
- [51] Liu Y-Z, Chen C-M, Li Y-F, Li X-M, Kong Q-Q, Wang M-Z. Crumpled reduced graphene oxide by flame-induced reduction of graphite oxide for supercapacitive energy storage. *Journal of Materials Chemistry A*. 2014;2(16):5730-7.
- [52] Yan J, Xiao Y, Ning G, Wei T, Fan Z. Facile and rapid synthesis of highly crumpled graphene sheets as high-performance electrodes for supercapacitors. *RSC Advances*. 2013;3(8):2566-71.
- [53] Yang X, Cheng C, Wang Y, Qiu L, Li D. Liquid-mediated dense integration of graphene materials for compact capacitive energy storage. *Science*. 2013;341(6145):534-7.
- [54] Dikin DA, Stankovich S, Zimney EJ, Piner RD, Dommett GH, Evmenenko G, et al. Preparation and characterization of graphene oxide paper. *Nature*. 2007;448(7152):457-60.
- [55] Zang J, Cao C, Feng Y, Liu J, Zhao X. Stretchable and High-Performance Supercapacitors with Crumpled Graphene Papers. *Scientific reports*. 2014;4.
- [56] Ramanathan T, Abdala A, Stankovich S, Dikin D, Herrera-Alonso M, Piner R, et al. Functionalized graphene sheets for polymer nanocomposites. *Nature nanotechnology*. 2008;3(6):327-31.
- [57] Pereira VM, Neto AC, Liang H, Mahadevan L. Geometry, mechanics, and electronics of singular structures and wrinkles in graphene. *Physical review letters*. 2010;105(15):156603.
- [58] Levy N, Burke S, Meaker K, Panlasigui M, Zettl A, Guinea F, et al. Strain-induced pseudo-magnetic fields greater than 300 tesla in graphene nanobubbles. *Science*. 2010;329(5991):544-7.
- [59] Guinea F, Katsnelson M, Geim A. Energy gaps and a zero-field quantum Hall effect in graphene by strain engineering. *Nature Physics*. 2010;6(1):30-3.
- [60] Kim KS, Zhao Y, Jang H, Lee SY, Kim JM, Kim KS, et al. Large-scale pattern growth of graphene films for stretchable transparent electrodes. *Nature*. 2009;457(7230):706-10.

- [61] Bao W, Miao F, Chen Z, Zhang H, Jang W, Dames C, et al. Controlled ripple texturing of suspended graphene and ultrathin graphite membranes. *Nature nanotechnology*. 2009;4(9):562-6.
- [62] Scharfenberg S, Rocklin D, Chialvo C, Weaver RL, Goldbart PM, Mason N. Probing the mechanical properties of graphene using a corrugated elastic substrate. *Applied Physics Letters*. 2011;98(9):091908.
- [63] Li T, Zhang Z. Substrate-regulated morphology of graphene. *Journal of Physics D: Applied Physics*. 2010;43(7):075303.
- [64] Cao Y, Hutchinson JW. Wrinkling phenomena in neo-Hookean film/substrate bilayers. *Journal of applied Mechanics*. 2012;79(3):031019.
- [65] Wang Y, Yang R, Shi Z, Zhang L, Shi D, Wang E, et al. Super-elastic graphene ripples for flexible strain sensors. *ACS nano*. 2011;5(5):3645-50.
- [66] Lee C, Wei X, Kysar JW, Hone J. Measurement of the elastic properties and intrinsic strength of monolayer graphene. *science*. 2008;321(5887):385-8.
- [67] Mei H, Landis CM, Huang R. Concomitant wrinkling and buckle-delamination of elastic thin films on compliant substrates. *Mechanics of Materials*. 2011;43(11):627-42.
- [68] Hutchinson JW, Suo Z. Mixed mode cracking in layered materials. *Advances in applied mechanics*. 1992;29(63):191.
- [69] Vella D, Bico J, Boudaoud A, Roman B, Reis PM. The macroscopic delamination of thin films from elastic substrates. *Proceedings of the National Academy of Sciences*. 2009;106(27):10901-6.
- [70] Rogers JA, Someya T, Huang Y. Materials and mechanics for stretchable electronics. *Science*. 2010;327(5973):1603-7.
- [71] Kaltenbrunner M, White MS, Głowacki ED, Sekitani T, Someya T, Sariciftci NS, et al. Ultrathin and lightweight organic solar cells with high flexibility. *Nature communications*. 2012;3:770.
- [72] Kim P, Abkarian M, Stone HA. Hierarchical folding of elastic membranes under biaxial compressive stress. *Nature materials*. 2011;10(12):952-7.
- [73] Booth TJ, Blake P, Nair RR, Jiang D, Hill EW, Bangert U, et al. Macroscopic graphene membranes and their extraordinary stiffness. *Nano letters*. 2008;8(8):2442-6.
- [74] Avouris P, Chen Z, Perebeinos V. Carbon-based electronics. *Nature nanotechnology*. 2007;2(10):605-15.

- [75] Novoselov KS, Geim AK, Morozov S, Jiang D, Zhang Y, Dubonos Sa, et al. Electric field effect in atomically thin carbon films. *science*. 2004;306(5696):666-9.
- [76] Balandin AA, Ghosh S, Bao W, Calizo I, Teweldebrhan D, Miao F, et al. Superior thermal conductivity of single-layer graphene. *Nano letters*. 2008;8(3):902-7.
- [77] Xia J, Chen F, Li J, Tao N. Measurement of the quantum capacitance of graphene. *Nature nanotechnology*. 2009;4(8):505-9.
- [78] Liang J, Huang Y, Zhang L, Wang Y, Ma Y, Guo T, et al. Molecular-level dispersion of graphene into poly (vinyl alcohol) and effective reinforcement of their nanocomposites. *Advanced Functional Materials*. 2009;19(14):2297-302.
- [79] Becerril HA, Mao J, Liu Z, Stoltenberg RM, Bao Z, Chen Y. Evaluation of solution-processed reduced graphene oxide films as transparent conductors. *ACS nano*. 2008;2(3):463-70.
- [80] Schedin F, Geim A, Morozov S, Hill E, Blake P, Katsnelson M, et al. Detection of individual gas molecules adsorbed on graphene. *Nature materials*. 2007;6(9):652-5.
- [81] He Q, Sudibya HG, Yin Z, Wu S, Li H, Boey F, et al. Centimeter-long and large-scale micropatterns of reduced graphene oxide films: fabrication and sensing applications. *Acs Nano*. 2010;4(6):3201-8.
- [82] Liang J, Xu Y, Huang Y, Zhang L, Wang Y, Ma Y, et al. Infrared-triggered actuators from graphene-based nanocomposites. *The Journal of Physical Chemistry C*. 2009;113(22):9921-7.
- [83] Xie X, Qu L, Zhou C, Li Y, Zhu J, Bai H, et al. An asymmetrically surface-modified graphene film electrochemical actuator. *ACS nano*. 2010;4(10):6050-4.
- [84] Liang J, Huang Y, Oh J, Kozlov M, Sui D, Fang S, et al. Electromechanical actuators based on graphene and graphene/Fe₃O₄ hybrid paper. *Advanced Functional Materials*. 2011;21(19):3778-84.
- [85] Das A, Pisana S, Chakraborty B, Piscanec S, Saha S, Waghmare U, et al. Monitoring dopants by Raman scattering in an electrochemically top-gated graphene transistor. *Nature nanotechnology*. 2008;3(4):210-5.
- [86] Li B, Cao X, Ong HG, Cheah JW, Zhou X, Yin Z, et al. All-Carbon Electronic Devices Fabricated by Directly Grown Single-Walled Carbon Nanotubes on

- Reduced Graphene Oxide Electrodes. *Advanced Materials*. 2010;22(28):3058-61.
- [87] Brownson DA, Kampouris DK, Banks CE. An overview of graphene in energy production and storage applications. *Journal of Power Sources*. 2011;196(11):4873-85.
- [88] Pumera M. Graphene-based nanomaterials and their electrochemistry. *Chemical Society Reviews*. 2010;39(11):4146-57.
- [89] Sun Y, Wu Q, Shi G. Graphene based new energy materials. *Energy & Environmental Science*. 2011;4(4):1113-32.
- [90] Eda G, Chhowalla M. Chemically derived graphene oxide: towards large-area thin-film electronics and optoelectronics. *Advanced Materials*. 2010;22(22):2392-415.
- [91] Allen MJ, Tung VC, Kaner RB. Honeycomb carbon: a review of graphene. *Chemical reviews*. 2009;110(1):132-45.
- [92] Huang X, Qi X, Boey F, Zhang H. Graphene-based composites. *Chemical Society Reviews*. 2012;41(2):666-86.
- [93] Yu D, Dai L. Self-assembled graphene/carbon nanotube hybrid films for supercapacitors. *The Journal of Physical Chemistry Letters*. 2009;1(2):467-70.
- [94] Hao L, Li X, Zhi L. Carbonaceous electrode materials for supercapacitors. *Advanced Materials*. 2013;25(28):3899-904.
- [95] Conway B. *Electrochemical supercapacitor. Scientific Fundamentals and Technological Applications*. New York: Kluwer Academic/Plenum Publishers 1999.
- [96] Wen Z, Wang X, Mao S, Bo Z, Kim H, Cui S, et al. Crumpled Nitrogen-Doped Graphene Nanosheets with Ultrahigh Pore Volume for High-Performance Supercapacitor. *Advanced Materials*. 2012;24(41):5610-6.
- [97] Mao S, Wen Z, Huang T, Hou Y, Chen J. High-performance bi-functional electrocatalysts of 3D crumpled graphene–cobalt oxide nanohybrids for oxygen reduction and evolution reactions. *Energy & Environmental Science*. 2014;7(2):609-16.
- [98] Ruoff R. Perspective: A means to an end. *Nature*. 2012;483(7389):S42-S.

- [99] Ma X, Zachariah MR, Zangmeister CD. Reduction of suspended graphene oxide single sheet nanopaper: the effect of crumpling. *The Journal of Physical Chemistry C*. 2013;117(6):3185-91.
- [100] Mao BS, Wen Z, Bo Z, Chang J, Huang X, Chen J. Hierarchical Nanohybrids with Porous CNT-Networks Decorated Crumpled Graphene Balls for Supercapacitors. *ACS applied materials & interfaces*. 2014;6(12):9881-9.
- [101] Wang Y, Shi Z, Huang Y, Ma Y, Wang C, Chen M, et al. Supercapacitor devices based on graphene materials. *The Journal of Physical Chemistry C*. 2009;113(30):13103-7.
- [102] Tang W, Peng L, Yuan C, Wang J, Mo S, Zhao C, et al. Facile synthesis of 3D reduced graphene oxide and its polyaniline composite for super capacitor application. *Synthetic Metals*. 2015;202:140-6.
- [103] Li Y, Cao D, Wang Y, Yang S, Zhang D, Ye K, et al. Hydrothermal deposition of manganese dioxide nanosheets on electrodeposited graphene covered nickel foam as a high-performance electrode for supercapacitors. *Journal of Power Sources*. 2015;279:138-45.
- [104] Feng X, Chen N, Zhang Y, Yan Z, Liu X, Ma Y, et al. The self-assembly of shape controlled functionalized graphene–MnO₂ composites for application as supercapacitors. *Journal of Materials Chemistry A*. 2014;2(24):9178-84.
- [105] Mahmood N, Zhang C, Yin H, Hou Y. Graphene-based nanocomposites for energy storage and conversion in lithium batteries, supercapacitors and fuel cells. *Journal of Materials Chemistry A*. 2014;2(1):15-32.
- [106] Liu J, Poh CK, Zhan D, Lai L, Lim SH, Wang L, et al. Improved synthesis of graphene flakes from the multiple electrochemical exfoliation of graphite rod. *Nano Energy*. 2013;2(3):377-86.
- [107] Park S, Ruoff RS. Chemical methods for the production of graphenes. *Nature nanotechnology*. 2009;4(4):217-24.
- [108] Yang S, Song X, Zhang P, Gao L. Crumpled nitrogen-doped graphene–ultrafine Mn₃O₄ nanohybrids and their application in supercapacitors. *Journal of Materials Chemistry A*. 2013;1(45):14162-9.
- [109] Jeong HM, Lee JW, Shin WH, Choi YJ, Shin HJ, Kang JK, et al. Nitrogen-doped graphene for high-performance ultracapacitors and the importance of nitrogen-doped sites at basal planes. *Nano letters*. 2011;11(6):2472-7.

- [110] Zhao B, Liu P, Jiang Y, Pan D, Tao H, Song J, et al. Supercapacitor performances of thermally reduced graphene oxide. *Journal of power sources*. 2012;198:423-7.
- [111] Kim TY, Lee HW, Stoller M, Dreyer DR, Bielawski CW, Ruoff RS, et al. High-performance supercapacitors based on poly (ionic liquid)-modified graphene electrodes. *ACS nano*. 2010;5(1):436-42.
- [112] Zhu Y, Stoller MD, Cai W, Velamakanni A, Piner RD, Chen D, et al. Exfoliation of graphite oxide in propylene carbonate and thermal reduction of the resulting graphene oxide platelets. *Acs Nano*. 2010;4(2):1227-33.
- [113] Lu X, Wang G, Zhai T, Yu M, Gan J, Tong Y, et al. Hydrogenated TiO₂ nanotube arrays for supercapacitors. *Nano letters*. 2012;12(3):1690-6.
- [114] Mishra AK, Ramaprabhu S. Functionalized graphene-based nanocomposites for supercapacitor application. *The Journal of Physical Chemistry C*. 2011;115(29):14006-13.
- [115] Kaniyoor A, Baby TT, Ramaprabhu S. Graphene synthesis via hydrogen induced low temperature exfoliation of graphite oxide. *Journal of Materials Chemistry*. 2010;20(39):8467-9.
- [116] Zhang S, Li Y, Pan N. Graphene based supercapacitor fabricated by vacuum filtration deposition. *Journal of Power sources*. 2012;206:476-82.
- [117] Stoller MD, Park S, Zhu Y, An J, Ruoff RS. Graphene-based ultracapacitors. *Nano letters*. 2008;8(10):3498-502.
- [118] Li X, Wang H, Robinson JT, Sanchez H, Diankov G, Dai H. Simultaneous nitrogen doping and reduction of graphene oxide. *Journal of the American Chemical Society*. 2009;131(43):15939-44.
- [119] Aso K, Hayashi A, Tatsumisago M. Phase-Selective Synthesis of Nickel Phosphide in High-Boiling Solvent for All-Solid-State Lithium Secondary Batteries. *Inorganic chemistry*. 2011;50(21):10820-4.
- [120] Dou Y, Li G, Song J, Gao X. Nickel phosphide-embedded graphene as counter electrode for dye-sensitized solar cells. *Phys Chem Chem Phys*. 2012;14(4):1339-42.
- [121] An C, Wang Y, Wang Y, Liu G, Li L, Qiu F, et al. Facile synthesis and superior supercapacitor performances of Ni₂P/rGO nanoparticles. *RSC Advances*. 2013;3(14):4628-33.

- [122] An C, Wang Y, Li L, Qiu F, Xu Y, Xu C, et al. Effects of highly crumpled graphene nanosheets on the electrochemical performances of pseudocapacitor electrode materials. *Electrochimica Acta*. 2014;133:180-7.
- [123] Simon P, Gogotsi Y. Materials for electrochemical capacitors. *Nature materials*. 2008;7(11):845-54.
- [124] Subramanian V, Zhu H, Vajtai R, Ajayan P, Wei B. Hydrothermal synthesis and pseudocapacitance properties of MnO₂ nanostructures. *The Journal of Physical Chemistry B*. 2005;109(43):20207-14.
- [125] Xu M-W, Zhao D-D, Bao S-J, Li H-L. Mesoporous amorphous MnO₂ as electrode material for supercapacitor. *Journal of Solid State Electrochemistry*. 2007;11(8):1101-7.
- [126] An C, Wang Y, Huang Y, Xu Y, Xu C, Jiao L, et al. Novel three-dimensional NiCo₂O₄ architectures: solvothermal synthesis and electrochemical properties. *CrystEngComm*. 2014;16(3):385-92.
- [127] Liu C, Li F, Ma LP, Cheng HM. Advanced materials for energy storage. *Advanced Materials*. 2010;22(8):E28-E62.
- [128] Bo Z, Zhu W, Ma W, Wen Z, Shuai X, Chen J, et al. Vertically Oriented Graphene Bridging Active-Layer/Current-Collector Interface for Ultrahigh Rate Supercapacitors. *Advanced Materials*. 2013;25(40):5799-806.
- [129] Wakihara M. Recent developments in lithium ion batteries. *Materials Science and Engineering: R: Reports*. 2001;33(4):109-34.
- [130] Whittingham MS. Lithium batteries and cathode materials. *Chemical reviews*. 2004;104(10):4271-302.
- [131] Armand M, Tarascon J-M. Building better batteries. *Nature*. 2008;451(7179):652-7.
- [132] Ji L, Lin Z, Alcoutlabi M, Zhang X. Recent developments in nanostructured anode materials for rechargeable lithium-ion batteries. *Energy & Environmental Science*. 2011;4(8):2682-99.
- [133] Cabana J, Monconduit L, Larcher D, Palacin MR. Beyond Intercalation-Based Li-Ion Batteries: The State of the Art and Challenges of Electrode Materials Reacting Through Conversion Reactions. *Advanced Materials*. 2010;22(35):E170-E92.

- [134] Poizot P, Laruelle S, Grugeon S, Dupont L, Tarascon J. Nano-sized transition-metal oxides as negative-electrode materials for lithium-ion batteries. *Nature*. 2000;407(6803):496-9.
- [135] Bruce PG, Scrosati B, Tarascon JM. Nanomaterials for rechargeable lithium batteries. *Angewandte Chemie International Edition*. 2008;47(16):2930-46.
- [136] Reddy M, Subba Rao G, Chowdari B. Metal oxides and oxysalts as anode materials for Li ion batteries. *Chemical reviews*. 2013;113(7):5364-457.
- [137] Wang Z, Zhou L. Metal Oxide Hollow Nanostructures for Lithium-ion Batteries. *Advanced materials*. 2012;24(14):1903-11.
- [138] Lai X, Halpert JE, Wang D. Recent advances in micro-/nano-structured hollow spheres for energy applications: from simple to complex systems. *Energy & Environmental Science*. 2012;5(2):5604-18.
- [139] Choi NS, Chen Z, Freunberger SA, Ji X, Sun YK, Amine K, et al. Challenges Facing Lithium Batteries and Electrical Double-Layer Capacitors. *Angewandte Chemie International Edition*. 2012;51(40):9994-10024.
- [140] Scrosati B, Hassoun J, Sun Y-K. Lithium-ion batteries. A look into the future. *Energy & Environmental Science*. 2011;4(9):3287-95.
- [141] Zhang L, Wu HB, Lou XWD. Iron-Oxide-Based Advanced Anode Materials for Lithium-Ion Batteries. *Advanced Energy Materials*. 2014;4(4):1300958.
- [142] Wang G, Shen X, Yao J, Park J. Graphene nanosheets for enhanced lithium storage in lithium ion batteries. *Carbon*. 2009;47(8):2049-53.
- [143] Bai S, Shen X. Graphene–inorganic nanocomposites. *Rsc Advances*. 2012;2(1):64-98.
- [144] Sun B, Horvat J, Kim HS, Kim W-S, Ahn J, Wang G. Synthesis of mesoporous α -Fe₂O₃ nanostructures for highly sensitive gas sensors and high capacity anode materials in lithium ion batteries. *The Journal of Physical Chemistry C*. 2010;114(44):18753-61.
- [145] Chen J, Xu L-n, Li W-y, Gou X-l. α -Fe₂O₃ nanotubes in gas sensor and lithium-ion battery applications. *Advanced Materials*. 2005;17(5):582-6.
- [146] Yan J, Fan Z, Wei T, Qian W, Zhang M, Wei F. Fast and reversible surface redox reaction of graphene–MnO₂ composites as supercapacitor electrodes. *Carbon*. 2010;48(13):3825-33.

- [147] Zhu X, Zhu Y, Murali S, Stoller MD, Ruoff RS. Nanostructured reduced graphene oxide/Fe₂O₃ composite as a high-performance anode material for lithium ion batteries. *Acs Nano*. 2011;5(4):3333-8.
- [148] Zou Y, Kan J, Wang Y. Fe₂O₃-graphene rice-on-sheet nanocomposite for high and fast lithium ion storage. *The Journal of Physical Chemistry C*. 2011;115(42):20747-53.
- [149] Liu S-Y, Xie J, Pan Q, Wu C-Y, Cao G-S, Zhu T-J, et al. Graphene anchored with nanocrystal Fe₂O₃ with improved electrochemical Li-storage properties. *Int J Electrochem Sc*. 2012;7:354-62.
- [150] Li Y, Lv X, Lu J, Li J. Preparation of SnO₂-nanocrystal/graphene-nanosheets composites and their lithium storage ability. *The Journal of Physical Chemistry C*. 2010;114(49):21770-4.
- [151] Zhou G, Wang D-W, Li F, Zhang L, Li N, Wu Z-S, et al. Graphene-wrapped Fe₃O₄ anode material with improved reversible capacity and cyclic stability for lithium ion batteries. *Chemistry of Materials*. 2010;22(18):5306-13.
- [152] Wen CJ, Huggins RA. Chemical diffusion in intermediate phases in the lithium-silicon system. *Journal of solid state chemistry*. 1981;37(3):271-8.
- [153] Hatchard T, Dahn J. In situ XRD and electrochemical study of the reaction of lithium with amorphous silicon. *Journal of The Electrochemical Society*. 2004;151(6):A838-A42.
- [154] Obrovac M, Christensen L. Structural changes in silicon anodes during lithium insertion/extraction. *Electrochemical and Solid-State Letters*. 2004;7(5):A93-A6.
- [155] Li H, Huang X, Chen L, Wu Z, Liang Y. A high capacity nano Si composite anode material for lithium rechargeable batteries. *Electrochemical and Solid-State Letters*. 1999;2(11):547-9.
- [156] Tarascon J-M, Armand M. Issues and challenges facing rechargeable lithium batteries. *Nature*. 2001;414(6861):359-67.
- [157] Szczech JR, Jin S. Nanostructured silicon for high capacity lithium battery anodes. *Energy & Environmental Science*. 2011;4(1):56-72.
- [158] Chan CK, Peng H, Liu G, McIlwrath K, Zhang XF, Huggins RA, et al. High-performance lithium battery anodes using silicon nanowires. *Nature nanotechnology*. 2008;3(1):31-5.

- [159] Cui L-F, Ruffo R, Chan CK, Peng H, Cui Y. Crystalline-amorphous core– shell silicon nanowires for high capacity and high current battery electrodes. *Nano Letters*. 2008;9(1):491-5.
- [160] Park M-H, Kim MG, Joo J, Kim K, Kim J, Ahn S, et al. Silicon nanotube battery anodes. *Nano Letters*. 2009;9(11):3844-7.
- [161] Song T, Xia J, Lee J-H, Lee DH, Kwon M-S, Choi J-M, et al. Arrays of sealed silicon nanotubes as anodes for lithium ion batteries. *Nano letters*. 2010;10(5):1710-6.
- [162] Yao Y, McDowell MT, Ryu I, Wu H, Liu N, Hu L, et al. Interconnected silicon hollow nanospheres for lithium-ion battery anodes with long cycle life. *Nano letters*. 2011;11(7):2949-54.
- [163] Chen D, Mei X, Ji G, Lu M, Xie J, Lu J, et al. Reversible Lithium-Ion Storage in Silver-Treated Nanoscale Hollow Porous Silicon Particles. *Angewandte Chemie International Edition*. 2012;51(10):2409-13.
- [164] Ng SH, Wang J, Wexler D, Konstantinov K, Guo ZP, Liu HK. Highly Reversible Lithium Storage in Spheroidal Carbon-Coated Silicon Nanocomposites as Anodes for Lithium-Ion Batteries. *Angewandte Chemie International Edition*. 2006;45(41):6896-9.
- [165] Magasinski A, Dixon P, Hertzberg B, Kvit A, Ayala J, Yushin G. High-performance lithium-ion anodes using a hierarchical bottom-up approach. *Nature materials*. 2010;9(4):353-8.
- [166] Kim H, Han B, Choo J, Cho J. Three-dimensional porous silicon particles for use in high-performance lithium secondary batteries. *Angewandte Chemie*. 2008;120(52):10305-8.
- [167] Yu Y, Gu L, Zhu C, Tsukimoto S, van Aken PA, Maier J. Reversible Storage of Lithium in Silver-Coated Three-Dimensional Macroporous Silicon. *Advanced Materials*. 2010;22(20):2247-50.
- [168] Winter M, Besenhard JO, Spahr ME, Novak P. Insertion electrode materials for rechargeable lithium batteries. *Advanced materials*. 1998;10(10):725-63.
- [169] Liu N, Wu H, McDowell MT, Yao Y, Wang C, Cui Y. A yolk-shell design for stabilized and scalable Li-ion battery alloy anodes. *Nano letters*. 2012;12(6):3315-21.

- [170] Na Y, Jang H. Oil absorbing graphene capsules by capillary molding. *Chemical Communications*. 2012;48(48):5968-70.
- [171] Lee JK, Smith KB, Hayner CM, Kung HH. Silicon nanoparticles–graphene paper composites for Li ion battery anodes. *Chemical Communications*. 2010;46(12):2025-7.
- [172] Mai L, Dong F, Xu X, Luo Y, An Q, Zhao Y, et al. Cucumber-like V_2O_5 /poly (3, 4-ethylenedioxythiophene) & MnO_2 nanowires with enhanced electrochemical cyclability. *Nano letters*. 2013;13(2):740-5.
- [173] Wei Q, An Q, Chen D, Mai L, Chen S, Zhao Y, et al. One-pot synthesized bicontinuous hierarchical $Li_3V_2(PO_4)_3/C$ mesoporous nanowires for high-rate and ultralong-life lithium-ion batteries. *Nano letters*. 2014;14(2):1042-8.
- [174] Zhao Y, Feng J, Liu X, Wang F, Wang L, Shi C, et al. Self-adaptive strain-relaxation optimization for high-energy lithium storage material through crumpling of graphene. *Nature communications*. 2014;5.
- [175] Dunn B, Kamath H, Tarascon J-M. Electrical energy storage for the grid: a battery of choices. *Science*. 2011;334(6058):928-35.



Waleed M.A.El Rouby earned his Bachelor's of Science, with honor, in Chemistry May 2004 and his Master's degree in physical Chemistry from Beni-Suef University, Egypt in May 2008. He earned his PhD degree in Carbon nanotubes and graphene synthesis for water treatment in November 2011 from Beni-Suef University. Now, he is a lecturer at Materials Science and Nanotechnology Department, Faculty of Postgraduate Studies for Advanced Sciences, Beni-Suef University. Within the next few days he will join to Vigo University, Spain for postdoctoral work.

His experience also covers wide range of the environmental application and recently in energy storage applications of nanomaterials. His research interests focus on carbon materials (graphene and CNTs), chemical method synthesis, CVD synthesis, Metal oxides nanoparticles, preparation, Characterization, and their applications.

He is a PI for three projects, the first one is funded from science and technology development fund (STDF) in Egypt, the second is a collaborative project (Egypt-South Africa), funded from Academy of Scientific Research and Technology and National research fund. The third is funded from Beni-Suef University. He is a team member in Egypt-US project entitled "Plasma-Assisted Chemical Vapor Synthesis versus Conventional Synthesis Methods of Advanced Ceramic Nanopowders" funded by STDF (Egypt) and NSF (USA).

He has about ten peer-reviewed scientific papers, and about the same number of participations in international conferences. He has participated in organizing several international conferences and workshops. He is a reviewer for more than five highly cited international journals.